`

DEPARTMENT OF MECHANICAL AND MANUFACTURING ENGINEERING

TRANSPORT PROPERTIES OF THERMOELECTRIC $Bi_{0.5}Sb_{1.5}Te_3$ THIN FILMS AND BULK ALLOYS

DOCTOR OF PHILOSOPHY DISSERTATION

ELLI SYMEOU

[2016]

DEPARTMENT OF MECHANICAL AND MANUFACTURING ENGINEERING

TRANSPORT PROPERTIES OF THERMOELECTRIC $Bi_{0.5}Sb_{1.5}Te_3$ THIN FILMS AND BULK ALLOYS

ELLI SYMEOU

A Dissertation Submitted to the University of Cyprus in Partial Fulfillment of the Requirements for the Degree of Doctor of Philosophy

December 2016

VALIDATION PAGE

Doctoral Candidate: Elli Symeou

Doctoral Thesis Title: Transport properties of thermoelectric $Bi_{0.5}Sb_{1.5}Te_3$ thin films and bulk alloys

The present Doctoral Dissertation was submitted in partial fulfillment of the requirements for the Degree of Doctor of Philosophy at the ***Department of Mechanical and manufacturing engineering*** *and was approved on the 5/12/2016 by the members of the* ***Examination Committee****.*

Examination Committee*:*

Research Supervisor: Professor Ioannis Giapintzakis **……...**

Committee Member: Associate Professor Theodora Kyratsi **……**

Committee Member: Associate Professor Loucas Louca **……..**

Committee Member: Senior Scientist Maria Dinescu **……..……..**

Committee Member: Professor Yaniv Gelbstein **……..……..**

DECLARATION OF DOCTORAL CANDIDATE

The present doctoral dissertation was submitted in partial fulfillment of the requirements for the degree of Doctor of Philosophy of the University of Cyprus. It is a product of original work of my own, unless otherwise mentioned through references, notes, or any other statements.

Elli Symeou

……..

`

Περίληψη

Στις μέρες μας, ένα από τα πιο σημαντικά και πολυσυζητημένα προβλήματα είναι η κλιματική αλλαγή και κατά συνέπεια η υπερθέρμανση του πλανήτη αλλά και η ενεργειακή κρίση. Ένα μεγάλο μέρος της ενέργειας που χρησιμοποιείται καθημερινά από διάφορες οικιακές και βιομηχανικές διεργασίες μετατρέπεται σε άχρηστη θερμότητα. Τα θερμοηλεκτρικά υλικά μπορούν να μετατρέψουν αυτή την άχρηστη θερμότητα, σε ηλεκτρισμό και κατά συνέπεια να αποτελέσουν μέρος της λύσης του ενεργειακού αλλά και κλιματικού προβλήματος που αντιμετωπίζουμε σήμερα. Αν και η σημερινή απόδοση των θερμοηλεκτρικών διατάξεων είναι χαμηλή (~7), πρόσφατα έχουν εμφανιστεί υλικά, τα οποία υπόσχονται να αυξήσουν την απόδοση στο 15-20% (1). Η απόδοση των θερμοηλεκτρικών υλικών, σε bulk μορφή, καθορίζεται από τον αδιάστατο θερμοηλεκτρικό συντελεστή $ZT= S^2T/\rho\kappa$, όπου S,ρ, κ, S^2/ρ και Τ είναι ο συντελεστής Seebeck, η ειδική αντίσταση, η θερμική αγωγιμότητα, η θερμοηλεκτρική ισχύς (PF) και η θερμοκρασία. Η απόδοση των θερμοηλεκτρικών λεπτών υμενίων, καθορίζεται από την θερμοηλεκτρική ισχύς, διότι η μέτρηση της θερμικής αγωγιμότητας των λεπτών υμενίων είναι πολύ δύσκολη.

Η ένωση $Bi_{0.5}Sb_{1.5}Te_3$ (BST) χαρακτηρίζεται ως το “the state of art” θερμοηλεκτρικό υλικό σε θερμοκρασία δωματίου αφού παρουσιάζει πολύ υψηλή απόδοση σε bulk μορφή αλλά όχι συγκρίσιμη με τις μέχρι τώρα υπάρχουσες τεχνολογίες (ZT=1.4 , PF=3770 $\mu V/K^2m$ στους 390K). Από την άλλη, η απόδοση των λεπτών υμενίων, τα οποία μπορούν να χρησιμοποιηθούν σε μικρής κλίμακας ηλεκτρονικές εφαρμογές, παραμένει χαμηλή. Οπόταν η περαιτέρω μελέτη αυτού του υλικού και στις δύο μορφές, κρίνεται απαραίτητη.

Η παρούσα διδακτορική διατριβή χωρίζεται σε δύο μέρη. Στο πρώτο μέρος, αναπτύχθηκαν λεπτά υμένια BST , με την μέθοδο παλμικής εναπόθεσης με λέιζερ, με σκοπό την επίτευξη μιας υψηλής θερμοηλεκτρικής απόδοσης συγκρίσιμης με αυτή των bulk υλικών. Για τον σκοπό αυτό, κατασκευάστηκαν και αποδομήθηκαν στόχοι με την επιθυμητή στοιχειομετρία για την ανάπτυξη λεπτών υμενίων πάνω σε υπόστρωμα γυαλιού. Αρχικά μελετήθηκαν οι συνθήκες εναπόθεσης, ώστε να βρεθούν οι βέλτιστες, που να οδηγούν σε υψηλές θερμοηλεκτρικές αποδόσεις. Στη συνέχεια, τα λεπτά υμένια , αναπτύχθηκαν σε θερμοκρασία δωματίου και

πέρασαν από ανόπτηση, ώστε να βελτιστοποιηθούν περαιτέρω οι ιδιότητες τους. Επίσης, μελετήθηκε κατά πόσο οι αναλογίες Bi/Te και Bi/Sb μπορούν να επηρεάσουν τις θερμοηλεκτρικές ιδιότητες των λεπτών υμενίων. Είναι αξιοσημείωτο, ότι η θερμική αγωγιμότητα στα λεπτά υμένια είναι μικρότερη από ότι στα bulk υλικά, λόγω σκεδάσεων των φωνονίων στις επιφάνειες και διεπιφάνειες. Έτσι, η επίτευξη ίδιας θερμοηλεκτρικής ισχύς με αυτήν των bulk υλικών μπορεί να οδηγήσει σε ένα υψηλότερο ZT. Η ανάπτυξη λεπτών υμενίων σε εύκαμπτα υποστρώματα βρίσκει πολλές εφαρμογές όπως για παράδειγμα σε ενδυτά ηλεκτρονικά. Έτσι, τέλος, αναπτύχθηκαν λεπτά υμένια σε εύκαμπτο υπόστρωμα ώστε να μελετηθεί κατά πόσο οι συνθήκες ανόπτησης και θερμοκρασίας υποστρώματος, επηρεάζουν τις θερμοηλεκτρικές ιδιότητες τους. Στο δεύτερο μέρος, ετοιμάστηκαν και χαρακτηρίστηκαν bulk BST υλικά με έξτρα προσθήκη Te, με την μέθοδο hot press και hot deformation, με σκοπό να επιτευχθεί ίδια ή και υψηλότερη θερμοηλεκτρική απόδοση από την υπάρχουσα (2).

Αποτέλεσμα αυτής της προσπάθειας, είναι η επίτευξη της υψηλότερης μέχρι σήμερα, θερμοηλεκτρικής ισχύς στα λεπτά υμένια και ίσης θερμοηλεκτρικής απόδοσης με αυτή της βιβλιογραφίας, στα bulk υλικά.

Abstract

In recent years, researchers and industries are attempting to find solutions for the escalating energy crisis and the threatening global warming. The huge amount of waste heat generated from several domestic and industrial processes could be directly converted to electricity by using thermoelectric devices. However, currently available thermoelectric devices are not in common use, because of their low efficiency (~7%). The next generation of thermoelectric materials are expected to produce thermoelectric devices with conversion efficiency 15-20% (1).

The conversion efficiency of thermoelectric materials is expressed through the dimensionless figure of merit, $ZT= S^2T/\rho\kappa$ where S, ρ, κ, S^2/ρ and T are the Seebeck coefficient, the electrical resistivity, the total thermal conductivity, the thermoelectric power factor (PF) and the operation absolute temperature, respectively.

$Bi_{0.5}Sb_{1.5}Te_3$ (BST) is considered to be a state-of-the-art p-type thermoelectric material, for temperatures near room temperature. In bulk form, BST exhibits $ZT\approx1.4$ and PF= 3770 $\mu V/K^2m$ at 390K. While these values are very encouraging, there is much more work to be done in order to develop higher-efficiency thermoelectric devices. In addition, for small-scale electronic applications, with small heat loads, thermoelectric thin films are more appropriate; however, the PF of BST thin films is still rather low.

My PhD thesis work is divided in two parts. The objective of the first part concerned the growth of BST films with bulk-like thermoelectric properties. To this end, we grew p-type BST thin films on fused silica substrates using pulsed laser deposition and home-made targets. Initially, we deposited BST films with different deposition conditions in order to obtain the optimum growth conditions. Then, the films were grown at room temperature followed by a post-deposition ex-situ annealing process in order to optimize their thermoelectric properties. Our results, concerning the PF value of the BST films, are very encouraging. Understanding the factors that influence the thermoelectric properties of BST (bulk and thin films) required further systematic investigations. To this end, we explored the effect of Sb-alloying on the

thermoelectric properties of BST samples. Another issue we investigated concerned the growth and thermoelectric characterization of BST films on flexible substrates, as flexibility of these materials is an interesting feature for many applications such as wearable electronics. The influence of substrate temperature and annealing treatment on the thermoelectric properties of these films was studied. In the second part, we dealt with the preparation and thermoelectric characterization of bulk BST with the objective to achieve similar or higher ZT than the highest reported value (2). A series of p-type bulk $Bi_{0.5}Sb_{1.5}Te_3$-with excess Te samples were prepared by hot press (HP) and by hot deformation (HD) with varying processing conditions.

We have achieved the highest PF value, ever reported in the case of BST films on fused silica and Kapton substrates, which is comparable with the bulk value. While in the case of bulk BST we have achieved the same ZT value as the highest one reported in the literature.

Acknowledgments

First of all, I would like to thank my supervisor, Professor Ioannis Giapintzakis for the continuous support during my PhD study, for his patience, understanding and knowledge that he gave me. My sincere thanks also goes to Associate Professor Theodora Kyratsi for her help and support.

I would also like to thank Dr. George Athanasopoulos for teaching me almost all the equipment that I was using during my PhD study and Dr. Maria Pervolaraki for teaching me the pulsed laser deposition technique. I would like also to thank Dr. Christian Mihailescu and Mrs. Christiana Nicolaou for their assistance with the XRD measurements. Moreover, I would like to thank Mr. Kypros Stylianou, our laboratory technician, for his help with technical problems.

I am really grateful for the Scholarship for the academic distinction "Roy Pogiatzi'' 2014-2015, which was sponsored by Mr. Roy Pogiatzis.

Special thanks goes to my family and my aunt Maria for always being there for me. Last but not least, I am mostly grateful to my husband Andreas and my daughter Nefeli, for their love and understanding.

List of publications

1. E. Symeou, M. Pervolaraki, C.N Mihailescu, G.I. Athanasopoulos, Ch. Papageorgiou, Th. Kyratsi, J. Giapintzakis, 'Thermoelectric properties of $Bi_{0.5}Sb_{1.5}Te_3$ thin films grown by pulsed laser deposition', Appl. Surf. Sci. 336 (2015) 138–142

2. M. Ioannou, E. Symeou, J. Giapintzakis and Th. Kyratsi, 'Structural Characterization and Thermoelectric Properties of Hot-Pressed CoSi Nanocomposites', J. Electron. Mater. 43 (2014) 3824-3830

3. M. Ioannou, A. Delimitis, E. Symeou, J. Giapintzakis and Th. Kyratsi, 'Effect of Silicon Nitride/Oxide on the Structure and the Thermal Conductivity of CoSi Nanocomposites', J. Nanosci. Nanotechnol. 16 (2016) 1–9

4. E. Symeou, Ch. Nicolaou and J. Giapintzakis, 'Enhanced thermoelectric properties in pulsed laser deposition-prepared $Bi_{0.5}Sb_{1.5}Te_3$ thin films through vacuum annealing', submitted to Journal of alloys and compounds

5. E. Symeou, Ch. Nicolaou, Th. Kyratsi and J. Giapintzakis, 'High Thermoelectric Performance of p-type $Bi_{0.5}Sb_{1.5}Te_3$ Bulk Alloys in the in-plane direction', submitted to Journal of Solid State Chemistry

List of conference presentations

1. Poster: '$Bi_{0.5}Sb_{1.5}Te_3$ thin films with bulk-like thermoelectric properties on glass and flexible substrates', E. Symeou, Ch. Nicolaou and J. Giapintzakis, European Conference on Thermoelectrics, 20-23/9/2016, Lisbon, Portugal

2. Oral Presentation: 'Thermoelectric properties of Bi-Sb-Te thin films prepared by pulsed laser deposition on fused silica and flexible substrates', E. Symeou, Ch. Nicolaou and J. Giapintzakis, European Materials Research Society, Spring Meeting, 2-6/05/2016, Lille, France.

3. Oral Presentation: 'Thermoelectric properties of $Bi_{0.5-x}Sb_{1.5}Te_{3+x}$ thin films with various compositions', E. Symeou, C. N. Mihailescu, M. Pervolaraki and J. Giapintzakis, European Materials Research Society, Fall Meeting, 15-18/09/2015, Warsaw, Poland.

4. Poster: '$Bi_{0.5}Sb_{1.5}Te_3$ thin films for thermoelectric cooling applications', E. Symeou, M. Pervolaraki, C. N. Mihailescu, G. I. Athanasopoulos, Ch. Papageorgiou, Th. Kyratsi, and J. Giapintzakis, European Materials Research Society, Spring Meeting, 26-30/05/2014, Lille, France.

5. Poster: 'Fabrication and characterization of planar thin film Ag-Bi-Ag structures', E. Symeou, G. I. Athanasopoulos, J. Giapintzakis, Workshop: Nanoscience of Advanced Thermoelectrics for Energy Conversion, 5 July 2011, University of Cyprus, Nicosia, Cyprus.

Contents

List of Figures

List of Tables

`

Chapter 1

1. Introduction

1.1 Motivation

Researchers and industries are attempting to find solutions for the escalating energy crisis and the threatening global warming. According to the energy outlook 2035 from BP PLC, the world energy consumption will increase by 41% between 2012 and 2035. Global energy intensity in 2035 is expected to be 36% lower than what it was in 2012, while energy per capita use is expected to increase by 14% (4). Do we have enough energy reserves for these needs? The achievement of highly efficient thermal management may contribute to solving this energy problem. A report mentioned that 69% of energy demand is for heating / cooling and electricity. On the other hand, 191 million vehicles in the US, dissipate 66% of their energy as waste heat. (5). Thus, the huge amount of waste heat generated from home heating, automotive exhaust and industrial processes could be converted directly to electricity by using thermoelectric devices (6). Low efficiency (~7%) and high cost are the disadvantages of these thermoelectric devices. If we could improve their efficiency, then the thermoelectric devices could be an important part of the solution to today's energy challenge. Recent findings indicate that the efficiency of these thermoelectric devices could be increased up to 20% (1).

Thermoelectric effect is the phenomenon of direct conversion of temperature difference to electric voltage and vice versa and is based on the Seebeck and Peltier phenomena (7). In 1821, **Seebeck** observed that if two dissimilar conductors were joined together and the junctions were held at different temperatures was created a voltage difference. The Seebeck effect is the basis for thermoelectric **power generation devices**. Thermoelectric generations are noiseless with no moving part, reliable, durable and emission-free operation. Due to all these properties, thermoelectric generators can be used for converting directly heat form automotive exhaust and industrial processes to electricity (8). Also the solar radiation can be exploited by the solar thermoelectric generator, which can be used to convert sunlight to electricity, by placing the thermoelectric generator between a solar absorber and a heat sink. When the solar absorber is exposed to sunlight, it heats up, and as a consequence a temperature gradient is created across

the thermoelectric elements. This gives an alternative route towards solar power exploitation in addition to photovoltaics and solar thermal plants. A few years later, **Peltier** observed the reverse of Seebeck effect, which refers to a temperature difference generated by a voltage gradient. This effect is the basis for **thermoelectric refrigeration devices** which could be used for cooling applications. The majority of thermoelectric applications requires devices based on bulk materials. However, there are several applications where small heat loads or low levels of power generation are involved, for examples, localized cooling in micro- and nano-electronics as well as energy autonomy in applications such as wireless sensor networks which could be well served by thin-film thermoelectric devices fabricated on rigid and/or flexible substrates. Flexible substrates have received much attention because of their low cost, light weight and favorable assembly properties. Also flexible thin film nanogenerators can be attached on various places, such as human bodies, as wearable electronics and wearable biometric monitoring sensors (9), (10).

The performance of these solid-state thermoelectric energy converters depends on the dimensionless thermoelectric figure of merit (ZT) of the constituent materials. While the results to date are very encouraging, there is much more work to be done in thermoelectric materials in order to develop higher-efficiency thermoelectric devices.

This work is divided in two parts. The objective of the first part concerns the growth of $Bi_{0.5}Sb_{1.5}Te_3$ thermoelectric thin films, by pulsed laser deposition, with bulk-like thermoelectric properties. Even though $Bi_{0.5}Sb_{1.5}Te_3$ is a very popular material, there is no 'magic recipe' reported yet, which leads to a repeatable high efficiency of $Bi_{0.5}Sb_{1.5}Te_3$ thin films. The innovation of this work concerns the investigation of the factors which influence the thermoelectric properties of $Bi_{0.5}Sb_{1.5}Te_3$ films and lead to enhanced thermoelectric properties. Furthermore, we have attempted to obtain these properties, onto a flexible substrate. Our results, concerning the PF value of $Bi_{0.5}Sb_{1.5}Te_3$ films, are very encouraging. The second part deals with the preparation and characterization of bulk $Bi_{0.5-x}Sb_{1.5+x}Te_3$ with the objective to achieve similar or higher ZT than the highest reported values (2). We have employed both hot press and hot deformation methods to tune the microstructure in an effort to enhance the thermoelectric properties. In addition, we have examined the effect of stoichiometry (adding more Sb for Bi) on maximizing ZT and shifting the temperature of maximum ZT to higher temperatures than

room temperature in an effort to utilize these materials for low-temperature power generation applications. Our BST materials exhibit similar ZT values to the highest reported in the literature and at higher temperatures than room temperature.

1.2 Background

1.2.1 Thermoelectric figure of merit

The efficiency of thermoelectric energy converters depends on the transport coefficients of the constituent materials through the figure of merit (11):

$$ZT = \frac{\sigma . S^2}{\kappa} . T \qquad (1)$$

Where σ, S, κ, T, $\sigma.S^2$ are the electrical conductivity, Seebeck coefficient, total thermal conductivity, absolute temperature and power factor (PF), respectively.

ZT is a complex quantity which involves both the charge and heat transport properties of the material. The system of free charge carriers (electron and holes), the phonon system and the interaction between both systems influence the ZT. Therefore, ZT can be described in terms of the electronic band structure, the lattice dynamical properties, and the charge carrier scattering mechanisms such as phonons and crystal impurities. Finally, the chemical bonding determines all these properties (11).

The thermoelectric efficiency, ε, in power generation mode and the coefficient of performance n in refrigeration mode of a thermoelectric couple are given by the following equations (12):

$$\varepsilon = \frac{T_H - T_C}{T_H} . \frac{(1 + ZT_M)^{1/2}}{(1 + ZT_M)^{1/2} + (\frac{T_C}{T_H})} \qquad (2)$$

$$n = \frac{T_c \ [(1 + ZT)^{\frac{1}{2}} - \frac{T_H}{T_C}]}{T_H - T_C \ [(1 + ZT)^{\frac{1}{2}} + 1]} \qquad (3)$$

Where T_H, T_C, T_M are the hot side, cold side and average temperature, respectively. The Carnot efficiency can be expressed as:

$$\eta = \frac{T_H - T_C}{T_H} \quad (4)$$

The thermoelectric refrigerators have about one third of the efficiency of the conventional refrigerators, which is about 10% of the Carnot efficiency (13). As can be seen in Figure 1.1, ZT values of 2-3 are needed, in order the thermoelectric refrigerators, to be competitive with traditional mechanical energy conversion systems.

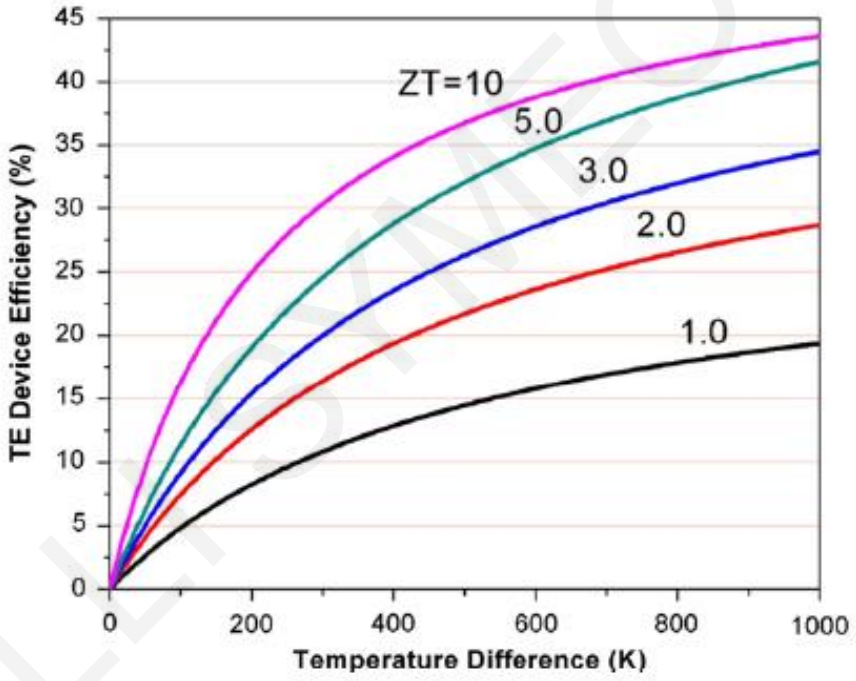

Figure 1.1. Thermoelectric energy conversion as a function of ZT at the setting of Tc=300 K (12).

The best thermoelectric materials have been defined as "phonon-glass electron-crystal", which means that the materials should have a low lattice thermal conductivity as in a glass, and a high electrical conductivity as in a crystal. Thermoelectric material which is characterized as 'good thermoelectric' must have high electrical conductivity, low thermal conductivity and high Seebeck coefficient in order to minimize Joule heating, to prevent thermal shorting and to maximize the conversion of heat to electrical power, respectively (14), (15). This is a challenge

given that the transport properties of the materials are interrelated. Next, I will discuss the basic principles for improving thermoelectric efficiency.

1.2.1.1 Electrical conductivity

The electrical conductivity (σ) is a measure of the material's ability to conduct an electrical current. Electrical conductivity and electrical resistivity (ρ) are related to the carrier concentration (n) through the carrier mobility (μ).

Equations 5 and 6 give the electrical conductivity and mobility, respectively.

$$\sigma = \frac{1}{\rho} = n.e.\mu \quad (5)$$

$$\mu = \frac{e.\tau}{m^*} \quad (6)$$

Where m^* is the effective mass and τ is the mean scattering time between collisions for the carriers. For semiconductors, σ involves the contributions of both holes and electrons:

$$\sigma = n.e.\mu_e + p.e.\mu_h \quad (7)$$

Where n and μ_e are the electron concentration and mobility, respectively, and p and μ_h are the hole concentration and mobility, respectively. There are two primary ways to achieve a high conductivity in a semiconductor, either by having a very small gap or by having very high concentration of carriers with high mobility (8).

1.2.1.2 Seebeck coefficient

The Seebeck coefficient (S) or thermopower expresses the ability of the material, when in a temperature gradient, to develop a voltage between the hot end and the cold end of the sample.

The charge carriers at the hot end of the sample have more kinetic energy than the charge carriers at the cold end and move faster towards the cold end. After several high energy carriers move to the cold end, they set up a voltage which prevents further movement of the high energy carriers to the cold end (16). The Seebeck coefficient for different carrier types is given by a weighted average to their electrical conductivity values (σ_e and σ_p): The Seebeck coefficient is positive if the charge carriers are holes and negative if the charge carriers are electrons. If charge carriers of both type are present, the resulting Seebeck coefficient is given by the following equation:

$$S \approx \frac{S_e.\sigma_e + S_p.\sigma_p}{\sigma_e + \sigma_p} \quad (8)$$

The Seebeck coefficient is given by the Mott expression (17) and according to this equation S is a measure of the variation in σ(E) above and below the Fermi surface (18).

$$S = \frac{\pi^2.k^2}{3.e}.T.\left(\frac{dln\sigma(E)}{dE}\right)_{E=E_F} \quad (9)$$

Where σ(E) is the electrical conductivity determined as a function of Fermi energy, E_F. If the electronic scattering is independent of energy, then σ(E) is just proportional to the density of states (DOS) at E.

One way to increase the Seebeck coefficient is the modification of DOS. For maximum Seebeck, a large asymmetry in DOS is required. As can be seen in Figure 1.2, S depends on the dimensionality of the sample. For materials in the bulk form, DOS has a square root dependence on energy and this dependence changes accordingly with the dimensionality of the quantum system (19). Another way to alter S is to decrease the carrier concentration; however, decreasing the carrier concentration results in decreasing the electrical conductivity too.

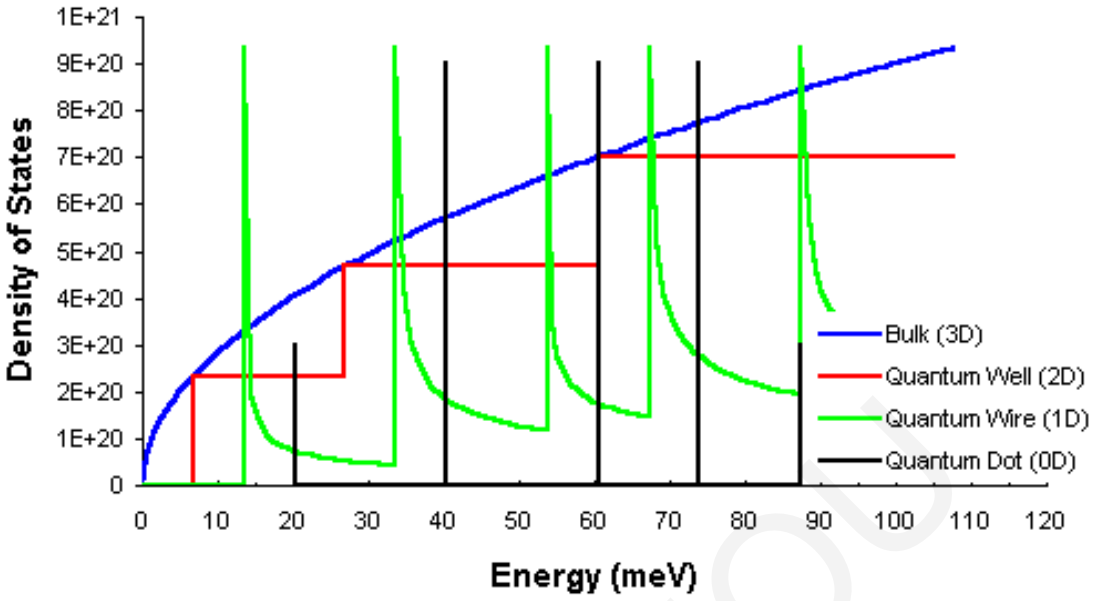

Figure 1.2. Density of states for bulk (3D blue), quantum well (2D red), quantum wire (1D green) and quantum dot (0D black).

1.2.1.3 Carrier concentration

Seebeck coefficient is mainly related with the carrier concentration, as I discussed above. For a large S, the type of carrier should only be restricted to a single type. Mixed n-type and p-type conduction leads to both charge carriers moving to the cold end, cancelling out the induced Seebeck voltages and consequently, the Seebeck coefficient becomes smaller, (Eq.8) (20).

1.2.1.4 Electronic thermal conductivity

The thermal conductivity is related to the transfer of heat through a material and is usually the sum of two contributions, one due to phonons ($k_{lattice}$) and the other due to charge carriers ($k_{carriers}$), i.e., electrons and holes transporting heat. According to Wiedemann-Franz law, the electronic thermal conductivity (k_e) is given by:

$$k_e = L.T.\sigma \qquad (10)$$

The electronic thermal conductivity is proportional to the electrical conductivity and it is not possible to reduce one while increasing the other. The k_e is affected by carrier concentration and carrier mobility. As carrier concentration increases, k_e increases. It is noteworthy that the Lorentz number L depends on carrier concentration (increase in carrier concentration implies an increase in L value) (7). Therefore, to reduce the electronic thermal conductivity of thermoelectric materials is not always the best choice, as it will adversely affect the electrical conductivity and has little or no improvement on ZT.

1.2.1.5 Lattice thermal conductivity

The lattice thermal conductivity (κ_l) is the only parameter that is not affected by the electronic structure, so ZT can be enhanced by minimizing the lattice thermal conductivity. Lattice thermal conductivity can be expressed by the following equation:

$$\kappa_l = \frac{1}{3}.(C_u.u_s.\lambda_{ph}) \qquad (11)$$

Where C_u is the heat capacity, u_s is the sound velocity, and λ_{ph} is the phonon mean free path. The crystal structure, defects and grain boundaries affect the lattice thermal conductivity. The lattice thermal conductivity can be reduced by scattering phonons within the unit cell, for example, by creating rattling structures or point defects or by alloying. Good thermoelectric materials are alloys because the lattice thermal conductivity is reduced due to alloy scattering. However, the electrical mobility (and electrical conductivity) is also generally reduced by alloying but the reduction in the lattice thermal conductivity is generally much greater than the reduction in the electrical conductivity (21). For example, Figure 1.3 presents a model system of Bi_2Te_3 with a κ_l of 0.8 W/mK and κ_e as a function of the carrier concentration. The corresponding ZT is on point 1. Reducing κ_l to 0.2 W/m K directly increases ZT to point 2. If the thermal conductivity decreases more, the carrier concentration can be reduced and as a consequence of this, k_e decreases and S increases. Point 3 shows the re-optimization of ZT (20).

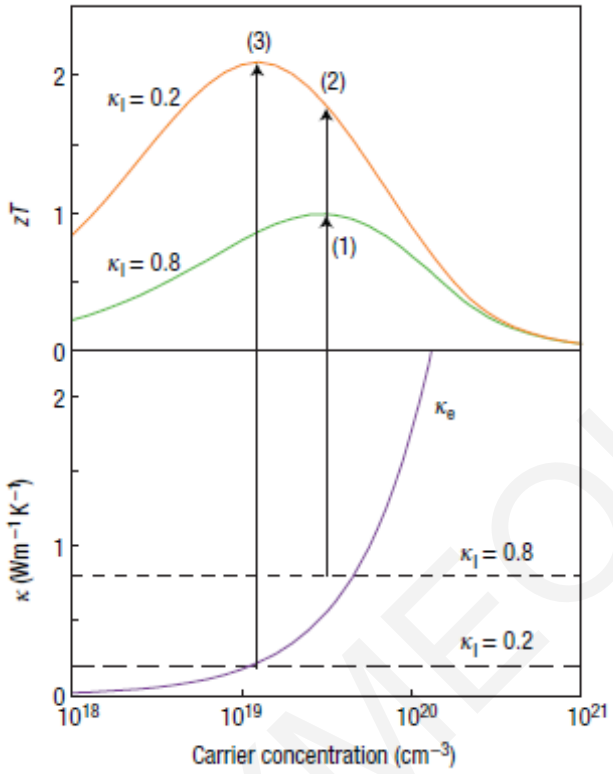

Figure 1.3. Increasing the ZT by reducing thermal conductivity.

Based on the discussion above, we arrive again to the characteristic phrase: "Find a rather unusual material, a phonon-glass electron crystal." (20) So, **what class of materials can be potential thermoelectric materials?** Metals exhibit high electrical conductivity (~100 S/cm), as a result they are also characterized by high electronic thermal conductivity but they have very low Seebeck coefficient (~5 μV/K). So, metals aren't a good choice for thermoelectric applications. The insulators have large band gap and large Seebeck coefficient (~1000 μV/K) but very low electrical conductivity (~10^{-12} S/cm). This results in a small value of PF, and thus a small Z (~5×10^{-17} /K), which is far smaller than that of metal (~3×10^{-6} /K). Consequently, as it is shown in figure 1.4 the optimal thermoelectric materials with a large value of PF are typically heavily doped semiconductors with a carrier concentration between 10^{19} and 10^{21} carriers per cm^3 (8).

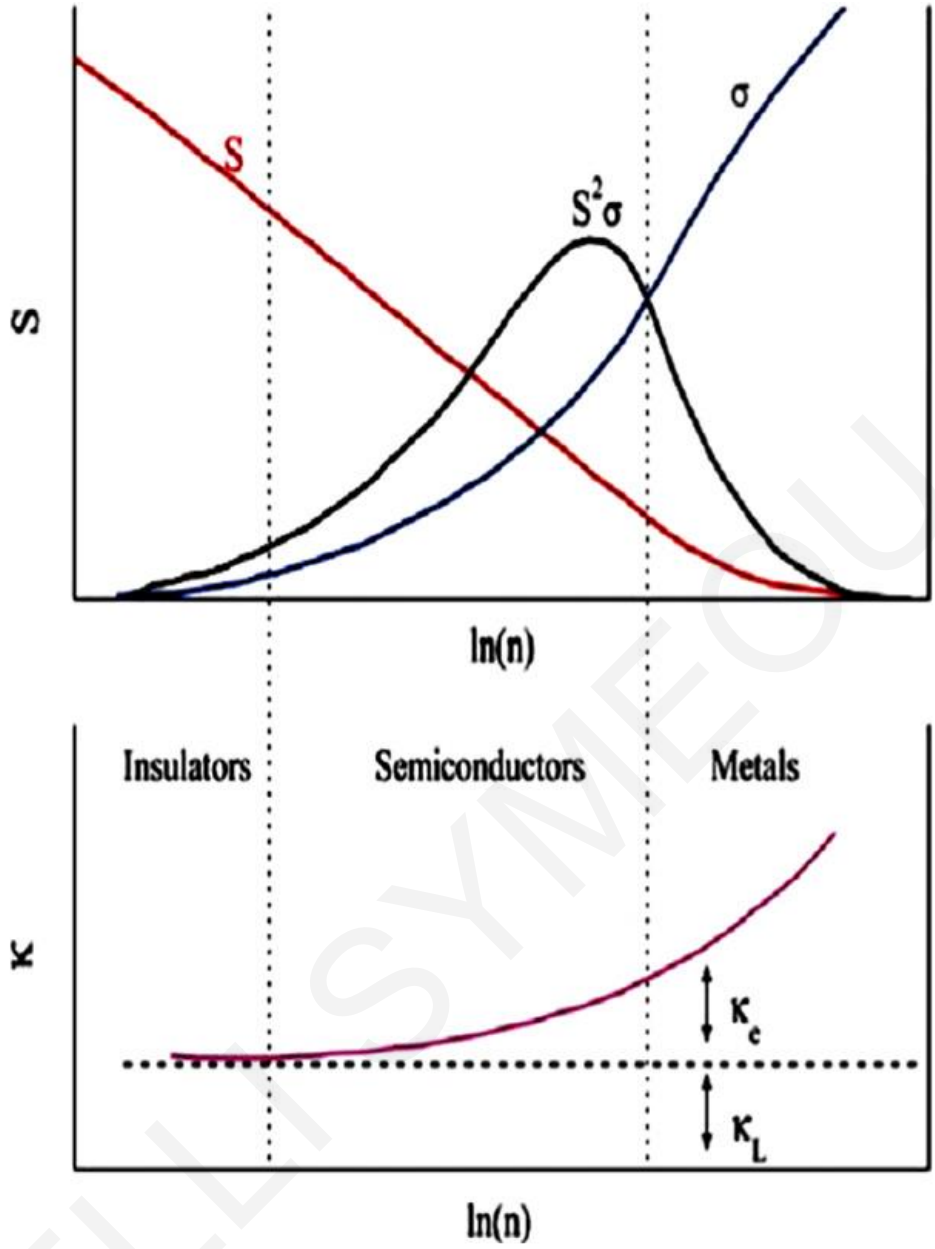

Figure 1.4. Free charge carrier concentration dependence of Seebeck coefficient, electrical conductivity and thermal conductivity. Good thermoelectric materials are typically heavily doped semiconductors with a carrier concentration between 10^{19} and 10^{21} carriers per cm^3 (12) .

1.3 Thermoelectric materials

1.3.1 Overview of thermoelectric materials

Following the reviews of J. C. Zheng (22) and Z. G. Chen (12), I will provide some information about the typical thermoelectric materials. From a historic point of view, the discovery of thermoelectric materials started in 1950. Conventional semiconductors such as group V chalcogenides (Bi_2Te_3, Sb_2Te_3) (23), (24), (25), group IV chalcogenides (PbTe) (23), group III-V (InSb), and group IV-IV (SiGe), were developed for applications at room temperature, intermediate temperature and high temperature, respectively. In 1960, the method used for the improvement of the ZT was to control doping and form solid solutions, such as Bi_2Te_3-Sb_2Te_3, PbTe-SnTe and $Si_{1-x}Ge_x$. Nevertheless, the overall ZT enhancement was limited (26) due to the reduction in the charge carrier mobility even though the reduction in the lattice thermal conductivity by the introduced point defects was notable. From 1960 to 1990, the research in the field of thermoelectrics stagnated and $(Bi_{1-x}Sb_x)_2$ $(Se_{1-y}Te_y)_3$ remained the best material with ZT~1 (27). From 1990 until today, the thermoelectric materials received much attention in order to re-investigate advanced thermoelectric materials with high ZT such as complex materials, for example, skutterudites (28) , (29), (30), clathrates (31), (32), (33), (34), half-Heusler alloys (35), complex chalcogenides (36), (37) and cobaltites (38), (39), (40). In 1993 (41), nano-technology was introduced in the scientific research and opened up new horizons (10). With the use of the thin film depositions techniques the nano-scale phenomena began to be exploited in order to enhance the thermoelectric performance. Some examples of the nano-technology are the low-dimensional thermoelectric quantum wells (42) quantum dots, nanowires (43), (44) , thin films (25) and molecular junctions (45). The trend is clear. The thermoelectric community follow two different approaches in order to achieve high ZT values. First, finding materials with complex structures and then synthesizing low-dimensional thermoelectric materials (nanostructures) either in the bulk form or in thin film form.

Approaches and examples

Low-dimensional thermoelectric materials: Thin films, quantum dots, quantum wells are found to exhibit very high values of ZT because the scattering of phonons is stronger when the size of the sample in at least one direction is reduced, while the scattering of carriers is not affected due to their small mean free path. Furthermore, by using the quantum confinement effects in order to obtain the enhanced density of states near Fermi level, the ZT of these low dimensional thermoelectric materials can be enhanced. Example of this enhancement was reported by Harman et al., which achieved a ZT of 0.9 at 300K and ZT of 2 at 390K in PbSeTe/PbTe quantum dot structures (46). Also Venkatasubramanian et al. have reported that the ZT of Bi_2Te_3-Sb_2Te_3 superlattices became 2.5 times larger than that of the conventional Bi_2Te_3-Sb_2Te_3 bulk material because the thermal conductivity was reduced more than the electrical conductivity (25).

Bulk thermoelectric materials: The first approach is the 'phonon-glass electron-crystal' (PGEC) that I mentioned above, which suggests that materials with complex crystal structures can reduce the lattice thermal conductivity due to the induced voids and rattlers (heavy elements atoms located in the voids). An example of PGEC material is $Ba_{0.08}La_{0.05}Yb_{0.04}Co_4Sb_{12}$ with ZT of 1.7 at 850K (47). The second approach, is the creation of nanostructuring in thermoelectric materials, which is divided in two types, according to Kanatzidis (1). In the first type, a single phase of the material exists with nanosize particles or grains. In the second type, a system with a major bulk phase is created with contains a minor second phase in nanoscale size. Nanostructured thermoelectric materials can enhance the density of states near Fermi level via quantum confinement which leads an increase of the PF (Seebeck coefficient and electrical conductivity). Other advantages of nanostructuring are the ability to reduce the lattice thermal conductivity by the introduction of a large density of interfaces in which phonons with a large mean free path can be scattered more effectively than electrons (keeping unaffected the carrier mobility and electrical conductivity), as shown in Figure 1.5. With this approach, ZT of about 2.2 was achieved in the complex nanostructured PbTe-based alloy $Ag_{1-x}Pb_{18}SbTe_{20}$ (LAST) fabricated by the melt method. From TEM analysis seems that the LAST alloys are complex nanostructured composites containing Ag-Sb rich nanoscale inclusions which play an important

role in the reduction of thermal conductivity and as a consequence in the enchantment of ZT (36).

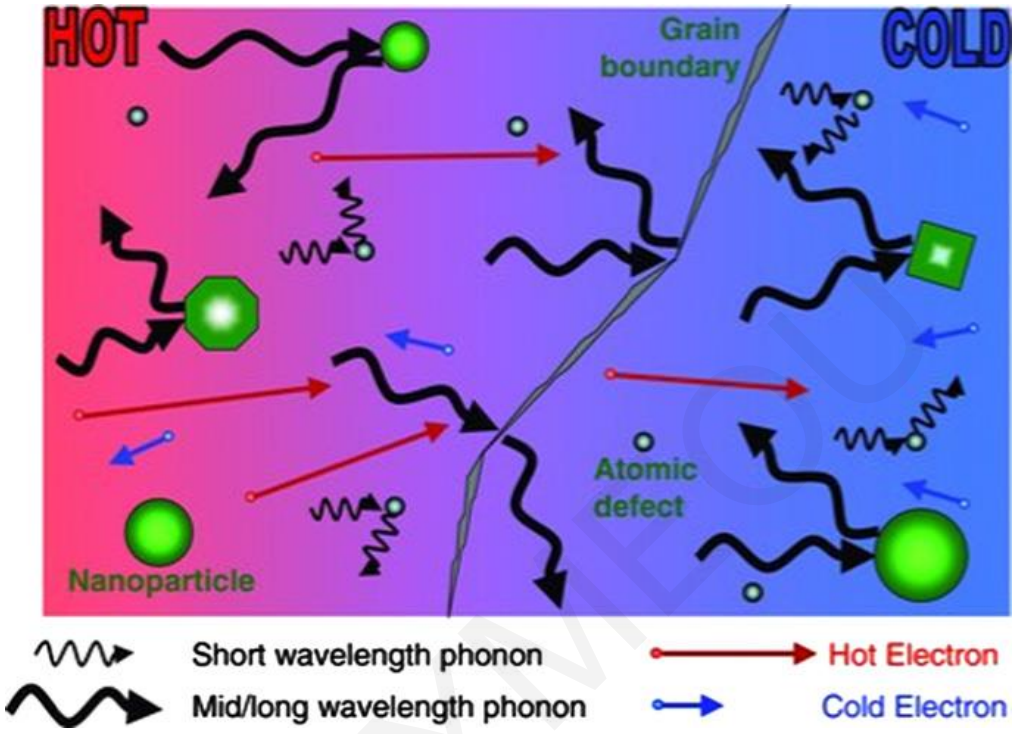

Figure 1.5. Schematic diagram illustrating various phonon scattering mechanisms within a thermoelectric material, along with electronic transport of hot and cold electrons (48).

Summarizing, we can say that the thermoelectric materials can be divided in three generations (1). In the first generation of thermoelectrics belong materials with an average ZT of about 1 and 4-5% conversion efficiency. The second generation of thermoelectric materials have ZT about 1.3 -1.7, which is based on the reduction of thermal conductivity via nanoscale precipitates and compositional in-homogeneities (49). The conversion efficiency of these materials is about 11-15%. The third generation of thermoelectric materials with ZT about 1.8-2.2 and conversion efficiency 15-20% have recently appeared. These high ZT values are attributed to the enhancement of Seebeck coefficients through valence band convergence, retention of the carrier mobility through band energy offset minimization between matrix, and reduction of lattice thermal conductivity (50). Figure 1.6 shows the highest ZT values to date.

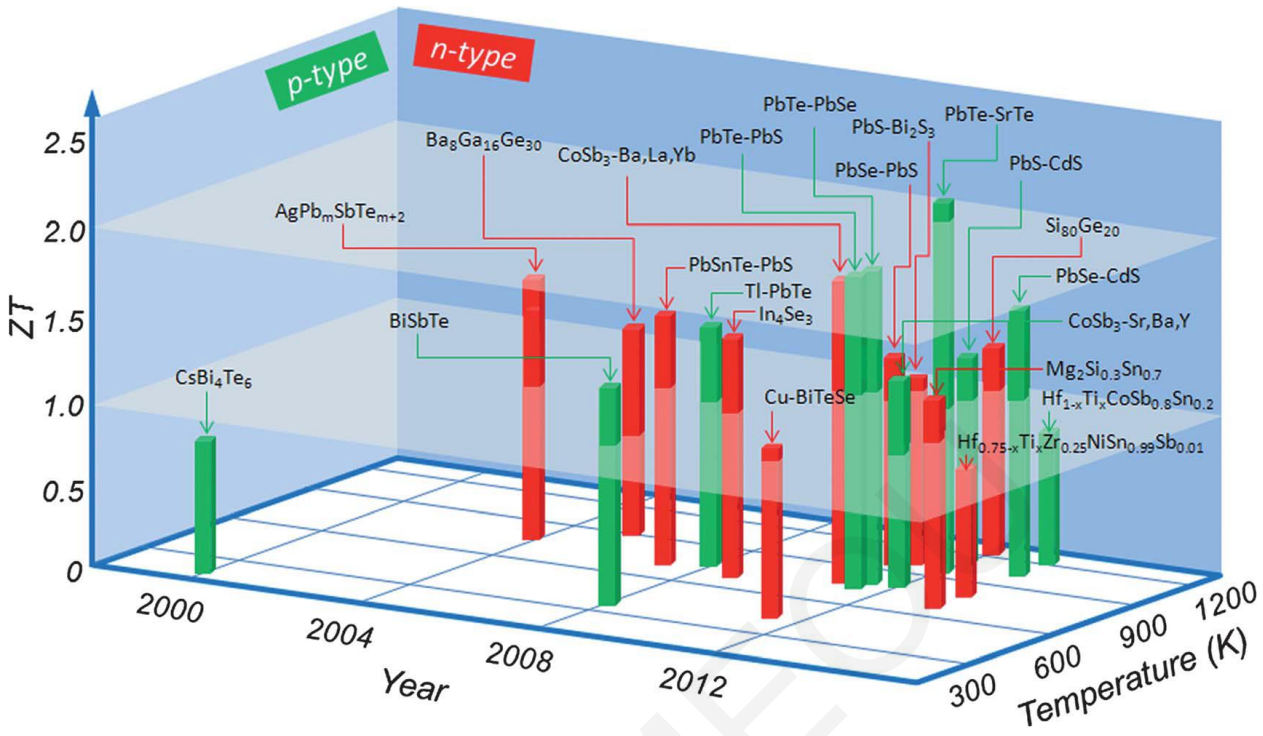

Figure 1.6. State of the art thermoelectric materials as a function of temperature and years. Re- produced from (1).

1.3.2 Thermoelectric $Bi_{0.5}Sb_{1.5}Te_3$ (BST)

In 1954, Goldsmid discovered the excellent thermoelectric properties of bismuth telluride and attributed his findings to the large mean molecular mass (low lattice thermal conductivity), low melting temperature and partial degeneracy of the conduction and valence bands of this V-VI chalcogenide (51). Since then, bismuth telluride has been widely studied as a thermoelectric material, in the temperature range around 300K and is widely used in thermoelectric cooling applications. It is also the best material for use in thermoelectric generators when the temperature of the heat source is moderate. It is a narrow-gap semiconductor with an indirect gap of approximately 0.15 eV (52). The layered rhombohedral crystal structure [space group D_{3d}^5 (R3m)] of Bi_2Te_3, Sb_2Te_3 and the alloy $Bi_{2-x}Sb_xTe_3$, is presented in Figure 1.7. The hexagonal unit cell contains three quintuples, each of which is composed of five atomic layers in the order of Te(1)-Bi/Sb-Te(2)-Bi/Sb-Te(1) along the c-axis. Te and Bi/Sb layers are held together by strong ionic-covalent bonds [Te(1)-Bi and Bi-Te(2)]; however, between Te(1) atomic planes of neighboring quintuples there is a van der Waals gap (53). This structural anisotropy leads to anisotropy in the thermoelectric properties. Scherrer and Scherrer have reported that the anisotropy ratios of BST alloys range from 2.5 to 3 in the electrical resistivity and from 2.1 to 2.5 in the thermal conductivity (54).

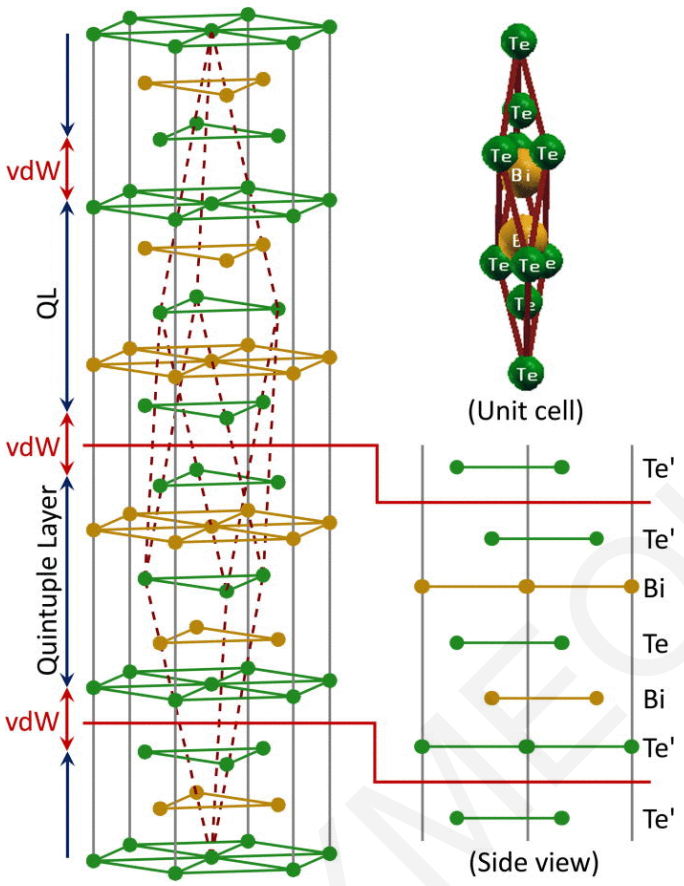

Figure 1.7. Crystal structure of Bi_2Te_3 (left), A separate rhombohedral unit cell structure (Top right), Side view of a quintuple layer (Te'-Bi-Te-Bi-Te') (Bottom right) (55).

Antisite defects: The existence of antisite defects Bi_{Te} and Sb_{Te}, has been verified in crystals of n-type Bi_2Te_3 and p-type Sb_2Te_3, respectively. As both compounds belong to the same crystallographic group, the origin of the hole carrier concentration in the solid solution $Bi_xSb_{2-x}Te_3$ (x = 0 to 2) are well explained by the formation of various antisite defects of Sb_{Te} and Bi_{Te}, which are created during the crystal growth (cations occupy the vacant anion sites) (56). A small difference in the electronegativity of the atoms forming the compound (X_{Sb} = 1.9, X_{Bi} = 1.8 and X_{Te} = 2.1) leads to low bond polarity and the formation of antisite defects (57), (58). Below is described how the antisite defects affect the hole carrier concentration in BST compounds.

Increase of hole carrier concentration: In Bi_2Te_3 compounds, formation of native defects and their concentration depend on the over-stoichiometry of Bi atoms when prepared from a

stoichiometric melt. This is due to Te's low vapor point. Presence of over-stoichiometric Bi atoms can induce defects such as: Vacancies in tellurium sublattice $V_{Te}^{\bullet\bullet}$ carrying two positive charges, antisite defects Bi_{Te}'carrying one negative charge and vacancies in Bi sublattice V_{Bi}'''carrying three negative charges. The process of creation and interaction of native defects approaches to an equilibrium state, which can be expressed by equation 12, and shows the creation of 4 extra holes, resulting in the increase of hole carrier concentration (59).

$$Bi_{Bi} + V_{Te}^{\bullet\bullet} + 2e' \rightarrow Bi_{Te}' + V_{Bi}''' + 4h^{\bullet} \qquad (12)$$

Decrease of hole carrier concentration: Navratil et al. (60) described the interaction of vacancies with the antisite defects that are present in $Bi_xSb_{2-x}Te_3$ solid solution. This interaction can be described as:

$$2V'_{Bi} + 3V_{Te} + Bi'_{Te} = V'_{Bi} + Bi_{Bi}^{x} + 4V_{Te} + 3e' \qquad (13)$$

$$2V'_{Sb} + 3V_{Te} + Sb'_{Te} = V'_{Sb} + Sb_{Sb}^{x} + 4V_{Te} + 3e' \qquad (14)$$

where Bi_{Bi} denotes a Bi atom on a regular Bi site, V'_{Te} is Te vacancy, V'_{Bi} is Bi vacancy, V'_{Sb} is Sb vacancy and e' is the produced electron, which can compensate and cause a decrease of hole concentration.

Because the thermoelectric properties such as the electrical resistivity and the Seebeck coefficient are related with the concentration of charge carriers, ZT could be controlled by the anti-site defects. Figure 1.8 presents a schematic diagram of the antisite defects in BST crystal.

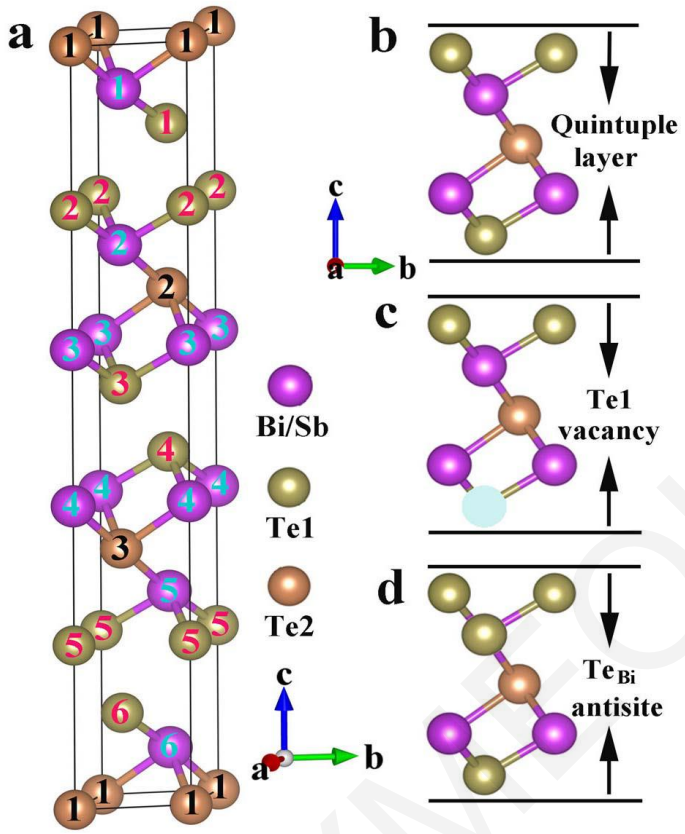

Figure 1.8. *(a) The hexagonal unit cell of BST, and (b) side view of the quintuple layer structure of perfect bulk, (c) Te_1 vacancy, and (d) Te goes to Bi position and create Te_{Bi} antisite defects* (61).

1.3.2.1 Bulk $Bi_{0.5}Sb_{1.5}Te_3$

In this section, a brief survey of BST bulk alloys will be given. Two different approaches have been adopted in the efforts to optimize BST alloys. The first is the bottom-up approach, which entails the incorporation of nanostructures into bulk materials via ball milling (62), melt spinning (63) or low-temperature hydrothermal synthesis (64) followed by hot press or spark plasma sintering to obtain bulk alloys (65). One of the highest ZT values that have been reported until today is by Fan et al. (66). This high ZT corresponds to p-type $Bi_{0.4}Sb_{1.6}Te_3$. Nanocomposites were obtained by a rapid and high throughput method of mixing nanostructured $Bi_{0.4}Sb_{1.6}Te_3$ particles obtained through melt spinning with micron-size particles obtained via solid state reaction. A maximum ZT of 1.8 at 43°C was obtained in the case of 40 wt% nano-inclusions. However, the orientation of the samples and the direction of the measurements were not discussed in the published article. Jiang et al. (67) achieved maximum

ZT of 1.14 at 350K for the composition of 24%Bi2Te3-76%Sb2Te3 with 3 wt% excess Te, prepared by zone melting method and measuring all the properties along the same direction. In 2008, Poudel et al. (68) reported the highest ZT of 1.4 at 373K for $Bi_{0.5}Sb_{1.5}Te_3$ alloys prepared using a bottom-up approach (ball milling and hot press method). However, the maximum ZT values are confined in a narrow temperature range near room temperature; the ZT decreases drastically with increasing temperature, falling to 0.8 at 523K, because of intrinsic conduction becoming dominant.. In the same time, one interesting article was published by Ma et al. (62) who achieved a ZT of 1.3 at 373K by ball milling elemental chunks of Bi, Sb, Te and hot pressing them, omitting the first step of the usual preparation method of BST samples, the melting process. The thermal conductivity was measured in the same way reported by Poudel et al.

The second approach is the top-down one, which involves hot press or spark plasma sintering followed by hot deformation, in order to induce in-situ nanostructures and more lattice defects (69), (70), (71). These efforts have resulted in high ZT values over these years. The first attempt was reported by Shen et al. (71). They hot pressed BST powders and then hot deformed them in order to induce in situ nanostructures by partial recrystallization and high density lattice defects into the materials, which exhibited a high ZT value about 1.1. Jiang et al. (2) prepared nanostructured BST prepared via ball milling following by SPS and hot deformation methods. As a result, a high ZT value of 1.56 at 50°C was obtained measuring all the properties in the same direction. In 2014, Hu et al. (69) tried to optimize the ZT of BST at higher temperatures by suppressing the intrinsic conduction through substitution of Bi atoms with Sb atoms. They reported a ZT of 1.3 at 380K and an average ZT of 1.18 in the range of 300-480K for $Bi_{0.3}Sb_{1.7}Te_3$ alloys prepared by a top-down approach, i.e., ball milling followed by hot press and hot deformation methods.

In the reports on the thermoelectric properties of BST alloys, there exists a wide variation in ZT values, ranging from 0.4 to 1.8 for samples with similar compositions. It can be deduced that the structure anisotropy, the orientation and compositional characteristics of the BST alloys play an important role in the thermoelectric performance. Figure 1.9 summarizes the results of the various authors that have been mentioned in this section. It must be remembered that the accurate calculation of ZT value is not simple, due to the anisotropy of the BST material.

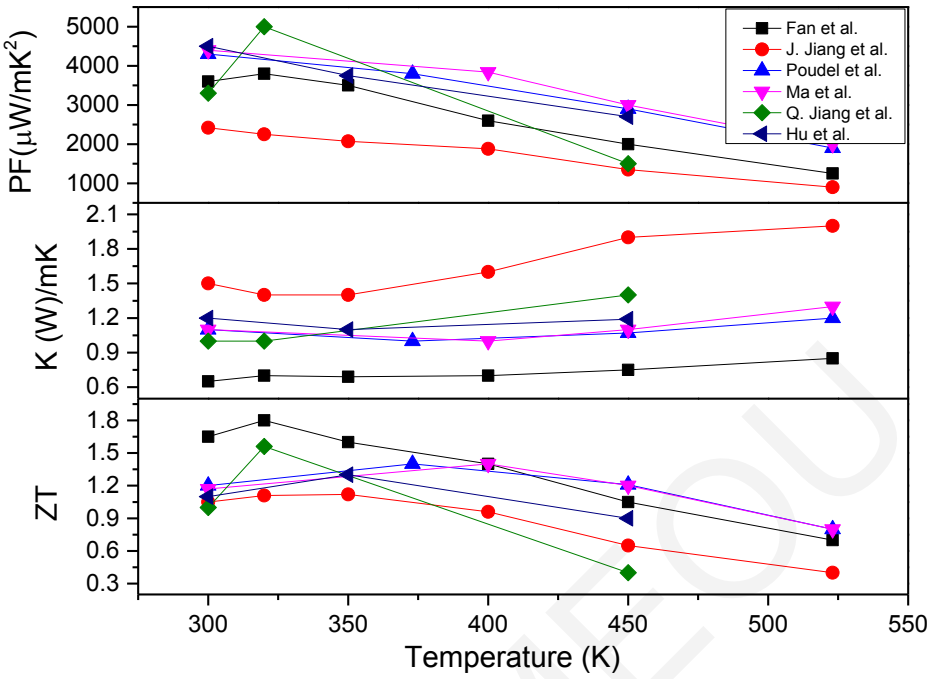

Figure 1.9. Plot of PF, κ and ZT as a function of temperature of the various works that have been mentioned in this section. It is poited out that Fan et al. did not discuss the orientation of the BST samples and the direction of thermal conductivity measured.

1.3.2.2 $Bi_{0.5}Sb_{1.5}Te_3$Thin films

Bi_2Te_3 or Sb_2Te_3 based thin films are also of great interest because thin film technology has brought a new perspective to the integration of thermoelectric cooling devices into microelectronic systems for thermal management purposes. Also, many groups have reported that ZT of low-dimensional Bi_2Te_3- or Sb_2Te_3-based thin films can be significantly improved. Hicks and Dresselhaus (41) theoretically predicted that ZT can be increased to 4-8 by using nanoscale superlattice structure, which could be achieved in Bi_2Te_3/Sb_2Te_3 thin film superlattices. Venkatasubramanian et al. (25) has verified this prediction with Bi_2Te_3/Sb_2Te_3 superlattice structures grown by chemical-vapor deposition and found a ZT of 2.4. They explained that this high ZT value (in the direction perpendicular to the layers of Bi_2Te_3) was attributed to the low lattice thermal conductivity of 0.24 Wm/K and to the cross-plane electron mobility which is equal to the in-plane electron mobility. This does not apply to bulk Bi_2Te_3

since the cross-plane mobility is less than half of the in-plane mobility. This high ZT value has not be confirmed by other groups yet (18).

Several techniques have been employed to deposit BST thin films on a variety of substrates including: flash evaporation (72), (73) radio-frequency sputtering (74), (75) direct current magnetron sputtering (76), pulsed laser deposition (PLD) (77), (78) and metalorganic chemical vapor deposition (MOCVD) (79), in order to achieve good thermoelectric properties by varying the substrate temperature or by annealing treatment. Nevertheless, the deposition of BST thin films with bulk-like thermoelectric properties remains a challenge because of issues related to stoichiometry and antisite defects. Next, a brief survey of BST thin films is provided with emphasis on the PF value reported.

Lin et al. have reported the influence of annealing temperature on crystallinity and thermoelectric properties of BST films deposited by RF magnetron sputtering on SiO_2/Si substrates. The highest obtained value of PF was 1120 $\mu W/mK^2$ at RT for a film annealed at 250°C for 10min in argon atmosphere (75). Kim et al. have reported that BST thin films, prepared by co-sputtering on SiO_2/Si substrates and annealed at 400°C for 10 min, exhibit a PF of 1120 $\mu W/mK^2$. The annealing was performed under a reductive atmosphere of flowing Ar gas with 10% H_2 (80). Jeon et al. (74) examined the microstructure evolution of sputtered BST films grown on SiO_2/Si during post-annealing and its effects on their thermoelectric properties. The highest PF obtained was 1700 $\mu W/mK^2$ for a film annealed at 200°C in vacuum for 12h. The highlight of this paper is that the post annealing prompted a drastic grain growth. Bourgault et al. have reported that BST films, deposited by direct current magnetron sputtering on Al_2O_3 substrates and annealed under argon atmosphere at 300°C for 16h, could achieve a PF value of 2000 $\mu W/mK^2$ (81). Also they observed that the films grown on glass substrates had a PF of 1600 $\mu W/mK^2$ after annealing at 300°C for 16h. Zheng et al. have recently reported that BST films, grown at room temperature on fused silica by ion beam sputtering, exhibit a PF of 2670 $\mu W/mK^2$ following annealing in vacuum at 300°C for 1h (82). In 2008, Takashiri et al. (83) reported that BST films, prepared by flash evaporation method on glass substrate heated at 200°C and then annealed at 300°C for 1h in Ar atmosphere, could achieve a PF value of 1220 $\mu W/mK^2$. In 2010, the same authors reported (84) that BST films, grown with the same conditions as the previous report but annealed at 300°C in H_2 atmosphere for 1h, had PF of 3560

$\mu W/mK^2$. In 2014, Takashiri et al. (85) tried again to anneal films over 300°C in H_2 atmosphere and observed that the PF of BST films decreases as the annealing temperature increased.

Therefore, it is evident that substrate type and temperature, thin film growth technique and post annealing processing are crucial factors to be determined for optimization of the thermoelectric properties of BST films. While in most cases an enhancement in the thermoelectric properties is observed in comparison to those of the as-deposited films, the achieved PF value remains low in comparison to the bulk value (86). In addition, in most of the thin-film studies, the ZT value has been calculated making the assumption that the thermal conductivity value of the BST films is similar to the one observed in the best bulk materials because it is a great challenge to measure it accurately in thin films and in the same direction that resistivity and Seebeck coefficients are measured. However, taking into consideration that phonons in thin films undergo additional scattering at surfaces and interfaces, it is expected that the thermal conductivity of the films is lower than that of the bulk ZT and thus the ZT of the films is expected to be higher than that of the bulk materials given that films and bulk materials have similar PF values.

1.4 Summary

Climate change along with energy consumption and demand are some of the critical problems we face today. All these issues require a more efficient use of primary energy that comes from fossil fuels. Thermoelectric devices are of interest for applications as power generators and heat pumps, which interconvert heat and electricity via the Seebeck and the Peltier effect, respectively. The performance of these solid state thermoelectric energy converters depends on the dimensionless thermoelectric figure of merit (*ZT*) of the materials, given by $ZT=S^2T/\rho.\kappa$, where S, ρ, κ, and T are the Seebeck coefficient, electrical resistivity, total thermal conductivity, and absolute temperature, respectively. A good thermoelectric material must combine a large Seebeck coefficient S with low electrical resistivity ρ and low thermal conductivity κ. Another crucial criterion to characterize thermoelectric materials is the power factor, defined as $PF= S^2/\rho$.

Bulk $Bi_{0.5}Sb_{1.5}Te_3$ (BST) is considered as a state-of-the-art p-type thermoelectric material in the temperature range 273-473K because it exhibits high ZT and PF and low thermal conductivity over this temperature range. It has been established that the most large-grained p-type BST

samples have a maximum ZT at about 1 and with nanostructured BST samples the ZT can substantially be higher (~ 1.5). An increases of the energy gap by changing the Bi/Sb ratio can give the advantage to elevate the ZT to higher temperatures. Meanwhile, Bi_2Te_3 or Sb_2Te_3 based thin films are of great interest because thin film technology has brought a new perspective to the integration of thermoelectric cooling devices into microelectronic systems for thermal management purposes. Nevertheless, the deposition of BST thin films with bulk-like thermoelectric properties remains a great challenge, with the PF values ranging from 1000 to 3500 $\mu W/mK^{2.}$ The determination of the substrate type and temperature, growth technique and post annealing processing is crucial for the optimization of the BST films.

This work is divided in two parts. The objective of the first part concerns the growth of BST films, by pulsed laser deposition, with bulk-like thermoelectric properties. In the second part, we are dealing with the preparation and thermoelectric characterization of bulk BST samples with the objective to achieve similar or higher ZT than the highest reported value.

Chapter 2

2. Experimental methods

The techniques used for the growth and the characterization of the BST materials studied in this thesis are discussed in this chapter. We have grown p-type BST thin films using pulsed laser deposition and BST bulk samples using hot press/deformation method. The structure, morphology and chemical stoichiometry of the BST thin films and bulk samples were characterized using techniques such as X-ray diffraction (XRD), scanning electron microscopy (SEM) and energy dispersive X-ray spectroscopy (EDX), respectively. The temperature dependence (250 to 390K) of the electrical resistivity, Hall coefficient and Seebeck was measured using a commercial physical properties measurements system (PPMS, Quantum Design). Laser flash technique (LFA) was used for thermal conductivity measurements on the BST bulk samples, in the temperature range of 300-390K.

2.1 Synthesis and growth techniques

2.1.1 Synthesis of $Bi_{0.5}Sb_{1.5}Te_3$ bulk samples

High purity (5N) Bi, Sb and Te granules were weighted according to the formula $Bi_{0.5-x}Sb_{1.5+x}Te_3$ (x=0-0.3); then an excess amount of Te (4 %wt) was added to the metal mixture to compensate for the loss of Te that is expected to occur during heating because of its low vapor point (277°C at 10^{-4} Torr). The metal mixture was loaded into a quartz tube that was sealed under vacuum at 10^{-3}Pa. The sealed quartz tube was heated at 850°C for 10 hours to ensure composition homogeneity, and then it was cooled slowly to room temperature. The obtained ingot was crushed, and grounded into powder that was characterized by XRD. For the compaction process, the powder was loaded in a cylindrical graphite die (inside diameter =13mm) and hot-pressed at 420°C for 1 hour under an axial pressure of 80MPa. For the HD

process, the powder was initially loaded in a cylindrical graphite die with an inner diameter of 10mm and hot-pressed at 340°C for 1 hour under 80MPa. Subsequently, the hot-pressed cylindrical sample was placed in the center of a larger graphite die with an inner diameter of 13mm and was re-pressed at 500°C for 1 hour under 40MPa.

2.1.2 Synthesis of $Bi_{0.5}Sb_{1.5}Te_3$ PLD targets

For the synthesis of the powder used to fabricate the PLD targets, high purity (5N) Bi, Sb and Te powders were used, according to the desired stoichiometry. The synthesis was done by mixing the constituent metals, inserting the mixture in evacuated and sealed quartz ampoules and melting the mixture at 850°C for 10 hours. The obtained ingots were ground using an agate mortar and pestle. The resulted fine powder was **cold pressed** at 5tons into 13mm diameter disks. Figure 2.1 shows a) the obtained BST ingot, b) which was grounded into powder and c) finally the powder cold pressed in a disk.

Figure 2.1. a) The obtained BST ingot for the melting, b) the agate mortar with the powder, c) the cold or hot press pellet.

2.1.3 Growth technique for $Bi_{0.5}Sb_{1.5}Te_3$ thin films

Pulsed laser deposition (PLD) is a physical vapor technique and can be carried out in vacuum or in the presence of a background gas. The technique of PLD has been used for growing complex multicomponent compounds because of its capability for stoichiometric transfer of material from target to substrate (87) . The detailed mechanisms of PLD are complex and include three steps, as shown in Figure 2.2. A pulsed laser beam is focused onto a target of the material to be deposited. During the first stage of the process, **the ablation process of the target material by the laser irradiation,** the laser light generates a strong electrical field which can remove the electrons from the target. The free electrons oscillate with the electromagnetic field of the laser light and can collide with the atoms of the bulk material thus transferring some of their energy to the lattice of the target material within the surface region. The surface of the target is heated up to temperatures at which all elements can evaporate (this ensures that all the elements of the target can evaporate at the same time). In the second stage, **the development of a plasma plume with high energetic ions, electrons etc.,** the material expands in a plasma plume and moves towards the substrate. The background pressure inside the PLD chamber is responsible for the distribution of the plume. The third stage, **the deposition of the ablation material on the substrate,** is important in determining the quality of the deposited films. The high energetic species ablated from the target impinge onto the substrate surface and may induce various types of damage to the substrate (88), (89).

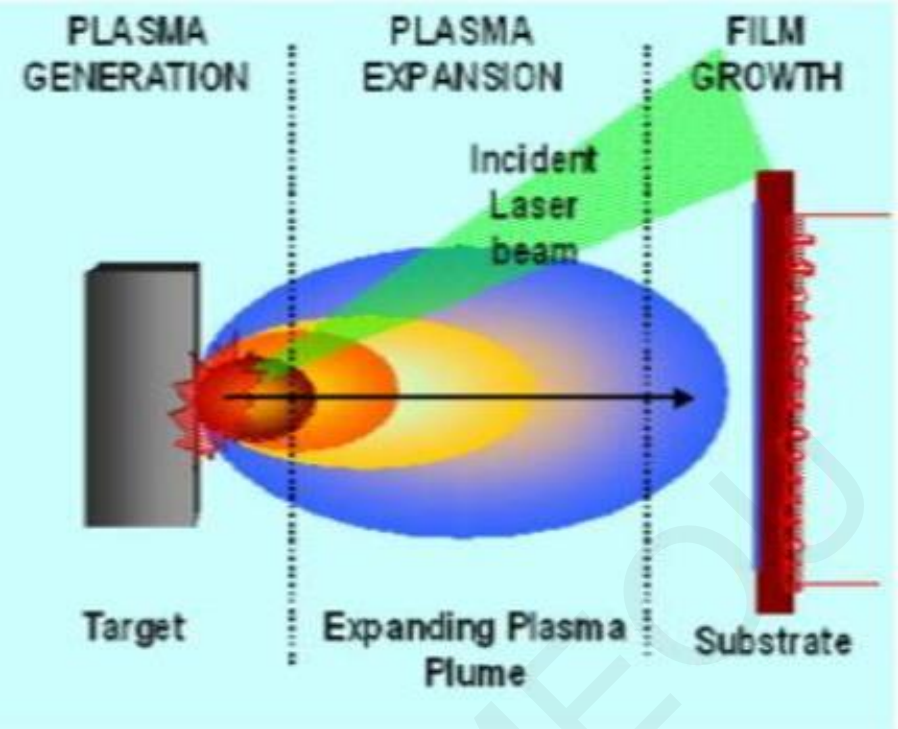

Figure 2.2. Mechanisms of PLD (three steps) (90).

Many experimental parameters can be changed, which then have an influence on films' properties. First, the laser parameters such as laser fluence, wavelength, pulse duration and repetition rate can be altered. Second, the preparation conditions, including target-to-substrate distance, substrate temperature, background gas and pressure, may be varied, which all influence the films growth. In Chapter 3, we have carried out a systematic investigation of the condition parameters, which are far from being independent and affect the growth and quality of the resulting BST films. The configuration of the PLD technique is illustrated in Figure 2.3.

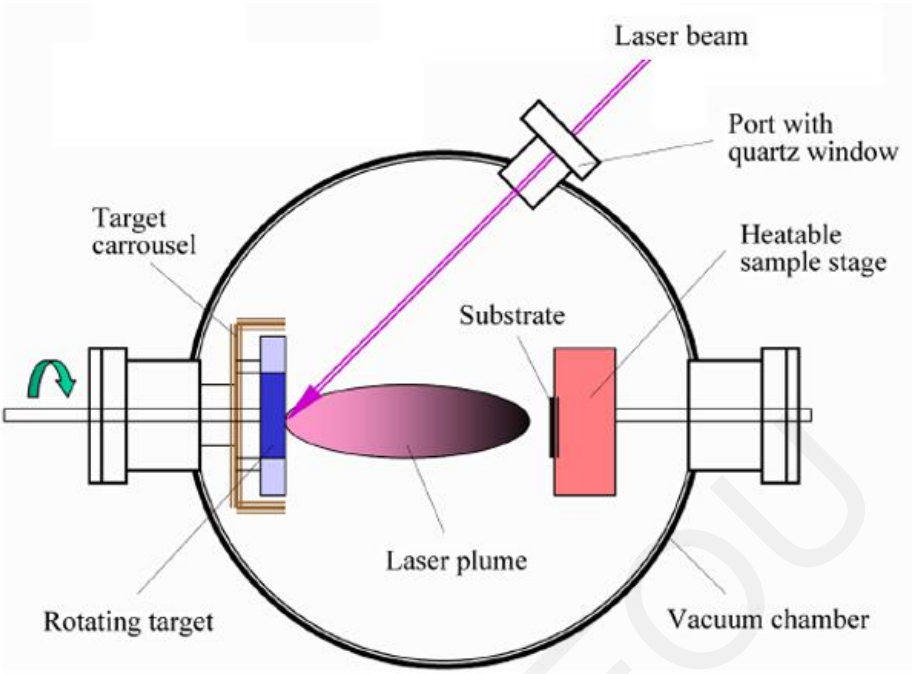

Figure 2.3. Configuration of the PLD technique.

A **krypton fluoride (KrF) excimer laser*** (Coherent COMPex Pro 201 F) was used in order to deposit the BST films, with a wavelength of 248 nm and repetition rate in the range of 1-10Hz. The maximum energy per pulse is 700mJ and the pulse duration is τ~25ns (91). A metal rectangular mask was used for selecting the homogenous part of the laser beam. An arrangement of mirrors was used to direct the beam inside the deposition chamber and a focusing lens was used to focus the beam onto the target. The substrate was mounted on a sample holder with mechanical contact. The sample holder could be heated to 800°C with a PID controller. The pressure inside the deposition chamber was controlled with a turbo pump in combination with a mechanical pump. More detailed information about the deposition conditions used is mentioned in Chapter 3. Figure 2.4 shows the PLD system used for the BST thin film depositions.

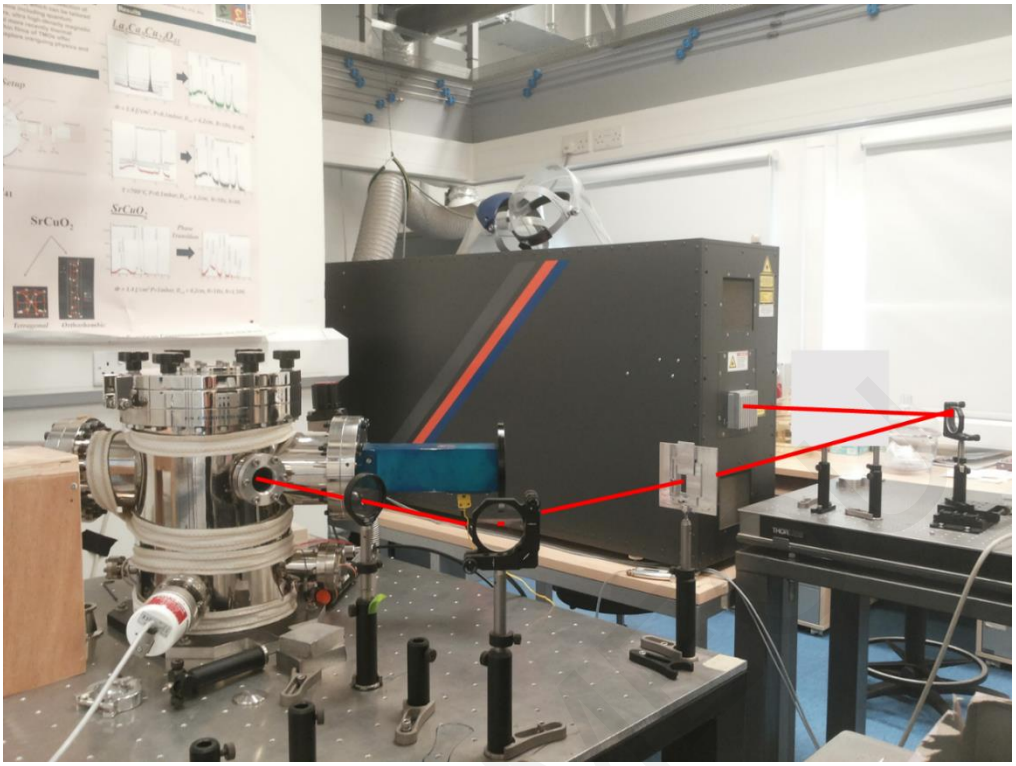

Figure 2.4. PLD system in our Lab. The red line presents the path of the laser beam to the chamber.

* An excimer (excited dimer) is a short-lived dimeric or heterodimeric molecule formed from two species, at least one of which is in an electronic excited state. Excimers are often diatomic and are formed between two atoms or molecules that would not bond if both were in the ground state. The excimer molecules are formed in a gaseous mixture of the component gases of Kr, F2 and Ne. Excimer lasers can be described as the most powerful in the ultra-violet (UV) region of the electromagnetic spectrum (92).

2.2 Characterization techniques

2.2.1 Structure, morphology and stoichiometric characterization techniques

X-Ray diffraction (XRD)

The crystalline structures of the BST films/ bulk were analyzed by X-ray diffraction (XRD) using a 9 kW rotating anode (SmartLab) Rigaku diffractometer. The XRD data were collected in the 2θ range from 10 to 90° with a step of 1°/min. X-Ray diffraction is a nondestructive technique and is used for qualitative/quantitative determination of the phases present and the crystallographic structure (lattice parameters, crystallographic orientation and grain size) of the investigated materials, because the electromagnetic radiation that used, has wavelengths comparable with the inter-atomic distances within the solid structures. The periodicity of the crystal structure creates geometrical arrangements on crystallographic planes and when the incident electromagnetic waves interact with them and are in agreement with Bragg's law, diffraction can occur. Bragg's law (Figure 2.5) is expressed though the equation: $2d_{hkl}.\sin\theta=n.\lambda$, where d_{hkl}, θ, n, λ are the inter-planar spacing, the incident angle, the order of the diffraction and the wavelength of the X – rays used in the experiment, respectively (93), (94).

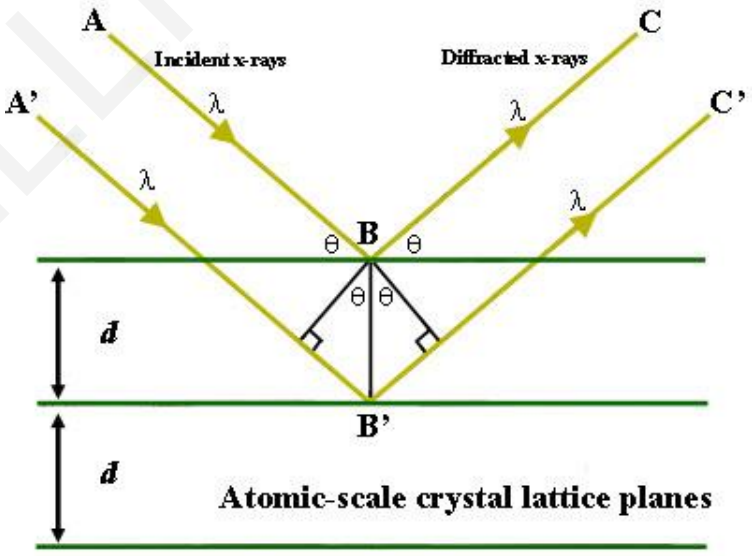

Figure 2.5. Bragg's law (95).

Scanning Electron Microscopy (SEM) and Energy dispersive spectroscopy (EDX)

Scanning electron microscopy (SEM) involves the scanning of the sample's surface with a high energy beam of electrons and provides information about sample morphology and topography (96). SEM images were collected with a Tescan Vega LSU, with an acceleration voltage of 20KV or with a JEOL, JSM-6610LV SEM. For the investigation of the morphology of the samples, secondary electrons were used to image the surface of the samples (for films: grains, splashes, cracks and for bulk: grains morphology, size and orientation). Backscattered electron imaging was used to detect the existence of secondary phases on the PLD target and BST bulk samples. The SEM system is also equipped with an Energy Dispersive X – Ray Spectrometer system (EDX) which was employed for the elemental analysis of the samples. EDX exploits the x-rays emitted due to the interactions between electromagnetic radiation and matter, and provides information about the samples composition. EDX spectra were collected under the same conditions (accelerating voltage, beam current, magnification, dead time and acquisition time) from at least three different regions of each sample. Quantitative analysis of the different elements (atomic percent concentration) was performed by a standard-less analysis with 5% accuracy.

2.2.2 Thermoelectric characterization techniques

Thermoelectric properties

The temperature dependence of electrical resistivity and Seebeck coefficient as well as the Hall coefficient at 300K were measured using a commercial **Physical Properties Measurement System (PPMS, Quantum Design)**. The Seebeck coefficient was measured using the steady state technique with thermal gradients of 1% of the measurement temperature and miniature Cernox temperature sensors. The distance between the voltage leads as well as the temperature

sensors was about 1 mm. The electrical resistivity was measured using the four-probe ac method. Electrical resistivity and Seebeck coefficient were measured simultaneously on samples with width of 5 mm and length of 10 mm using the Thermal Transport Option (TTO) of PPMS. The total relative errors in the measurements of electrical resistivity and thermopower were 5%, 7% respectively. A picture of a typical sample configuration is shown in Fig. 2.6.

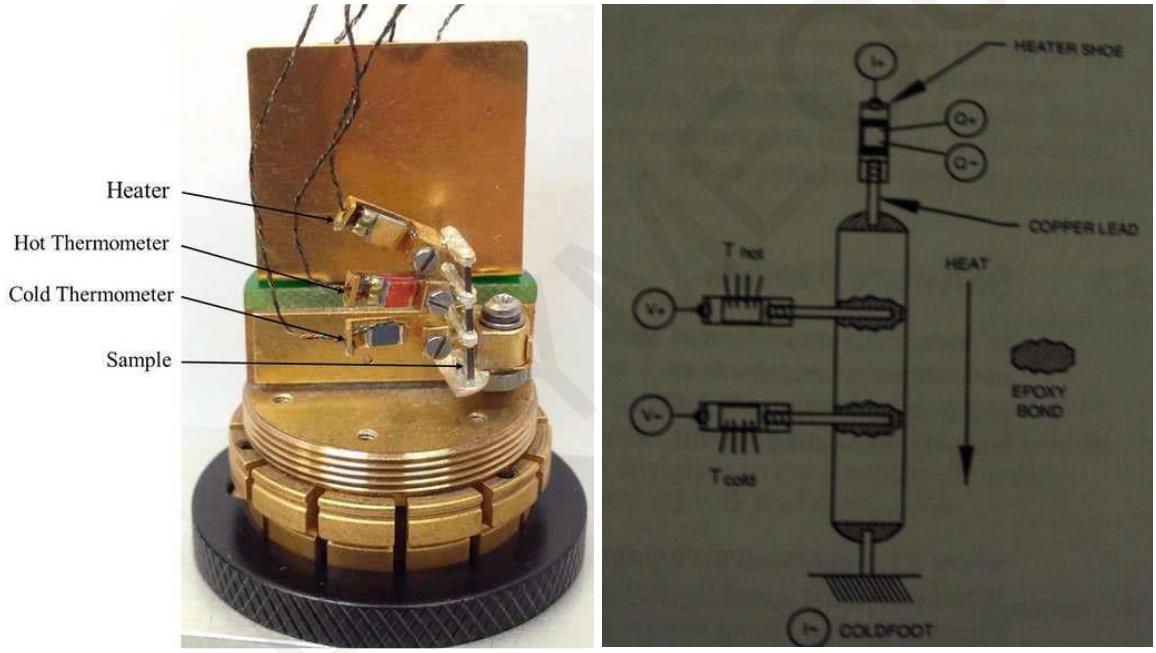

Figure 2.6. Thermal and electrical connections for an investigated sample (97).

Hall coefficient measurement

The Hall coefficient (R_H) was measured using the Van der Pauw technique (98) under a magnetic field of 2 T and a dc current of 2mA for the BST films and 20mA for the BST bulk samples. The currents were applied on the surface of the samples with four contacts along their edge, as shown in Figure 2.7. The combination of the Hall coefficient with the resistivity gives the type of the carrier (n-type / p-type), the carrier density and the mobility of the samples. The

carrier concentration and in-plane Hall mobility were calculated using $n_H = -1/(e.R_H)$ and $\mu_H = 1/(n_H .e. \rho)$, respectively. The total relative errors in the measurement was 5%.

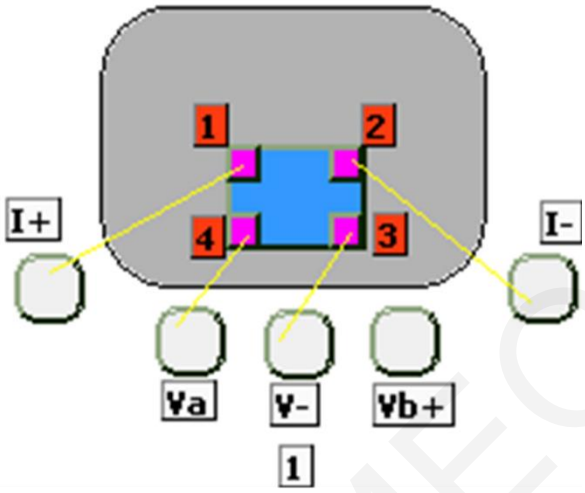

Figure 2.7. Sample mounting for Hall measurements.

Thermal conductivity measurement in the bulk BST samples

Thermal conductivity is calculated using the relation $\kappa = D.\rho_s.C_{p,}$ where D, ρ and C_p is the thermal diffusivity, the density and the specific heat of the sample, respectively. The thermal diffusivity (D) of the BST bulk samples was measured using a **Netzsch Laser Flash Apparatus LFA-457** system from room temperature to 375K. A short laser pulse is used for heating the upper surface of the sample. The absorbed heat propagates through the sample and causes a temperature increase on the rear surface. The infrared detector measures this temperature rise versus time. The samples were coating by graphite spray in order to maximize the amount of thermal energy transmitted from the irradiated surface of the sample to the upper surface and to maximize the signal observed by the infrared detector (99). The relative densities (ρ_s) of the samples were estimated by an ordinary dimension and weight measurement procedure and the specific heat (C_p) was calculated theoretically for each composition (100), (101). Figure 2.8 shows a schematic representation of the Netzsch Laser Flash Apparatus LFA-457 system used in our studies.

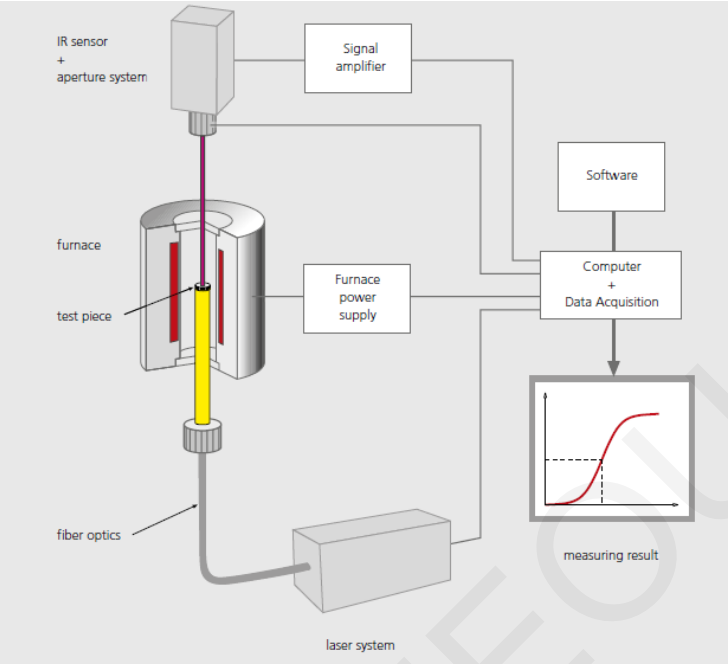

Figure 2.8. A schematic diagram of using a Netzsch Laser Flash Apparatus LFA-457 system.

BST samples, as I mentioned previously, are highly anisotropic and ZT could be overestimated significantly if the thermoelectric properties (S, ρ and κ) of BST samples are measured along different directions. In order to investigate the in-plane thermal conductivity of BST samples, we used the method introduced by Xie et al. (3) which I will describe it briefly in Chapter 4.

Chapter 3

$Bi_{0.5}Sb_{1.5}Te_3$ thin films

As we mentioned above, $Bi_{0.5}Sb_{1.5}Te_3$ (BST) is considered to be a state-of-the-art p-type thermoelectric material, for temperatures near room temperature with a relatively high ZT value (1.1-1.5). While this value is very encouraging, there is much more work to be done in order to develop higher-efficiency thermoelectric devices. The majority of thermoelectric applications requires devices based on bulk materials. However, there are several applications where small heat loads or low levels of power generation are involved, e.g., localized cooling in micro- and nano-electronics as well as energy autonomy in applications such as wireless sensor networks and wearable electronics, which could be well served by thin-film thermoelectric devices fabricated on rigid and/or flexible substrates (9), (102). Nevertheless, the deposition of BST thin films with bulk-like thermoelectric properties remains a challenge. Understanding the factors that influence the thermoelectric properties of BST films requires further systematic investigations. The objective of this part of my work concerns the growth of BST films with bulk-like thermoelectric properties (PF= 3770 $\mu V/K^2m$ at 390K). It is noted that if the films and bulk materials have the same PF, the ZT of the films is expected to be higher due to the lower thermal conductivity of thin films in comparison to the bulk counterpart materials. Our results, concerning the PF value of the BST films, are very encouraging.

3.1 Growth of $Bi_{0.5}Sb_{1.5}Te_3$ thin films

3.1.1 Motivation

As there are not many works on the growth of BST films by PLD, during the first part of this Thesis we have carried out a systematic investigation of the condition parameters which are far from being independent and affect the growth and quality of the resulting BST films. We deposited BST films with different fluence and various substrate temperatures between room temperature and 350°C in order to obtain the optimum growth conditions, which result in the best PF. Films with different thicknesses were produced in order to investigate the effect of

thickness on PF. Part of the work presented in this Chapter has been published in Applied Surface Science 336 (2015) 138–142.

3.1.2 Experimental

Target selection: The first report about PLD grown Bi_2Te_3 thin films was published in 1996 by Dauscher et al. (103). They reported that the films are deficient in Te due to the interaction of the incoming laser with the plasma plume. Christen et al. (104) reported that the stoichiometric removal of the material from the target, does not lead every time to the growth of stoichiometric materials. When growing composite materials, for which one of the element is more volatile than others, re-evaporation may occur from the growth surface and as a consequence the grown films become non-stoichiometric. In the case of BST, Te is more volatile than Bi and Sb and the use of an additional amount of Te in the target, is required. In our case, we used BST targets with an extra 1%wt Te ($Bi_{10}Sb_{30}Te_{60+1\%wt}$).

Substrate selection: We have chosen to use inexpensive fused silica substrates because they are amorphous and, hence, are expected to affect the crystallographic texture of the grown thin films differently than single crystal substrates. In addition, they have low thermal conductivity, which is an advantage for thermoelectric applications because it reduces heat leaks and aids in maintaining a temperature gradient along the film.

Growth of BST films: BST thin films were deposited using a KrF laser (λ = 248nm) with a pulse duration of 25 ns at a pulse repetition rate of 10 Hz. The laser beam was incident at an angle of ~45° with respect to the target surface. The home-made target was rotating during ablation to avoid local heating of the target. The distance between the target and the substrate was kept at ~4 cm. A vacuum system comprised of a rotary and a turbomolecular pump evacuated the deposition chamber to a base pressure of $< 5 \times 10^{-5}$ mbar before high purity (99.999%) argon gas was introduced. During the deposition the ambient pressure was ~ 0.13 mbar. Prior to deposition the substrates underwent cleaning; specifically, they were cleaned thoroughly in an ultrasonic bath with acetone, ethanol and isopropanol.

Target synthesis: For the preparation of the PLD targets, we have followed the procedure that was described in Chapter 2: 2.1.2: Synthesis of BST PLD targets.

3.1.3 Effect of Fluence

The stoichiometric removal of material from a target is unquestionably the most important factor in the success of PLD and can be achieved by the optimization of the laser fluence. Zeipl et al. (105) deposited Bi_2Te_3 thin films by PLD, using fluences from 2 to 10 J/cm^2, and found that their films appear to be very far from stoichiometry when using high fluence. As the fluence decreased the films became more stoichiometric. Based on this report, we chose laser fluences between 0.3 J/cm^2 and 2.2 J/cm^2 in order to study the stoichiometric transfer from the target on the substrate with reasonable growth rate and reduced particulate density. The BST films were studied accordingly for their structure and stoichiometry. The room temperature depositions took place in Ar atmosphere with 525 pulses.

To calculate the fluence or the energy density of the laser beam, the spot area on the surface of the target was determined. To take the beam imprint, we placed a photograph sheet inside the chamber at the target position. The spot size was determined by measuring the beam spot area on this photograph sheet from a single laser pulse. By measuring the energy of the beam before and after the optical component, we determined the energy which is lost until the laser beam arrived at the target and it was about 8%. The laser fluence, F, at the surface of the target was calculated by F= (energy of the laser x 8%) / spot area.

Table 3.1 shows the EDX composition results versus different fluence. It is evident, using fluences below 1.5 J/cm^2 results in films with slight deficiency in Bi whereas for fluences above 2 J/cm^2 the films are deficient in Te. As the laser fluence increased, an ablation threshold is reached where laser energy absorption is higher than needed for evaporation. Furthermore, laser ablation can affect the particle size and density, as shown in Figure 3.1a and b, where the laser fluence decreased from 2 J/cm^2 to 0.3 J/cm^2. It is pointed out that, the overall film composition for the BST film with F=0.3 J/cm^2 was different, because the particles have different phase. The optimum stoichiometry was achieved using a fluence between 1.5 J/cm^2 and 2 J/cm^2. Based on these results, the rest of the depositions were carried out using the fluence of 2 J/cm^2.

F (J/cm^2)	Bi (at %)	Sb (at %)	Te (at %)
F=2.2	10.23	31.70	58.06
F=2	10.28	29.70	60.01
F=2	10.33	30.11	59.55
F=1.7	10.51	30.22	59.26
F=1.5	10.15	30.14	59.70
F=1	9.39	27.00	63.60
F=0.5	8.16	30.57	61.27
F=0.3	7.67	30.28	62.04

Table 3.1. Stoichiometric analysis versus laser fluence for the BST films.

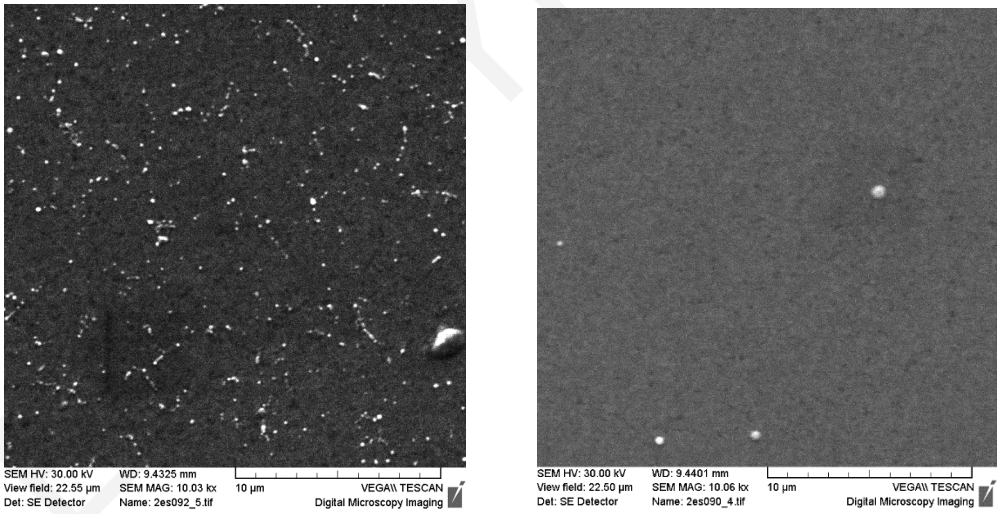

Figure 3.1. SEM images for the BST films grown with a) F=0.3 J/cm^2 and b) F=2 J/cm^2.

3.1.4 Effect of thin film thickness

In order to investigate the influence of film thickness on the thermoelectric properties of BST films, a series of samples were grown at 350°C by varying the number of laser pulses and keeping the rest of the deposition conditions identical. The thickness of the as-grown films varied between 100 nm and 480 nm and was found to be a crucial parameter for their thermoelectric properties. All samples exhibit similar XRD patterns (not shown / same as Figure 3.2); i.e., they are all fully oriented and the observed (00l) reflections indicate preferential growth along the c-axis.

Films thicker than 280nm have microcracks and the coalescence of these cracks leads to exfoliation. This effect is attributed to the large difference in the thermal expansion coefficient between the fused silica substrate ($1x10^{-6}$/K) (106) and the BST films (~$20x10^{-6}$/K). Specifically, the large thermal expansion coefficient mismatch generates cracks in the films due to the large tensile thermal strains induced upon cooling down to room temperature following the deposition of the films.

On the other hand, BST films thinner than 180nm are dense with smooth surfaces. As shown in Table 3.2, the best PF at 390K is obtained for 180 nm-thick films, i.e., PF= 2600 μW/mK^2, because of its lower resistivity than the other samples. Given that all samples are fully oriented along c-axis, we expect the effect of anisotropy to be weak, and hence, we propose that the lower resistivity value of the 180-nm thick sample is a thickness effect; i.e., the surface scattering of charge carriers is reduced resulting in the increase of the carrier mean free path (73). The fact that all samples exhibit similar Seebeck values indicates that the carrier concentration for all samples is also similar, and thus, the difference in resistivity should be related to differences in mobility.

Thickness	ρ (Ω.m)	S (μV/K)	PF (μW/K^{2}m)
100nm	$1.1x10^{-5}$	150	2150
180nm	$1 x10^{-5}$	165	2600
280nm	$1.15 x10^{-5}$	140	1650

Table 3.2. Room-temperature thermoelectric properties of BST films with different thicknesses.

3.1.5 Effect of substrate temperature

Figure 3.2 shows the XRD patterns of BST thin films deposited at different substrate temperatures, and keeping the rest of the deposition conditions identical ($F=2J/cm^2$, number of pulses 525, RR=10Hz). It is evident that the films grown at substrate temperatures lower than 150°C are amorphous and as the substrate temperature increases above 150°C the crystallinity of the films improves. The increase of the substrate temperature to 350°C is associated with the generation of new peaks in the XRD pattern. The film deposited at 350°C is fully oriented and the observed (00l) reflections indicate preferential growth along the c-axis of the BST film. SEM images (figure 3.3) from the same series of BST thin films reveal that grain size increases slightly with increasing substrate temperature showing granular structure on all three of them.

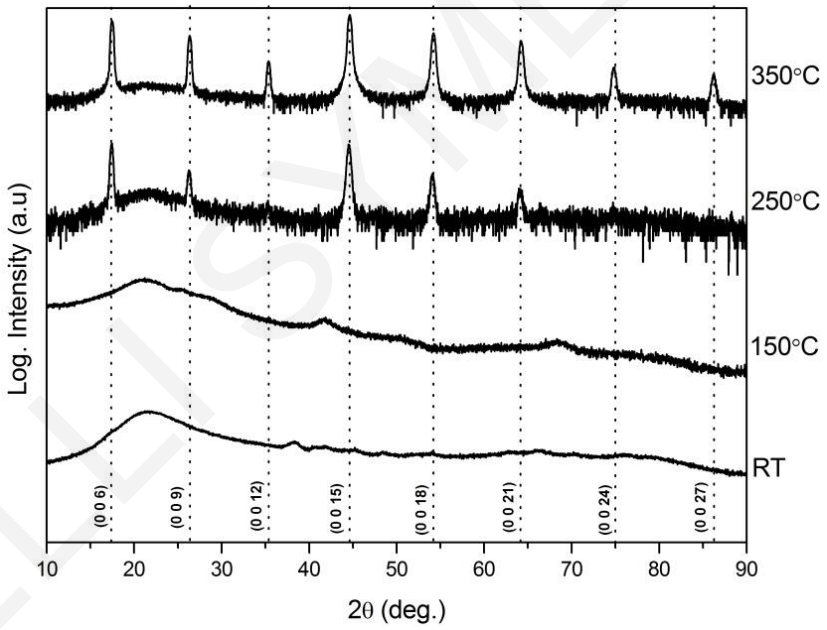

Figure 3.2. X-ray diffraction patterns obtained for BST films deposited at different substrate temperatures.

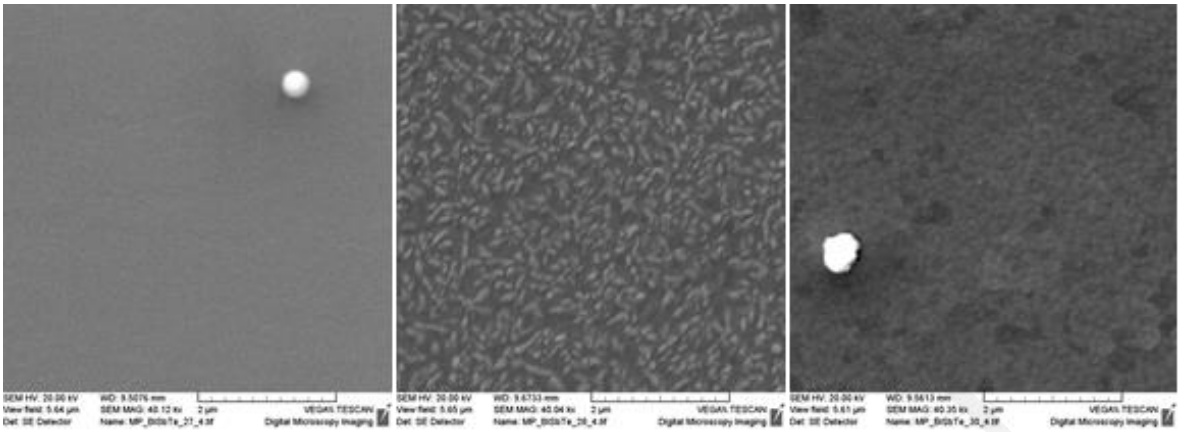

Figure 3.3. SEM of BST thin films, deposited at 150, 250 and 350 °C on fused silica substrate.

As I mentioned above, the stoichiometric transfer of material from target to film is a challenge in the case of the investigated compound as it is composed of three elements with different atomic weights and vaporization enthalpies (107). The composition of the BST films was investigated by EDX. Table 3.3 shows the composition analysis of the films deposited at different substrate temperatures and of the BST target used for their deposition by PLD. The target seems to be nearly stoichiometric concerning the atomic ratio of (Bi+Sb):Te. It is known that EDX may not be the best method to determine accurately the atomic concentration of BST samples as the peaks corresponding to Sb and Te overlap and this makes difficult the analysis of the spectra (107) . However, we suggest that by concentrating on the Bi atomic concentration it is possible to extract useful information because the Bi peak is well defined and the associated error with the deduced at% concentration is rather small. It is evident from Table 3.3 that the Bi concentration tends to increase with increasing substrate temperature possibly due to the loss of Te. We expect therefore the concentration of Bi_{Te} antisite defects to increase with a corresponding increase in the carrier concentration. This expectation is confirmed by the measured room-temperature carrier concentration values shown in the last column of table 3.3.

	Bi (at %)	Sb (at %)	Te (at %)	Carrier concentration @300K (cm^{-3})
Target composition	10.73	28.83	60.23	-
RT	8.77	29.30	61.91	-
150°C	10.40	28.99	60.61	$2.54x10^{19}$
250°C	9.38	28.83	61.78	$1.09x10^{20}$
350°C	11.65	28.17	60.17	$1.44x10^{20}$

Table 3.3*. EDX composition analysis for BST target used and films deposited at different temperatures. Room-temperature carrier concentrations for BST films deposited at 150, 250 and 350°C.*

The effect of the substrate temperature on the electrical resistivity of BST films is illustrated in Figure 3.4a. The almost-amorphous film grown at 150°C exhibits semiconducting-like behavior whereas the crystalline films grown at 250°C and 350°C exhibit metallic-like behavior. The transition from semiconducting to metallic behavior with increasing substrate temperature is attributed both (i) to the increase of the hole carrier concentration due to the increase of Bi_{Te} antisite defects and (ii) to the increase of the hole carrier mobility due to enhanced crystallinity and texturing of the films. The above reasons are the origin of the large difference in the resistivity of the samples exhibiting metallic behavior.

The effect of the substrate temperature on the Seebeck coefficient of BST films is shown in Figure 3.4b. It is evident that S tends to decrease with increasing substrate temperature. This effect is attributed to the fact that S is inversely proportional to the carrier concentration and also to the electronic anisotropy (out-of-plane S is greater that in-plane S) which is directly related with the texturing of the films. Figure 3.4c, displays the temperature dependence of the calculated power factor values for all films. The film deposited at 350°C exhibits the best PF over the entire temperature range investigated; e.g., at 390 K PF= 2600 $\mu W/K^2m$.

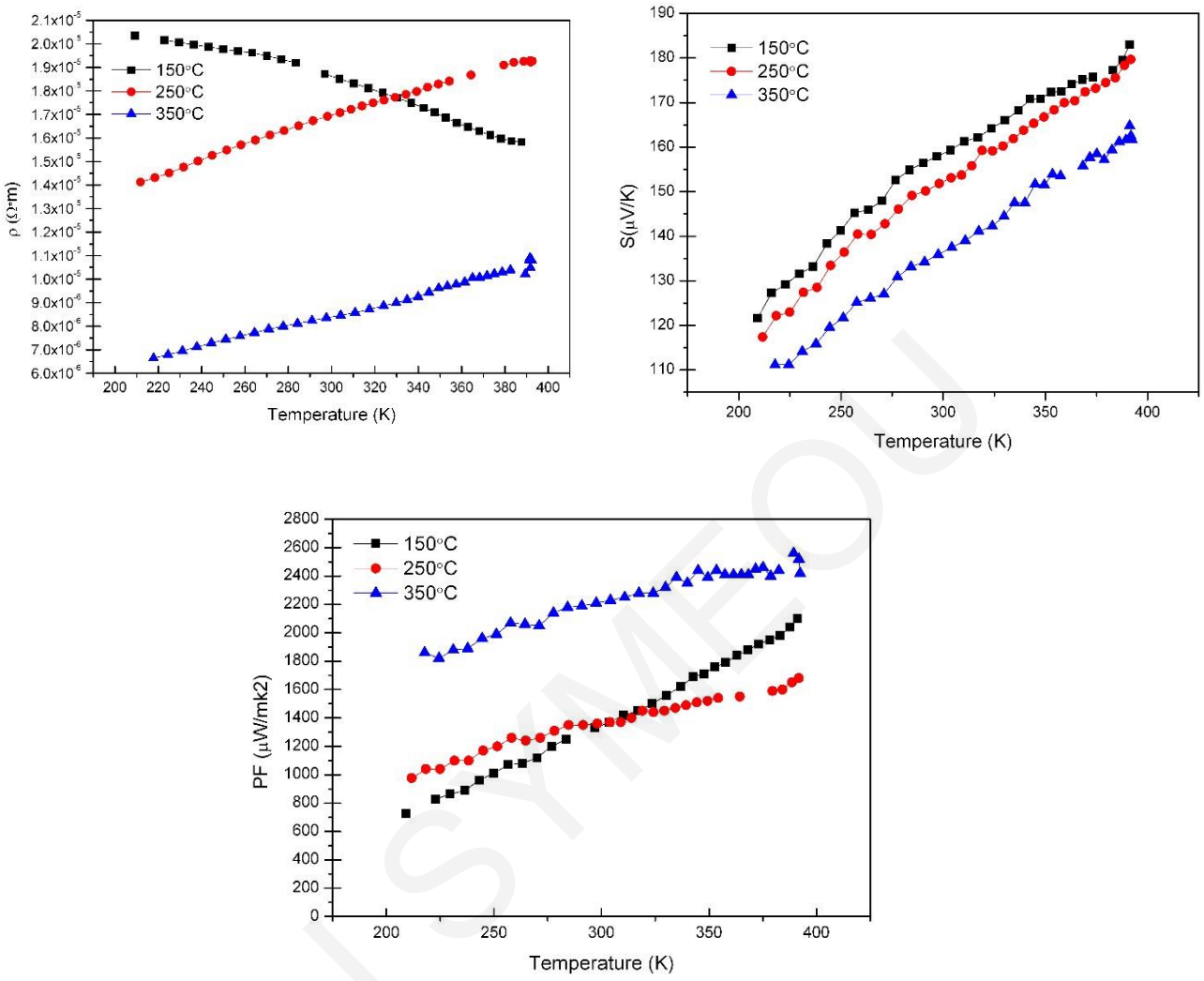

Figure 3.4. Temperature dependence of electrical and thermoelectric properties of BST films grown at different substrate temperatures: (a) electrical resistivity, (b) Seebeck coefficient, and (c) power factor.

3.1.6 Conclusions

As there are not many works on the growth of BST films by PLD, during the first part of this Thesis we have carried out a systematic investigation of the condition parameters which are far from being independent and affect the growth and quality of the resulting BST film. The optimum deposition conditions which lead to the highest PF (2600 $\mu W/K^2m$.) are summarized in Table 3.4. This PF value was still lower than the PF value of the bulk BST samples.

Substrate	F (J/cm^2)	Tsub (°C)	Thickness (nm)	RR (Hz)	Dist.Targ,-sub (cm)	Atmosphere
Fused silica	2	350	180nm / 525p	10	4	Argon (.13mbar)

Table 3.4. The optimum deposition conditions of the BST films.

3.2 Effect of post annealing

3.2.1 Motivation

Annealing has been used to relieve large thermal stresses, alter defect concentration and control stoichiometry of materials, thereby altering the carrier concentration. However, the thermoelectric properties of films are not affected by only the carrier concentration but also by grain size and grain orientation, which can also be modified during the annealing process. Therefore, in order to enhance the PF of the grown BST films, we investigated the effect of the three major annealing parameters, atmosphere, temperature and time, on the thermoelectric properties (Seebeck coefficient and resistivity).

The aim of this study was to initially obtain pulsed laser deposition-prepared BST films with bulk-like thermoelectric properties on fused silica substrates and then to obtain similar properties for BST films on flexible substrates, by optimizing the post deposition annealing process. Part of the work presented in this section has been submitted for publication in Journal of alloys and compounds and another part has been published as an article in Applied Surface Science 336 (2015) 138–142.

3.2.2 Effect of the annealing atmosphere

BST films were grown at room temperature and then were subjected to a post-annealing process, following the PLD conditions shown in Table 3.4. Based on published reports, for the first step, we selected to perform the annealing process at 300°C in Ar atmosphere and vacuum for different times: (Argon - 5h, 10h and 16h; vacuum – 16h) (108).

Figure 3.5 shows the XRD patterns for a BST film which was deposited at room temperature and then post-annealed in Ar atmosphere at 300°C for 16 h. The as-grown BST film exhibits amorphous structure (cf. lower panel of Fig. 3.5) while following post-annealing the same film becomes crystalline with randomly oriented grains (cf. upper panel of Fig. 3.5). It is noted that a polycrystalline structure was observed for all post-annealed BST films. Thus, the annealing process enhances the crystallinity of the films but does not result in preferred orientation.

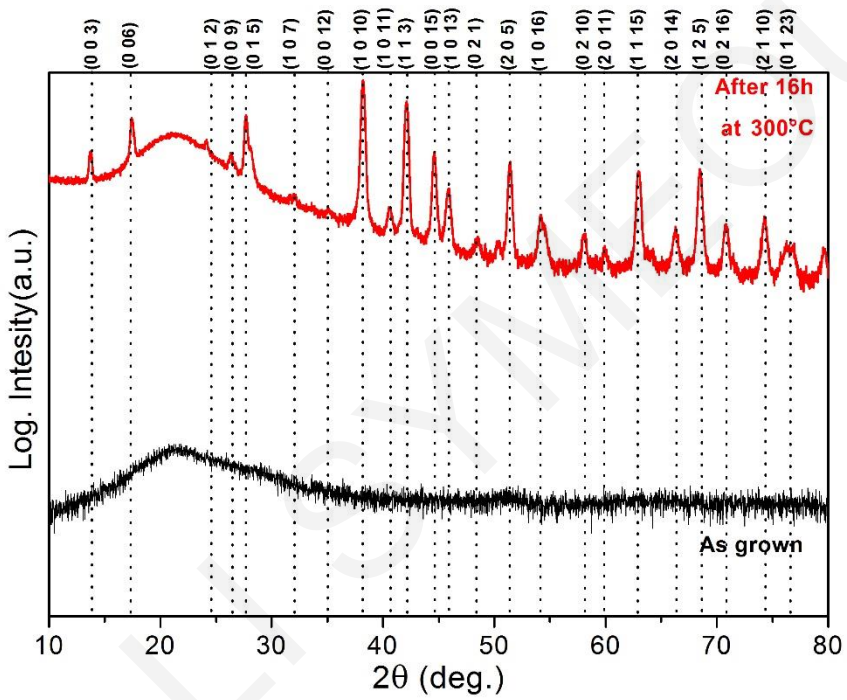

Figure 3.5. X-ray diffraction pattern obtained for a BST film deposited at room temperature and then post-annealed in Ar atmosphere at 300°C for 16 h.

SEM images shown in Figure 3.6 reveal that annealing in Ar atmosphere results in the formation of particles (i.e., film surface becomes rougher) and their areal density increases with increasing annealing duration. On the other hand, films annealed in vacuum have significantly less and smaller in size particles on their surface (Figure 3.9) than the ones annealed in Ar atmosphere. The particles for both types of annealing were found to have the same composition as the bulk of the film. A similar effect has also been reported by Bourgault et al. (108) .

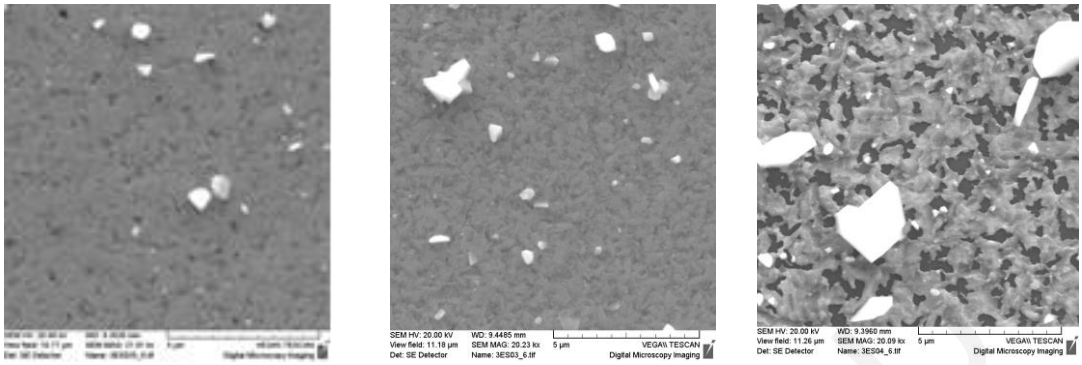

Figure 3.6. SEM image for a BST film, annealed in argon atmosphere for 5(left), 10 and 20h (right).

The results of the composition analysis for the BST films, deposited at room temperature and then post-annealed in Ar atmosphere and vacuum, are illustrated in Table 3.5. The as-deposited films seem to be rich in Bi with the exception of the film that was post-annealed in vacuum. Following the post-annealing treatment, all films display an increase in Bi concentration, which is attributed to the loss of the highly volatile Te during the annealing process.

We expect, therefore, all post-annealed films to exhibit p-type conduction as acceptor-like Bi_{Te} antisite defects are likely to be formed due to excess of Bi ions (108), (109). In addition, we expect the resistivity of the films to decrease with increasing annealing duration because the concentration of the Bi_{Te} antisite defects is likely to increase resulting in an increase of the hole carrier concentration.

	Bi (at%)	Sb (at%)	Te (at%)	Carrier concentration @300K (cm^{-3})
Target composition	10.73	28.82	60.23	-
As deposited	11.19	28.56	60.25	-
5h annealing in Ar	11.89	28.80	59.30	$2.36x10^{19}$
As deposited	11.57	28.47	59.96	-
10h annealing in Ar	12.08	28.68	59.24	$1.93x10^{19}$
As deposited	10.39	28.71	60.90	-
16h annealing in Ar	10.64	29.62	59.74	$4.05x10^{19}$
As deposited	8.92	29.60	61.48	-
16h annealing in vacuum	9.71	29.09	61.20	-

Table 3.5. EDX composition analysis for as-grown BST films, deposited at room temperature, and following annealing under Ar environment or vacuum. Room-temperature carrier concentrations for films annealed under Ar environment.

As can be seen in Figure 3.7, the thermoelectric properties of the films are strongly influenced by the post-annealing treatment. Figure 3.7a displays the temperature dependence of the Seebeck coefficient for BST films annealed at 300°C for different duration times of 5, 10 and 16h. Interestingly while the magnitude of the Seebeck coefficient remains almost the same (~210- 220μV/K at 300K) for all films annealed in Ar atmosphere there is a definite trend in the S magnitude which is consistent with the trend of the hole carrier concentrations (cf. last column of Table 3.6); i.e., S(10h)>S(5H)>S(16h) whereas p(10)<p(5h)<p(16h). This indicates that the S value is strongly dependent on the concentration of the antisite defects and the stoichiometry of the films. On the other hand, the resistivity, which shows metallic behavior in agreement with (108), exhibits a different trend, i.e., ρ(5h)>ρ(10h)>ρ(16h) (Fig. 3.7b). This effect may be attributed to the fact that the grain size increases with increasing annealing duration, i.e., the density of the grain boundaries decreases, and thus, the hole carrier mobility is enhanced (75). The resistivity being affected by both parameters, carrier concentration and carrier mobility, tends to then have the observed trend.

In comparison with the films post-annealed in Ar, the Seebeck coefficient of the film post annealed in vacuum decreases to slightly lower values (190 μV/K at 300K) and its resistivity

drops significantly about a factor of 2. As a result the BST film, which was annealed in vacuum, exhibits the best PF among all the films discussed herein and is equal to 2780μW/mK2 at 300K and 3200μW/mK^2 at 390K (figure 3.7c). These PF values are among the highest ones reported for BST films grown on fused silica substrates. The origin of the PF enhancement in the BST film post-annealed in vacuum is most likely related to the fact that the composition of the film is very close to stoichiometric one (cf. Table 3.5)

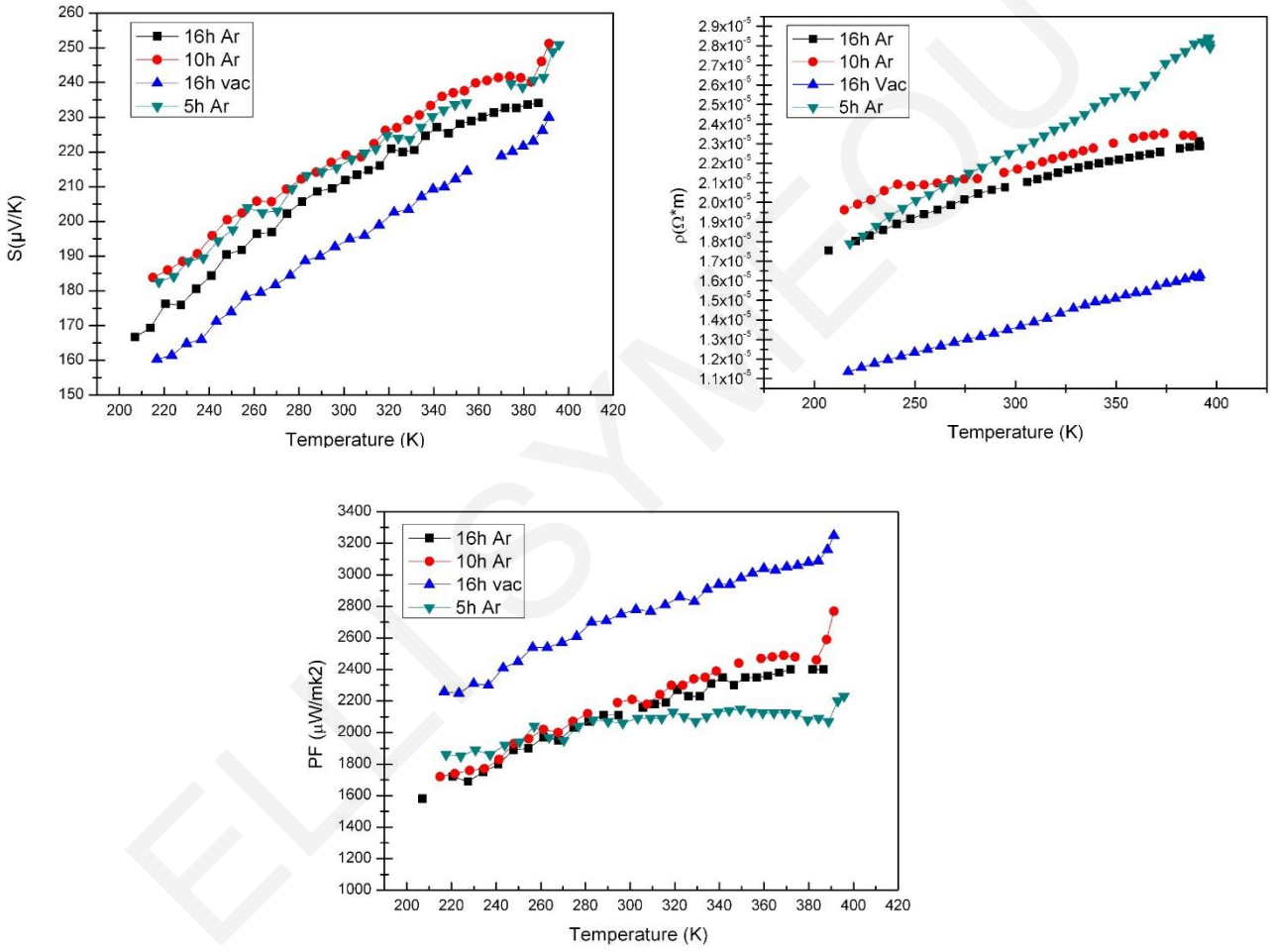

Figure 3.7. Temperature dependence of electrical and thermoelectric properties of BST films grown at room temperature and post-annealed for various times at 300°C: (a) Seebeck coefficient, (b) electrical resistivity, and (c) power factor.

3.2.3 Effect of temperature and time of annealing

Following the observation that the film annealed in vacuum for 16h exhibited the highest PF we proceeded to grow BST films at RT (following the PLD conditions shown in Table 3.4) which then underwent an ex-situ post-deposition annealing treatment at different temperatures (300°C, 350°C) and times (1h, 5h, 10h, 16h) in vacuum.

As shown in Figure 3.8, all investigated BST films seem to exhibit a slight deficiency in Te concentration. This is likely attributed to the evaporation of volatile Te during annealing. Taking into account that there is an overlap between the peaks of Sb and Te in EDX spectra (107) and that the relative error is ~5%, we consider the BST films as being nearly stoichiometric.

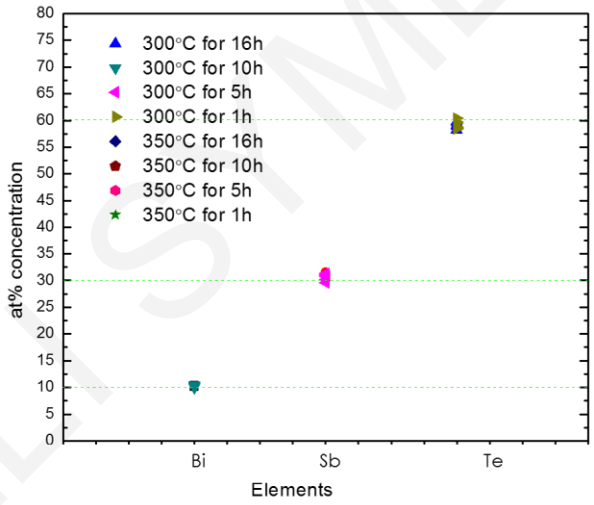

Figure 3.8. EDX composition analysis for the BST films annealed in vacuum, at 300°C and 350°C for different times.

SEM images of BST samples before and after annealing, at different temperatures for 16h, are shown in Figure 3.9. It is evident that the surface morphology of the films is remarkably changed following the post-annealing treatment at different temperatures. In addition, no grain microstructure is visible for the as-deposited BST film within the resolution of our instrument (Fig. 3.9a). However, following annealing at 300°C for 16h (Fig. 3.9b), crystallites are generated

and, as expected, following annealing at 350°C for 16h the size of the crystallites increases even further (Fig. 3.9c).

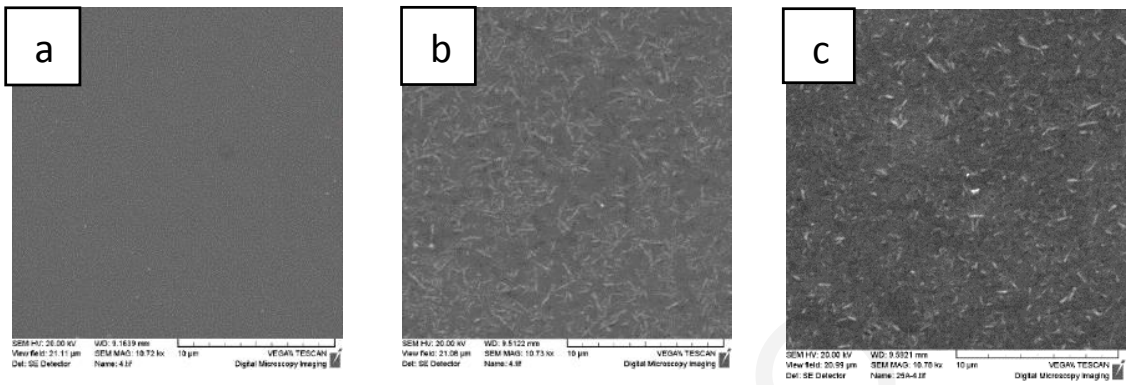

Figure 3.9. SEM images, for the as deposited BST film (a) and for BST films after annealing for 16h (b) at 300°C (c) and 350°C.

Figure 3.10 shows the XRD patterns for a series of BST films which were deposited at RT and then post-annealed in vacuum at different temperatures and times. All the diffraction peaks are indexed to rhombohedral BST (space group R3m; representation in hexagonal unit cell). The as-grown films exhibit very low degree of crystallinity while following post-annealing the same films become crystalline in agreement with the SEM results. The difference in the XRD patterns indicates that the annealing treatment results in a significant grain growth (74). Moreover, for the annealed BST films, the XRD patterns indicate that the film grains exhibit moderate texture with the preferred orientation direction varying depending on the temperature and time of the annealing process. For example, for BST films annealed at 300°C, the preferred orientation is (1 0 10). On the other hand, for BST films annealed at 350°C for more than 5 hours, the intensity of (0 0 6), (0 0 15) and (0 0 18) peaks increases considerably and the prefer orientation is (0 0 6).

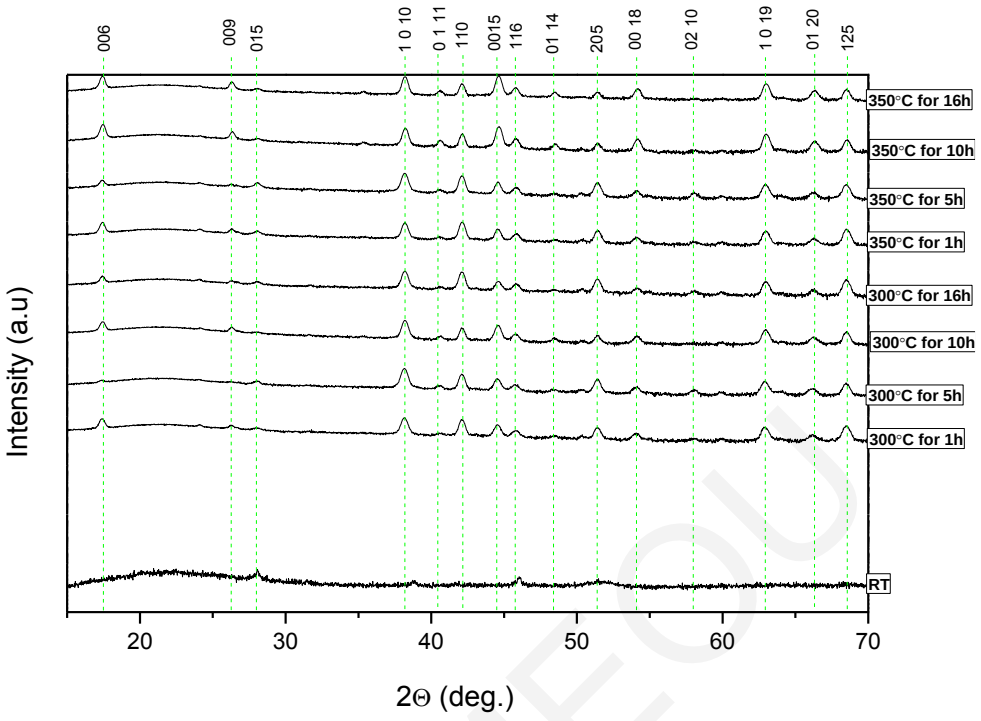

Figure 3.10. X-ray diffraction patterns obtained for a BST film deposited at RT and then post-annealed in vacuum at 300°C and 350°C for different times.

Figure 3.11d shows the carrier concentration and mobility at 300K for the annealed BST films. All films have positive carrier concentrations indicating that they are p-type semiconductors. The hole concentration of films annealed at 300°C increases as annealing duration increases from 1h to 5h, however, longer annealing duration results in a decrease of the hole concentration. On the other hand, the BST films annealed at 350°C for 5h exhibit even higher hole concentration than those films annealed at 300°C but longer annealing duration causes a decrease. Next, we provide possible explanations for both the increase and decrease of the hole concentration as a function of annealing duration. The increase in the hole concentration with annealing duration is attributed to the fact that the BST films have slight deficiency in Te concentration. As a consequence of Te loss, Te vacancies are created and the formation of anti-site defects occurs, where Bi and/or Sb atoms occupy Te sites in the lattice. These Bi_{Te} and Sb_{Te} antisite defects act as electron acceptors. On the other hand, the decrease in the hole concentration, following several hours of annealing at temperatures 300°C and above, is attributed to the loss of Bi and the consequent creation of Te_{Bi} antisite defects which act as

electron donors. Noro et al. (110) have explained the creation of Te_{Bi} antisite defects on the basis of the relative vapor pressures of the different elements and compounds which are formed.

Next, we discuss the evolution of room temperature hole mobility as a function of annealing process parameters. It is evident from Figure 3.11d, that the hole mobility increases with increasing annealing temperature and duration. This observation is attributed to the enhancement of grain growth (i.e., reduction of grain boundaries), (83) improvement of crystallinity and increased preferred grain orientation with increasing annealing temperature and duration. The highest mobility value ($141 cm^2/V*s$) is observed for BST films annealed at 350°C for 16h.

Figure 3.11 presents the thermoelectric properties of the annealed BST films. It is noted that no data are presented for as-grown films grown at RT because it was not possible to measure them due to very high resistivity. Specifically, as XRD and SEM results (vide supra) indicate the as-grown films have very low degree of crystallinity and the grains are very small (in the scale of nanometers). Consequently, there are many grain boundaries and the resistivity becomes very high. (74). A linear variation of the Seebeck coefficient and electrical resistivity with temperature (250-390K) is observed for all annealed BST films, as can be seen in figure 3.11a. This variation is characteristic of degenerate semiconductors. According to semiconductor theory, Seebeck coefficient is directly proportional to the scattering factor and inversely proportional to the logarithmic carrier concentration (111). The enhancement of Seebeck coefficient observed at high temperatures may be caused by the dominant effect of carrier scattering at point defects and grain boundaries resulting from the annealing treatment and anti-site defects. The measured values of Seebeck coefficient range from 130-260 μV/K with the

higher values belonging to the films with the lower hole concentration and vice versa. Looking at the temperature dependence of the resistivity figure 3.11b, one ascertains that the BST films that were annealed at 350°C for 10h and 16h have the lowest value. This is attributed to the higher mobility and increased (006) preferred orientation of the films. The resistivity of the annealed BST films range from $8x10^{-6}$ Ohm.m to $2.4x10^{-5}$ Ohm.m. Figure 3.11c, displays the temperature dependence of the calculated PF values for all annealed BST films. It is evident that with increasing annealing temperature and duration the PF increases. Specifically, PF (350°C/16h) > PF (350°C/10h) > PF (300°C/16h) > PF (300°C/10h) > PF (350°C/5h) > PF (350°C/1h) > PF (300°C/5h) > PF (300°C/1h). The BST film annealed at 350°C for 16h has a Seebeck coefficient of 210μV/K, an electrical resistivity of $1.15x10^{-5}$ Ohm.m and exhibits the highest PF value of 3750μW/mK^2 at 380K. This value is the highest one, ever reported in the case of BST films on fused silica substrates. It is pointed out that annealing at even higher temperatures (>350°C) not only does not improve the thermoelectric properties of BST films but it has a detrimental effect on them as it results in a re-evaporation of BST films from the substrate.

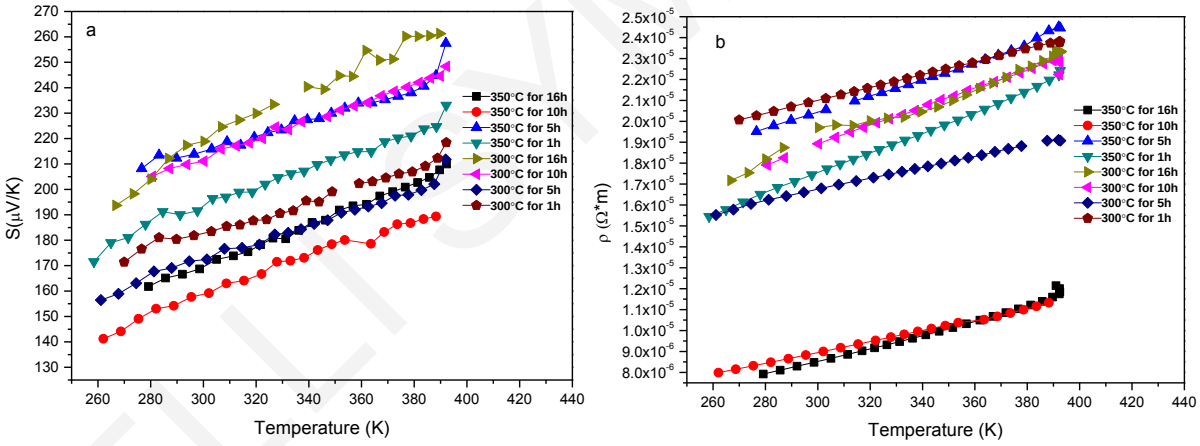

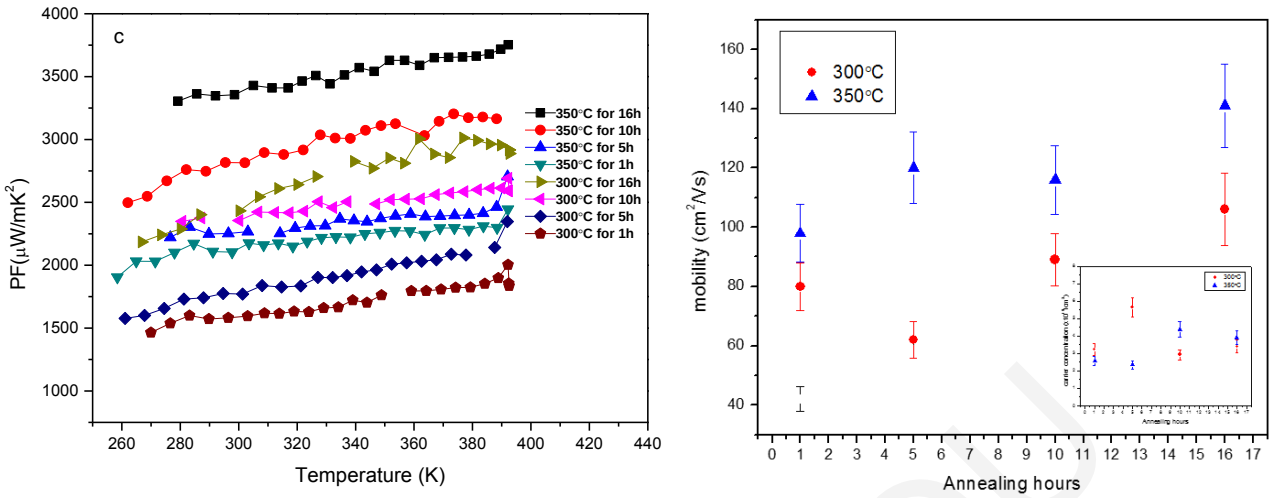

Figure 3.11. Temperature dependence of electrical and thermoelectric properties of BST films grown on fused silica substrates at room temperature and then annealed at 300°C and 350°C for different times(a) Seebeck coefficient, (b) electrical resistivity, (c) power factor, (d) mobility and carrier concentration (at 300K).

3.2.4 Effect of the deposition temperature on the thermoelectric properties of $Bi_{0.5}Sb_{1.5}Te_3$ films following by post annealing

In this study, we have chosen to grow BST films both at 350°C, due to the high PF value that was discussed in section 3.1.5, and at room temperature in order to determine whether the deposition temperature affects the thermoelectric properties of BST films, followed by post annealing. Figure 3.12 displays the thermoelectric properties of this comparison. As can be seen in Figure 3.12a, the Seebeck coefficient of the BST film grown at room temperature and then subjected to a post annealing treatment at 350°C for 16h is higher than that of the BST film grown at 350°C. The resistivity follows the same trend (Table 3.6). This behavior is well explained by the variation of the carrier concentration which is inversely proportional to the Seebeck coefficient and resistivity. Also the composition of the BST film grown at 350 °C is not the optimum one. The hole carrier concentration increases with decreasing Te concentration, as happened with the film grown at 350°C. This dependence of the carrier concentration on the

composition can be interpreted considering the recombination of the majority charge carrier, in this case, hole, with the minority one, electron, which was more pronounced for Te-deficient samples (80). As a consequence, the highest PF is observed in the BST films grown at RT and then subjected to a post annealing treatment.

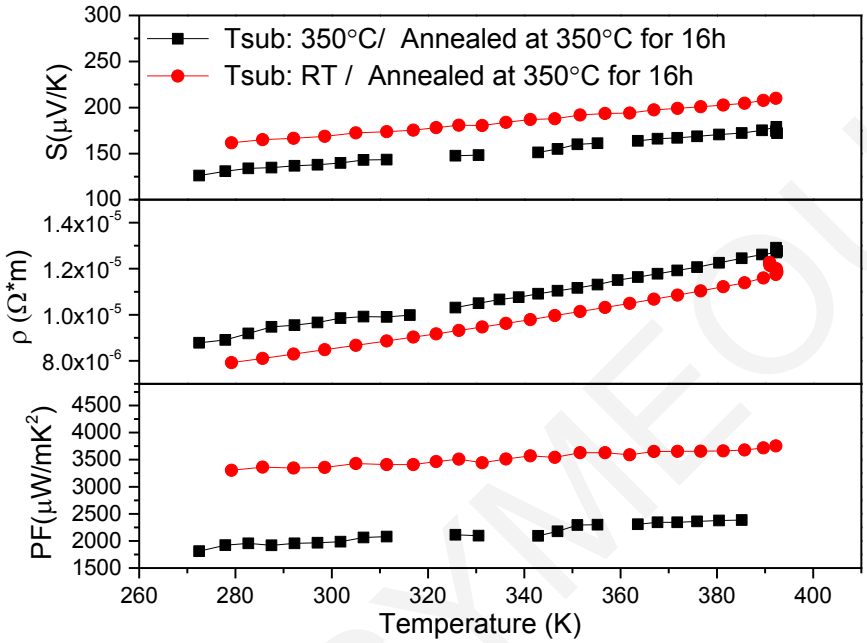

Figure 3.12. Temperature dependence of electrical and thermoelectric properties of BST films grown at room temperature and 350°C, following by annealing annealed at 350°C for 16h (a) Seebeck coefficient, (b) electrical resistivity, and (c) power factor.

	Bi (at%)	**Sb (at%)**	**Te (at%)**	**Carrier concentration @300K (cm^{-3})**
Tsub: 350 °C Annealed at 350C for 16h	8.96	33.79	57.25	$8.26x10^{19}$
Tsub: RT Annealed at 350C for 16h	9.93	31.21	58.86	$3.91x10^{19}$

Table 3.6. EDX composition analysis for BST thin films grown at room temperature and 350°C, following by annealing annealed at 250°C for 16h, along with their carrier concentration.

3.2.5 Conclusions

BST thin films have been grown by PLD on fused silica substrates in an attempt to achieve bulk-like PF values. We have investigated the effect of the three major annealing parameters: atmosphere, temperature and time, on the microstructure, chemical composition and thermoelectric properties of films grown at room temperature. We have identified the annealing process parameters that result in bulk-like PF values for BST films grown on fused silica substrates. It was evident that with increasing annealing temperature and duration the PF increases. The hole mobility increases with increasing annealing temperature and duration. This observation is attributed to the enhancement of grain growth improvement of crystallinity and increased preferred grain orientation with increasing annealing temperature and duration. Specifically, the PF follows this sequence: PF (350°C/16h) > PF (350°C/10h) > PF (300°C/16h) > PF (300°C/10h) > PF (350°C/5h) > PF (350°C/1h) > PF (300°C/5h) > PF (300°C/1h). The BST film annealed at 350°C for 16h in vacuum, has a carrier concentration of $4x10^{19}cm^{-3}$, a Seebeck coefficient of 210μV/K, an electrical resistivity of $1.15x10^{-5}$ Ohm.m and exhibits the highest PF value of $3750\mu W/mK^2$ at 380K. This is the highest PF value for BST films grown on amorphous substrates to date and compares very well with the highest bulk value ($3770\mu W/mK^2$).

3.3 Effect of substrate

3.3.1 Motivation

The second part of this work concerns the attempt to obtain BST films with bulk-like thermoelectric properties onto a flexible substrate such as Kapton, exploiting the experience we accumulated from the BST films grown on fused silica substrates (as discussed above). Kapton was chosen as substrate because it is amorphous and has low thermal conductivity, similarly to fused silica, and because of its relatively good heat resisting properties for a polymeric material. The influence of both substrate temperature and annealing process parameters on the thermoelectric properties of the BST films were investigated.

3.3.2 Effect of substrate temperature (kapton substrate)

Prior to deposition the substrates underwent cleaning; specifically, kapton substrates were cleaned thoroughly in an ultrasonic bath with acetone and ethanol. The PLD conditions remain the same as seem in table 3.4. Figure 3.13 shows the XRD patterns of BST thin films deposited on Kapton at different substrate temperatures (100°C - 300°C). It is evident that the films grown at substrate temperatures lower than 200°C are amorphous (will not be discussed any further herein) whereas films grown at temperatures higher than 200°C exhibit enhanced crystallinity and (1 0 10) preferred orientation. Also, for the film grown at 250°C the intensity of the diffraction peak assigned to (006) plane is enhanced.

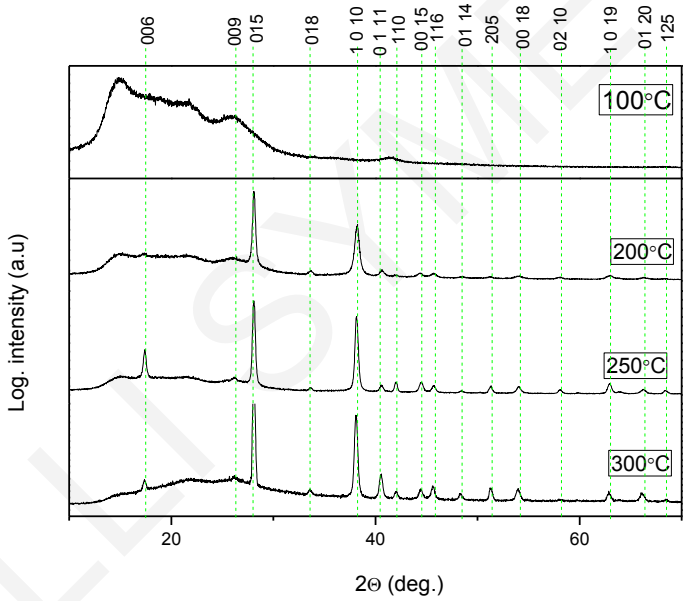

Figure. 3.13. X-ray diffraction patterns for BST films grown on kapton substrates at different substrate temperatures.

The results of EDX elemental analysis for all BST films grown on Kapton along with their Hall-measured carrier concentrations are presented in Table 3.7. All films are characterized by a small deficiency in Te and an increasing Bi concentration as the substrate temperature increases. In addition, the carrier concentration of the films increases from 5.4×10^{19} cm^{-3} to 1.42×10^{20} cm^{-3} as the substrate temperature increases from 200°C to 300°C. It is speculated that as the Bi

concentration increases and the Te concentration decreases with increasing substrate temperature, the concentration of Bi_{Te} antisite defects increases with a corresponding increase in the carrier concentration.

Samples	Bi (at %)	Sb (at %)	Te (at %)	Carrier concentration (cm^{-3})
200°C	10.18	30.94	58.87	$5.7x10^{19}$
250°C	10.47	31.13	58.39	$1.23\ x10^{20}$
300°C	10.99	31.07	57.94	$1.42\ x10^{20}$

Table 3.7. EDX composition analysis for BST thin films grown on Kapton at different temperatures along with their carrier concentration.

Temperature dependence of Seebeck coefficient, electrical conductivity and power factor for the BST films grown on Kapton at different substrate temperatures are plotted in Figure 3.14. The Seebeck coefficient of the films (Figure 3.14a) decreases with increasing substrate temperature as a consequence of the increasing carrier concentration. The BST film grown at 200°C exhibits semiconducting-like behavior whereas the films grown at higher temperatures exhibit metallic-like behavior (Figure 3.14b). Both the transition from semiconducting to metallic behavior with increasing substrate temperature as well as the large difference in the resistivity of the samples exhibiting metallic behavior are attributed to the combined effect of the increasing carrier concentration and increasing hole mobility. The latter effect is attributed to the enhanced crystallinity and texturing of the BST films with increasing substrate temperature.

The BST film deposited at 250°C exhibits the best PF, which is $2600\mu W/mK^2$ at 390K (Figure 3.14c). This result is attributed to the enhanced (006) diffraction peak intensity (Figure 3.13), which indicates that there are several grains/crystallites with their layered structure aligned parallel with the surface of the substrate, and the consequent strong reduction in electrical resistivity (it is reminded that BST is a layered anisotropic material with $\rho_{in\ plane} < \rho_{cross\ plane}$). For substrate temperatures above 250°C, the PF decreases dramatically because of Kapton substrate

degradation and poor adhesion of BST films. This observation is in accordance with previous findings (112).

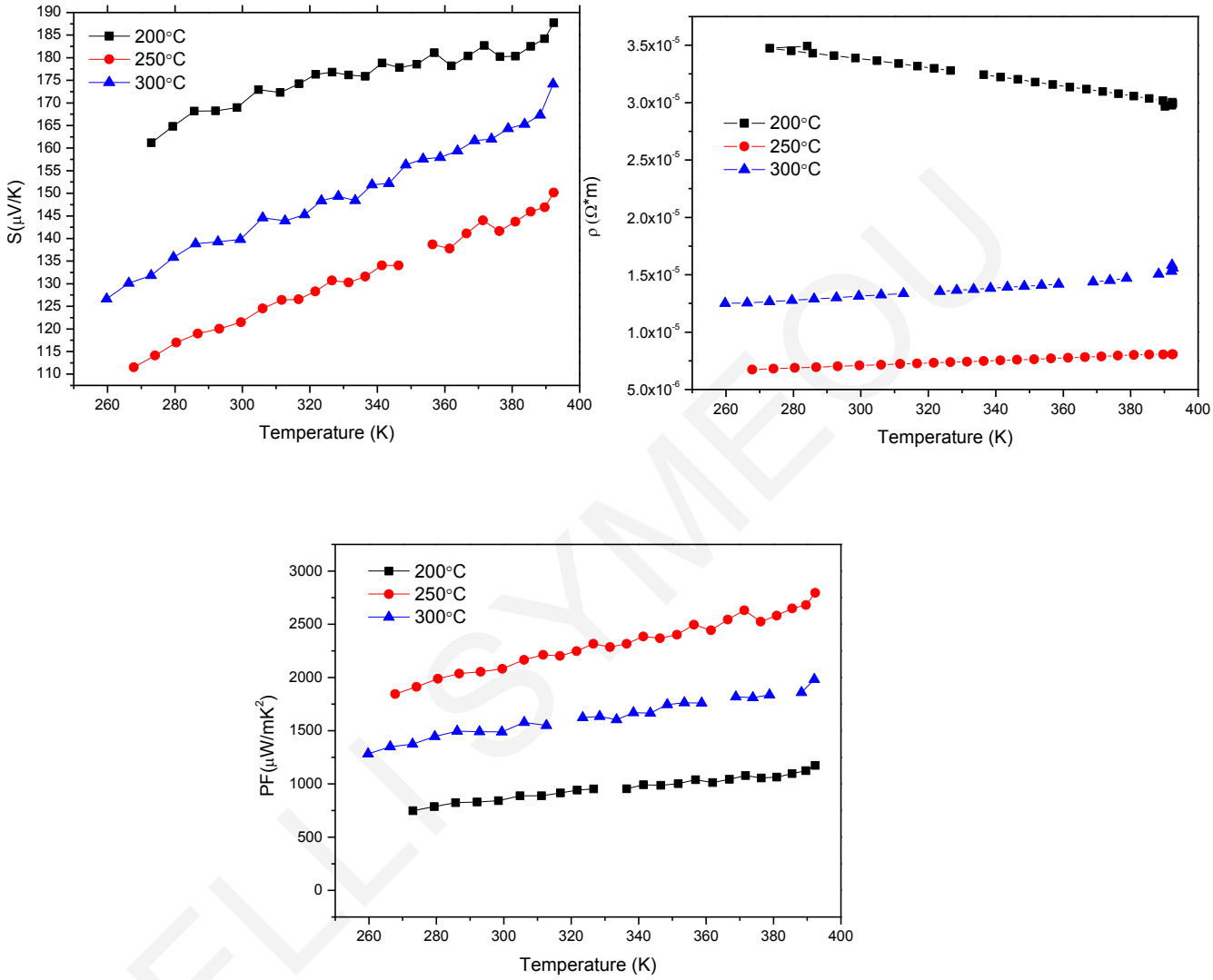

Figure 3.14. Temperature dependence of electrical and thermoelectric properties of BST films grown on Kapton substrates at different substrate temperatures (a) Seebeck coefficient, (b) electrical resistivity, and (c) power factor.

3.3.3 Effect of post annealing (Kapton substrate)

Next, we discuss the results obtained for BST films grown on Kapton substrates at RT and then post annealed at 250°C for 1h and 5 h. The reason we restricted our investigation to the particular annealing parameters is that BST films annealed at temperatures over 250°C exhibit microcracks and poor adhesion to Kapton. This effect is attributed to the large change in the thermal expansion coefficient of Kapton with increasing temperature. For example, the thermal expansion coefficient of Kapton is 17 $x10^{-6}$/K at 30°C and 44 $x10^{-6}$/K at 400°C (113). Also, for the temperature range of interest, the coefficient of BST is ~15 - 20$x10^{-6}$/K depending on the crystallographic direction (114).We suggest that this thermal expansion mismatch generates cracks in the films due to the large tensile thermal strains induced upon cooling down to RT following the annealing of the BST films.

The XRD patterns shown in figure 3.15 reveal that the amorphous as-grown films undergo crystallization when they are subjected to annealing treatment (similarly to the case of fused silica substrates). In particular, the film annealed for 5h has an enhanced (006) reflection indicative of crystallization with a preferred orientation along the c-axis.

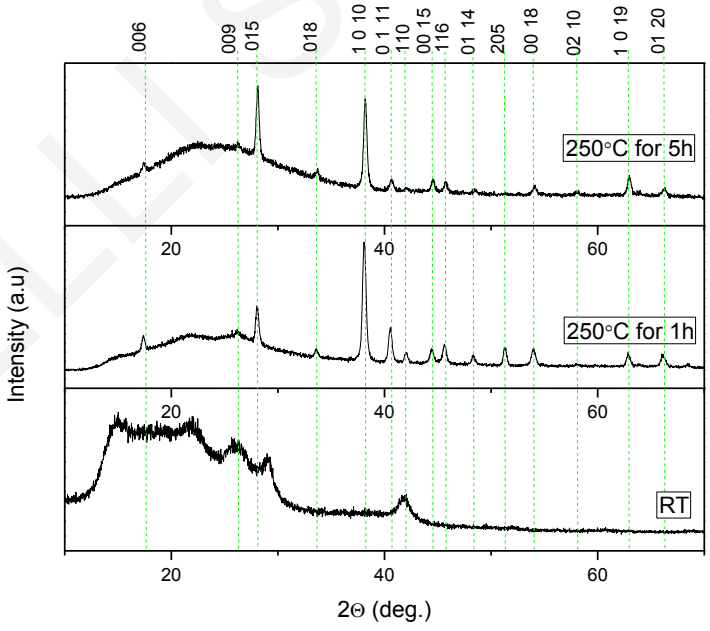

Figure 3.15. X-ray diffraction patterns obtained for BST films deposited at RT on kapton substrates and then post-annealed in vacuum at 250°C for 1h and 5h.

The thermoelectric properties of the annealed BST films are presented in Figure 3.16. A linear variation of the Seebeck coefficient with temperature is observed for all investigated films (Figure 3.16a). The Seebeck coefficient of the films decreases as the annealing time duration and the carrier concentration increases (Table 3.8). In addition, it is evident that the resistivity exhibits a linear variation with temperature (Figure 3.16b) and decreases with increasing annealing time duration. Similarly to the case of fused silica substrates, the decrease of the resistivity of BST films grown on Kapton substrates is attributed to the enhancement of crystallinity and preferred (006) orientation with increasing annealing time duration. Figure 3.16c displays the temperature dependence of the calculated PF values. The BST film grown at RT and annealed at 250°C for 5h exhibits the highest PF value of 2600μW/mK^2 at 390K, which is the same as the one found for the case of BST films grown on Kapton substrates heated at 250°C. Although this PF value is lower than the bulk value, it is nevertheless the highest ever reported for BST films on flexible substrates.

Samples	Bi (at %)	Sb (at %)	Te (at %)	Carrier concentration (cm^{-3})
RT	10	29.73	60.27	-
250°C for 1h	9.99	30.34	59.66	3.34 x10^{19}
RT	10.27	29.32	60.4	-
250°C for 5h	10.07	31.81	58.15	5.35x10^{19}

Table 3.8. EDX composition analysis for BST thin films grown on Kapton at RT and followed by post annealing at 250°C along with their carrier concentration (when possible to measure).

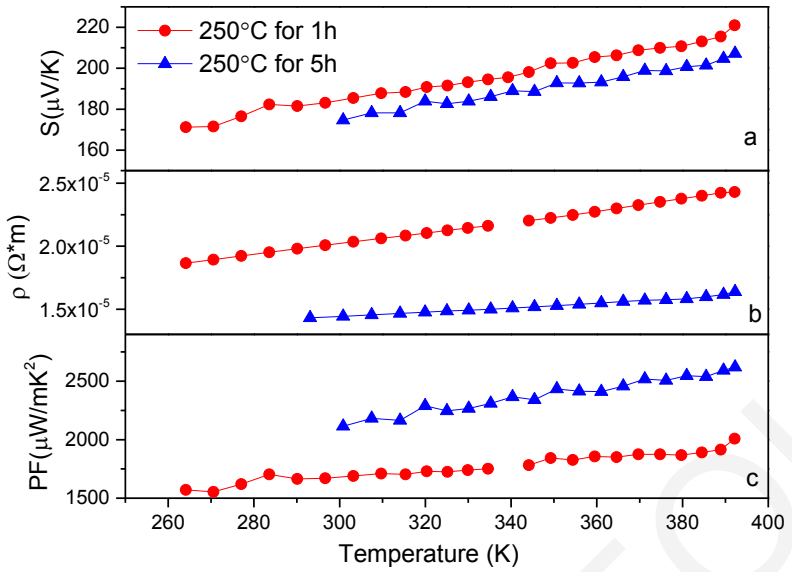

Figure 3.16. Temperature dependence of electrical and thermoelectric properties of BST films grown on kapton substrates and annealed at 250°C (a) Seebeck coefficient, (b) electrical resistivity, and (c) power factor.

3.3.4 Conclusions

We have investigated the effect of substrate temperature on the growth of BST films on Kapton substrates. All films are characterized by a small deficiency in Te and an increasing Bi concentration as the substrate temperature increases. As a consequence the carrier concentration of the films increases from $5.7x10^{19}$ to $1.42x10^{20}$ cm^{-3}. The films grown at substrate temperatures lower than 200°C are amorphous and as the temperature increase the crystallinity of the films increases and preferred orientation observed.

In addition, we have investigated the effect of post annealing treatment in vacuum on the chemical composition and thermoelectric properties of films grown at room temperature on Kapton substrates. The BST films annealed at temperatures over 250°C exhibit microcracks and poor adhesion to Kapton. The BST film grown at RT and annealed at 250°C for 5h exhibits the highest PF value of 2600μW/mK^2 at 390K, which is the same as the one found for the case of BST films grown on Kapton substrates heated at 250°C. This result is attributed to the enhanced (006) diffraction peak intensity. Although this PF value is still lower than the bulk value, it is the highest one ever reported for BST films grown on flexible substrates.

3.4 Effect of Bi/Sb and Bi/Te ratio on the thermoelectric properties of $Bi_xSb_{2-x}Te_3$ films

3.4.1 Motivation

The motivation behind the present study is to understand the transport properties of BST thin films with different Bi/Te and Bi/Sb ratios in the temperature range of 250-390K. Such study is accomplished on as-deposited and annealed thin films in order to understand the stoichiometry transfer from target to film and how the stoichiometry affects the transport properties of the films. Te vaporization loss occurs during the melting and annealing process and this leads to the deviation from the stoichiometry, as we have already discussed in Section 3.2. The aims of this study were: first, to control the loss of Te in order to achieve films with 60 at % of Te by changing the Bi/Te radio and, second, to study the effect of Bi/Sb ratio on the thermoelectric properties of the BST films.

Several techniques and composition combinations of BST compounds have been employed to optimize the thermoelectric properties. The highest PF values reported using PLD are shown below. L. Bassi et al. (115) have reported PF of 2500 $\mu W/mK^2$ at room temperature for a textured film grown on Si substrate. In 2009, Obara et al. (116) reported the influence of Bi content on the microstructures and thermoelectric properties of $Bi_{2-x}Sb_xTe_3$ thin films and found that the film with composition $Bi_{0.3}Sb_{1.7}Te_3$ has the highest PF of 3700 $\mu W/mK^2$ at RT. In 2014, Cornett et. al. (117) reported that some of the $Bi_{2-x}Sb_xTe_3$ films grown on Si substrates and annealed in Te vapor showed PF values comparable to the bulk value. But it is not clear yet, why some films exhibited these high PF values and some films did not.

The BST films were grown at RT (using the PLD conditions shown in Table 3.4) on fused silica substrates and then underwent an ex-situ post-deposition annealing treatment at 300°C for 16h in vacuum.

3.4.2 Effect of Bi/Te ratio on the $Bi_xSb_{2-x}Te_3$ films

Christen et al. (104) reported that it is possible to work in a regime of significant excess of the volatile component, all of which re-evaporates beyond the amount needed to form the stoichiometric compound. Thus, BST targets were prepared by cold press, as we described above, according to the formula $Bi_{10-x}Sb_{30}Te_{60+x}$ (x=2-6). Table 3.9, shows the composition analysis of the targets (CP), of the films after annealing treatment (AA) and the nominal stoichiometry of the mixed powders (NC). As can be seen, the targets have more than 1at% deficiency in Te. In general, as x increases the deficiency in Te increases. This phenomenon is attributed to the incomplete mixing of the constituent elements and the subsequent formation of more than one phases; this is confirmed by the SEM analysis (not shown) which showed that the targets had a second phase of Te. Despite this fact, we proceeded to ablate these targets and deposit BST films thinking that the second phase of Te may assist in achieving the correct Te content in the films.

As can be seen in Table 3.9, the films after annealing treatment exhibit a considerable change in the elemental concentration. All films display an increase in Bi and Sb concentration and did not follow the excess of x that was added in the targets but instead have the opposite trend (very high deficiency in Te). As a consequence of Te loss, Te vacancies are created and we expect the formation of antisite defects, where Bi or/and Sb occupy Te positions in the lattice. Also, Table 3.9 presents the hole carrier concentration and hole mobility at 300K. As I mentioned before, all BST films have a deficiency in Te, which is responsible for the creation of antisite defects and the modification of carrier concentration. Film 1 exhibits a carrier concentration of $1.84x10^{19}cm^{-3}$ close to the one found in the best bulk materials. Except for film 2, the hole carrier concentration increases with decreasing Te concentration. The most interesting films appear to be film 1 and film 4. Both exhibit the highest mobility, which is attributed to the increased preferred orientation along (00l), as can be seen in the XRD patterns below.

Sample Name		Bi (at%)	Sb (at%)	Te (at%)	Carrier concentration (cm^{-3})	Mobility (cm^2/Vs)
1	NC	8	30	62		
$\mathbf{Bi_{9.03}Sb_{31.37}Te_{59.59}}$	CP	7.57	31.41	61.01		
	AA	9.03	31.37	59.59	1.84×10^{19}	144
2	NC	7.5	30	62.5		
$\mathbf{Bi_{8.62}Sb_{34.79}Te_{56.58}}$	CP	7.06	30.74	62.19		
	AA	8.45	32.57	58.98	1.86×10^{19}	95.2
3	NC	7	30	63		
$\mathbf{Bi_{8.45}Sb_{32.57}Te_{58.98}}$	CP	6.51	31.82	61.67		
	AA	8.62	34.79	56.58	3.34×10^{19}	68.3
4	NC	6	30	64		
$\mathbf{Bi_{7.12}Sb_{33.84}Te_{59.03}}$	CP	5.56	31.76	62.67		
	AA	7.12	33.84	59.03	2.23×10^{19}	133
5	NC	5	30	65		
$\mathbf{Bi_{6.47}Sb_{35.77}Te_{57.75}}$	CP	4.68	31.32	63.99		
	AA	6.47	35.77	57.75	5.72×10^{19}	62.4
6	NC	4	30	66		
$\mathbf{Bi_{4.85}Sb_{37.46}Te_{57.69}}$	CP	3.82	31.3	64.88		
	AA	4.85	37.46	57.69	4.89×10^{19}	85.8

Table. 3.9. EDX composition analysis for BST target and thin films grown at RT and followed by post annealing at 300°C for 16h. (NC refers to: Nominal composition, CP refers to: target with cold press, AA refers to: BST films after annealing).

Figure 3.17 shows the XRD patterns for a typical as-grown BST film, and for the films post-annealed in vacuum. The as-grown BST films exhibit amorphous structure (as we expected) while following post-annealing the same films become crystalline with randomly oriented grains. Films 1 and 4, which are closer to the 10/30/60 composition, show preferred (00l) orientation.

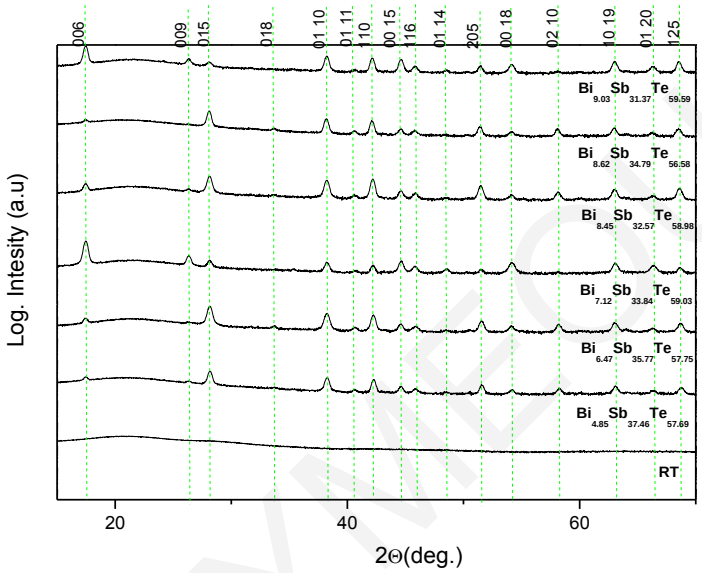

Figure 3.17. XRD patterns for a typical as grown BST film (Bi/Te), and for the films post-annealed in Vacuum.

The Seebeck coefficient and electrical resistivity are closely related to the carrier concentration, which is greatly affected by the formation on anti-site defects. Figure 3.18a presents the Seebeck coefficient as a function of the carrier concentration, which is inversely proportional to it and follows the general behavior. On the other hand, resistivity (Figure 3.18b) does not show a clear behavior as a function of carrier concentration because it is affected also by the mobility.

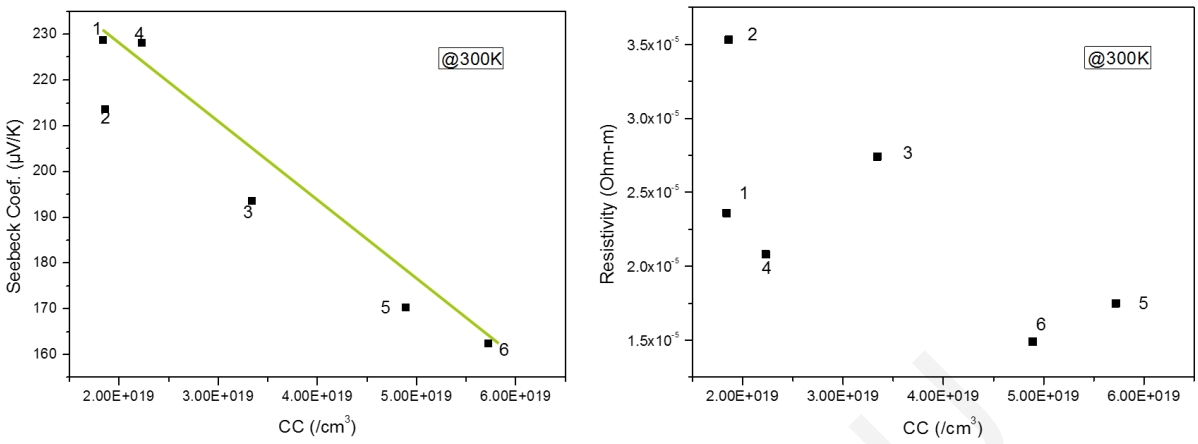

Figure 3.18. a) Seebeck coefficient and b) electrical resistivity as a function of carrier concentration for BST (Bi/Te) films.

Figure 3.19 displays the thermoelectric properties of these films as a function of temperature. The observed increases in Seebeck coefficient (Figure 3.14a) with decreasing carrier concentration is expected, due to be inversely proportional to it, as I mentioned before. Despite the fact that samples 2 and 3 have similar carrier concentration, they have different Seebeck coefficient due to the large differences in the mobility. The highest Seebeck coefficient has been observed for $Bi_{9.03}Sb_{31.37}Te_{59.59}$ film and takes values from 185-250 μv/K. The resistivity being affected by both parameters, carrier concentration and carrier mobility, tends to then have the observed trend (Figure 3.14b). In particular, the resistivity represented by $\rho = (1/ne\mu)$, that is clearly related by the number of the hole and their mobility of them. The resistivity of the films range from $1x10^{-5}$ Ohm.m to $4x10^{-5}$ Ohm.m. Figure 3.14c displays the temperature dependence of the calculated power factor values for all films. $Bi_{7.12}Sb_{33.84}Te_{59.03}$ exhibits the best PF over the entire temperature range investigated; e.g., at 290 K PF= 2600 $\mu W/K^2m$. This film exhibited the highest mobility and the highest Seebeck coefficient among the samples studied in this part of the Thesis. It is remarkable that the PF remains constant for the whole range of temperatures.

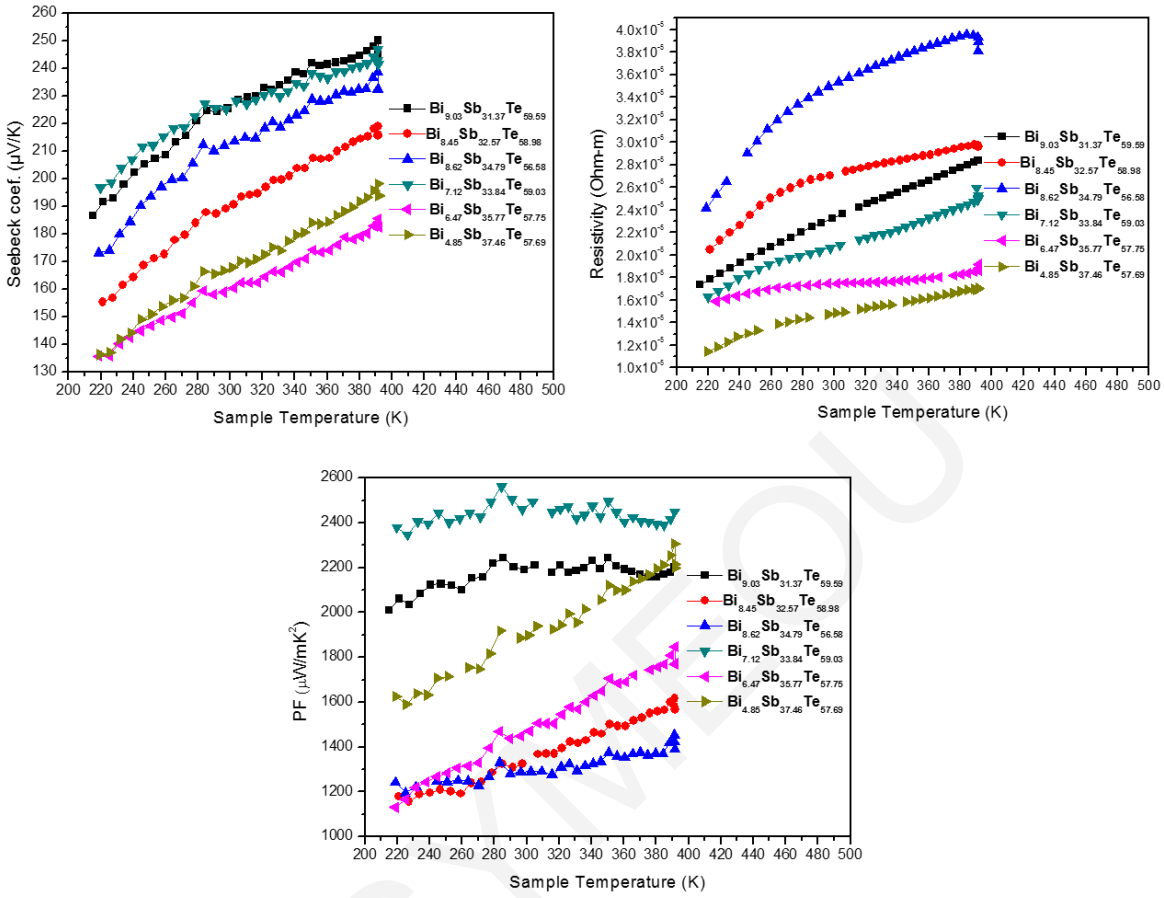

Figure 3.19. Thermoelectric properties of BST (Bi/Te) films as a function of temperature. a) Seebeck coefficient, b) Electrical resistivity, c) power factor.

3.4.3 Effect of Bi/Sb ratio on the $Bi_xSb_{2-x}Te_3$ films

According to the results of Section 3.4.2, which showed that the film with composition 7/34/59 had the highest PF, we decided to ablate a series of p-type $Bi_{10-x}Sb_{30+x}Te_{60+1\%wt}$ (x=0-6) targets prepared by cold press, as we described above, in order to investigate the influence of the Sb content on the thermoelectric properties of BST films, grown at RT and annealed at 300°C for 16h in vacuum. The samples were named BST0.5, BST0.4, BST0.3 and BST0.2 for $Bi_{10}Sb_{30}Te_{60+1\%wt,}$ $Bi_8Sb_{32}Te_{60+1\%wt,,}$ $Bi_6Sb_{34}Te_{60+1\%wt,}$ $Bi_4Sb_{36}Te_{60+1\%wt,}$ respectively.

The XRD patterns are the same as those shown in Figure 3.10, indicating that the films have polycrystalline rhombohedral structure with a preferred (1 0 10) orientation. A very small peak shift is observed with changing the Bi/Sb ratio, because of a change in lattice parameters. Figure 3.20 reveals the morphology of the BST films. Grains can be observed at the surface of all samples. The grain size increases with increasing Sb content x=0-6 and voids appear on the surface.

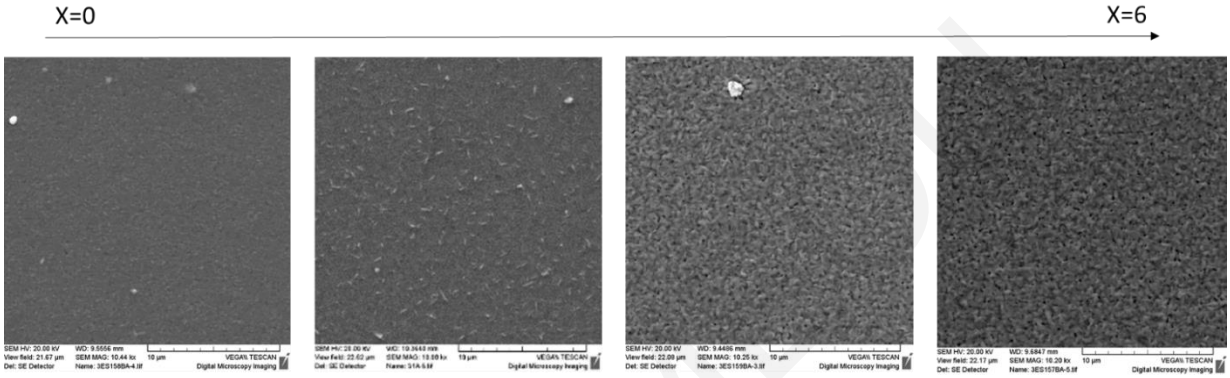

Figure 3.20. SEM images, for BST films with various Sb content.

The composition of the BST samples was investigated by EDX, as shown in Table 3.10. It is evident that the Bi concentration tends to increase after annealing treatment possibly due to the loss of Te. We expect therefore an increase in the carrier concentration. Also, as we discussed above, the extra holes, in p-type BST are created by the antisite defects resulting from the Bi or Sb atoms occupying Te sites. Therefore, the antisite defect concentration of Sb_{Te} increases with decreasing Bi content, resulting in an increase in the hole carrier concentration (67). This expectation is confirmed by the measured room-temperature carrier concentration values shown in Table 3.10. On the other hand, the mobility remains almost constant, expect for the BST03 film which showed a little higher mobility than the other films. The texturing of the BST films, which does not change by adding Sb, is responsible for the constant values of the mobility. However, the mobility of the BST films are very high and is in agreement with previous findings (117) .

	Bi (at %)	Sb (at %)	Te (at %)	Carrier concentration @300K (cm^{-3})	Mobility ($cm^2/V.s$)
Target composition	9.19	31.07	59.7		
BST0.5 at RT	9.93	30.2	59.86		
BST0.5 Annealed	9.76	32.48	57.755	$2.23x10^{19}$	157
Target composition	7.47	33.03	59.48		
BST0.4 at RT	7.93	32.16	59.9		
BST0.4 Annealed	8.04	33.01	58.95	$2.87\ x10^{19}$	158
Target composition	5.62	35.16	59.22		
BST0.3 at RT	6.07	34.29	59.62		
BST0.3 Annealed	6.35	35.18	58.465	$3.71\ x10^{19}$	186
Target composition	3.85	37.28	58.86		
BST0.2 at RT	3.87	36.77	59.35		
BST0.2 Annealed	3.92	36.91	59.17	$3.90\ x10^{19}$	153

Table 3.10. EDX composition analysis for BST target and thin films grown at RT and followed by post annealing at 300°C for 16h, their carrier concentration and their mobility.

The temperature dependence of thermoelectric properties of the BST films with various Sb content is illustrated in Figure 3.21. As can be seen in Figure 3.21a and b, a linear variation of the Seebeck and resistivity with temperature (250-390K) was observed for all studied BST films. The Seebeck coefficient at 390K decreased from 250 to 180μv/K by increasing the Sb content from x=0 to 6. This change is well explained by the variation of the carrier concentration, which is inversely proportional to it. In Figure 3.21b, one can see the resistivity of the BST films. The resistivity of the BST films at 390K decreases from $1.9x10^{-5}$ Ohm.m to $1.3x10^{-5}$ Ohm.m by increasing the Sb content from x=0 to 6. The behavior of ρ(x) is not monotonic as film BST03 exhibits a lower resistivity than film BST02 likely due to lower mobility.

Figure 3.21c reveals the temperature dependence of the calculated PF values for all BST films. The stoichiometry of the BST films obviously affected the PF. We can observe that film BST02 has the lowest PF value even though its resistivity is very low. This is attributed to its very high carrier concentration and, as a consequence, it has a very low Seebeck coefficient. On the other hand, the PF of films BST04 and BST03 is high and increases with increasing temperature. At about 330K the PF values cross, meaning that below 330K the BST03 film has higher PF (3340

$\mu W/mK^2$) than the BST04 film (3160 $\mu W/mK^2$) and after 330K the BST04 has higher PF (3820 $\mu W/mK^2$) than the BST03 film (3620 $\mu W/mK^2$). Concluding, we can say that both compositions ($Bi_8Sb_{32}Te_{60+1\%wt,}$ and $Bi_6Sb_{34}Te_{60+1\%wt}$) have the best thermoelectric properties. The BST04 film due to the highest Seebeck coefficient and the BST03 film due to lowest resistivity among the investigated films.

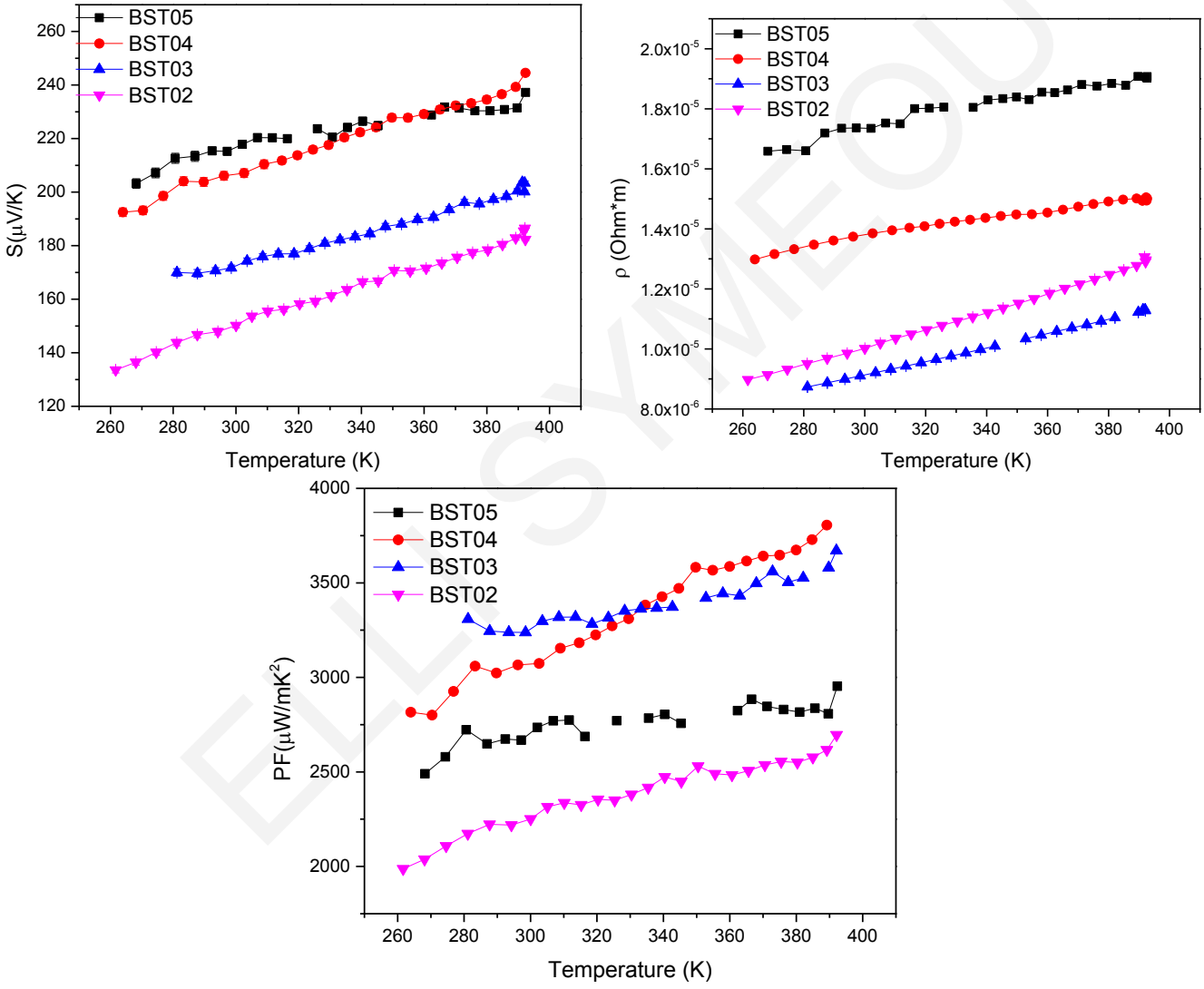

Figure 3.21. Temperature dependence of electrical and thermoelectric properties of BST films with different Sb content (a) Seebeck coefficient, (b) electrical resistivity, and (c) power factor.

3.4.4 Conclusions

BST thin films with different Bi/Te and Bi/Sb ratio were fabricated. The microstructure and thermoelectric properties of the films were sensitive to variations in the chemical composition. In the first case of Bi/Te ratio, we have prepared targets by cold press according to the formula $Bi_{10-x}Sb_{30}Te_{60+x}$ (x=2-6). As we observed from the SEM images, a second face of Te appeared in the targets. The films after annealing treatment had considerable change in the elemental concentration, which did not correspond to those of targets. As a consequence of the "bad" stoichiometry, the thermoelectric properties of these films were not as expected however, they directed us to grow BST films with different Bi/Sb ratio which led to the highest PF of this work.

Second, we prepared targets by cold press according to the formula $Bi_{10-x}Sb_{30+x}Te_{60+1\%wt}$ (x=0-6), in order to investigate the influence of the Sb content on the thermoelectric properties of BST films, grown at RT and annealed at 300°C for 16h in vacuum. When the Sb content in BST films increased from x=2 to 4, the grain size shows an obvious increase and voids appear on the surface. The carrier concentration increased as the Sb content increased from $2.23x10^{19}$ to $3.9x10^{19}$ cm^{-3}. The largest PF at 390K (3820 $\mu W/mK^2$) was obtained for the $Bi_8Sb_{32}Te_{60+1\%wt}$ film with an electrical resistivity and Seebeck coefficient of $1.5x10^{-5}$ Ohm.m and 240μV/K, respectively. This value is the highest one ever reported in the case of BST films on fused silica substrates.

Chapter 4

$Bi_{0.5}Sb_{1.5}Te_3$ Bulk alloy

4.1 The Effect of Bi/Sb Ratio on Thermoelectric Properties of p-type Nanostructured $Bi_xSb_{2-x}Te_3$ Alloys prepared by Hot Press and Hot Deformation methods

P-type BST is currently heavily used in room-temperature commercial thermoelectric refrigeration applications due to its relatively high ZT~1. Even though this material has been investigated extensively for several decades, recent findings indicate that there may be room for further improvement in its efficiency and thus, it could be a good system to revisit for exploring higher ZT.

4.1.1 Motivation

In the last part of this work, polycrystalline solid solutions of p-type $Bi_{0.5-x}Sb_{1.5+x}Te_3$ were fabricated by both a hot press (HP) and hot deformation (HD) method, with the aim of identifying preparation conditions that could improve the thermoelectric performance of BST. Focus has been given on the two main issues concerning BST alloys: anisotropy and intrinsic conduction. By measuring all thermoelectric properties in the same direction, we calculated reliable ZT values and by increasing the concentration of Sb in the BST alloys we succeeded in shifting the maximum ZT value at temperatures higher than room temperature. It is noteworthy, that a number of published works have reported high ZT values without taking into account or discussing in detail the issue of anisotropy (118), (119), (120). It will be shown that the Lotgering factor F, which is the most frequently used method to quantify the degree of preferred orientation from XRD results, may not always be an effective criterion in estimating the extent to which physical properties, such as thermal conductivity, are affected by the anisotropy. For example, for BST samples with F=0.10, based on which they were characterized as nearly isotropic, a high ZT value was calculated using κ values measured along a different direction

than the one S and ρ were measured (118), (121). In this chapter, it will be shown that, for a BST sample with F=0.15, a quite different ZT was obtained depending on whether κ was measured along the same direction as S and ρ (ZT~1.12) or along a different direction than S and ρ (ZT~1.66). The present section has been submitted for publication in the Journal of Solid State Chemistry.

4.1.2 Hot press method

In the first section of this chapter, we discuss the effect of Sb content on the thermoelectric properties of BST samples prepared by the HP method. The investigated samples $Bi_{0.5}Sb_{1.5}Te_3$, $Bi_{0.4}Sb_{1.6}Te_3$, $Bi_{0.3}Sb_{1.7}Te_3$, and $Bi_{0.2}Sb_{1.8}Te_3$ were labeled as HP-0.5, HP-0.4, HP-0.3 and HP-0.2, respectively. Table 4.1 shows the chemical composition of the HP-BST samples determined by EDX. Taking into account that there is an overlap between the peaks of Sb and Te in EDX spectra and that the relative error is ~5%, we consider the HP-BST samples as being nearly stoichiometric (107).

Sample name (nominal stoichiometry)	**Chemical composition (at %)**			**Carrier concentration and hole mobility at 300K**	
	Bi	Sb	Te	p (x10^{19} /cm^3)	μ (cm^2/V*s)
HP-0.5 (10/30/60)	8.95	30.23	60.82	1.68	291
HP-0.4 (8/32/60)	7.07	32.71	60.22	1.825	273
HP-0.3 (6/34/60)	5.43	35.15	59.43	2.535	283
HP-0.2 (4/36/60)	3.70	36.76	59.55	2.995	400

Table 4.1. *Chemical composition, carrier concentration n_H and hole mobility μ_H at 300K for the HP-BST samples*.

Figure 4.1a shows typical XRD diffraction patterns of all BST samples for two different configurations, namely the in-plane configuration (the X-ray beam was incident on the surface of the sample which was perpendicular to the hot press direction) and the cross-plane configuration (the X-ray beam was incident on the surface of the sample which was parallel to

the hot press direction). All the observed diffraction peaks were indexed to the rhombohedral BST phase and no other impurity phase was found. The (00ℓ) diffraction intensities in the in-plane XRD pattern are much higher than the ones in the cross-plane XRD pattern, revealing the existence of preferred orientation in the in-plane configuration. The Lotgering factor (F) was used to quantify the degree of preferred orientation of the (00l) planes. F was calculated based on the formula $F=(P-P_0)/(1-P_0)$, with $P_0=I_0(00\ell)/\Sigma I_0(hk\ell)$ and $P=I(00\ell)/\Sigma I(hk\ell)$, where $I_0(hk\ell)$ and $I(hk\ell)$ are the peak intensities of a randomly oriented sample and the measured sample, respectively (122). As shown in Figue 4.1b, the in-plane F value decreases as the Sb content increases, taking values from 0.19 to 0.11. On the other hand, the cross-plane F value is negative indicating that the experimentally observed relative intensity of that diffraction line is less than the value expected for a randomly oriented sample (123). This difference in the F values of the two configurations clearly indicates microstructural anisotropy in the BST samples. This is further confirmed from Figure 4.1c, which shows the relative intensity of (0015) peak as a function of Sb content, for both studied configurations. The dash line corresponds to the (0015) relative intensity of a randomly oriented sample. It is evident that the relative intensity of the (0015) peak in the cross-plane configuration is much lower than that of a randomly oriented sample. On the other hand, for the in-plane configuration, we observed that the relative intensity of the (0015) peaks is higher than that of a randomly oriented sample and decreases from 76% to 32% with increasing Sb content. Figure 4.2 depicts a typical SEM image of the surface parallel to the hot press direction, for all HP-BST samples. In good agreement with the XRD results, partially oriented grains were observed. It is, therefore, expected that the thermoelectric properties (vide infra) are affected by the microscale texture evolution.

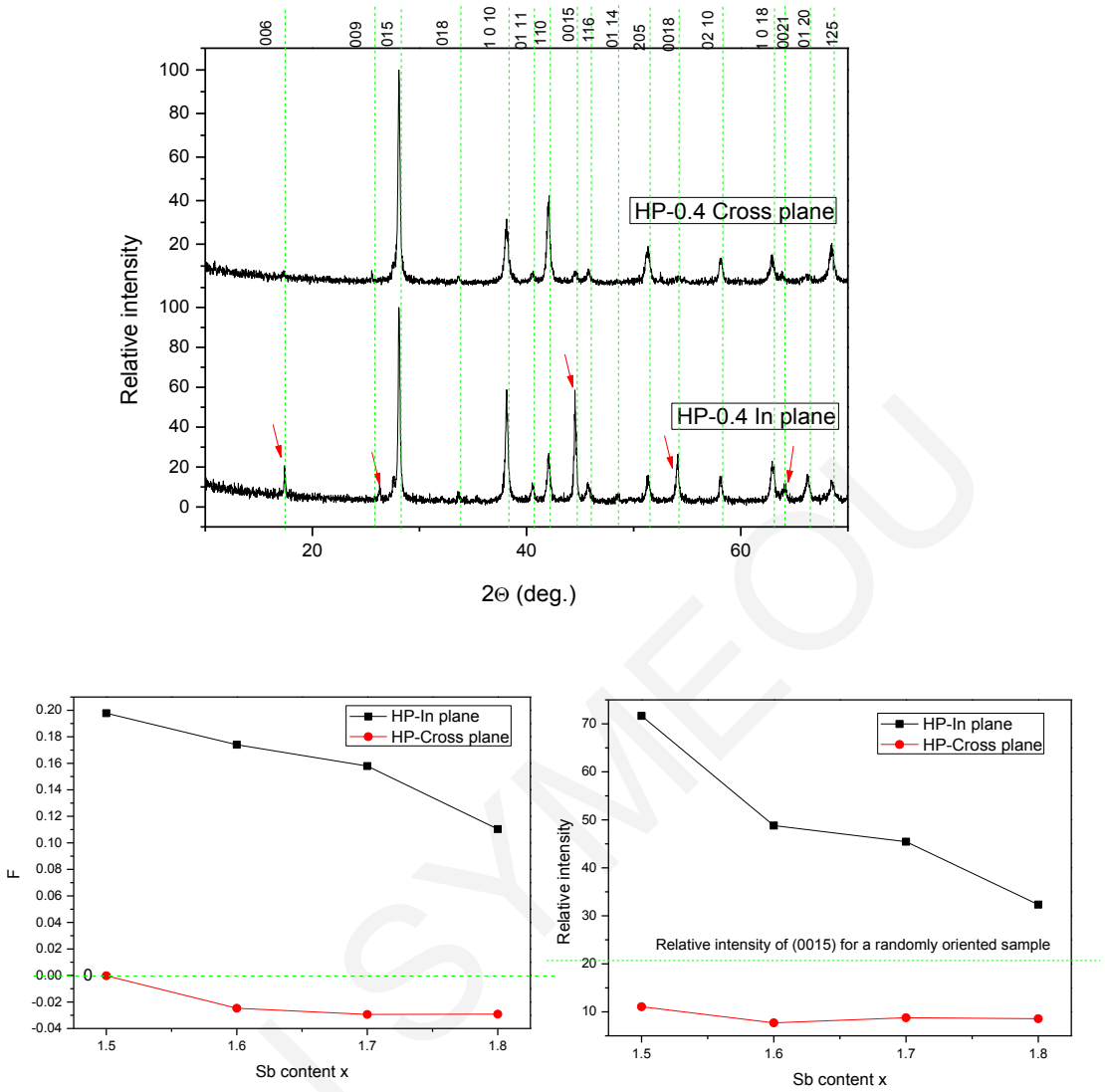

Figure 4.1. *XRD analysis of the HP-BST samples for both in-plane and cross-plane directions.* ***(a)*** *Typical XRD diffraction patterns of all samples - the Miller indices of all major peaks are indicated,* ***(b)*** *Lotgering factor F as a function of Sb content,* ***(c)*** *relative intensity of (0015) peak as a function of Sb content.*

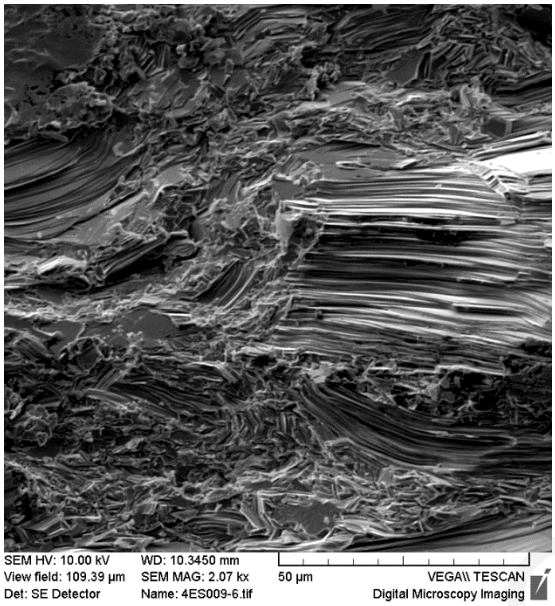

Figure 4.2. *Typical SEM image of the surface parallel to the pressing direction for HP-BST samples.*

Next, we discuss the influence of Sb concentration on the Hall carrier concentration (n_H) and carrier mobility (μ_H) of the samples based on the data presented in Table 4.1. The observed increase of n_H with increasing Sb concentration is attributed to the formation of more antisite defects. Raising the Sb content in $Bi_{0.5-x}Sb_{1.5+x}Te_3$ promotes a reduction in the formation energy of antisite defects, because of the smaller difference in electronegativity (X_{Sb} = 1.9, X_{Bi} = 1.8 and X_{Te} = 2.1) for low-polarity Sb-Te bonds compared with low-polarity Bi-Te bonds. Moreover, the increase in μ_H with increasing Sb content is most likely related to the reduced alloy scattering of the carriers (67). This tendency agreed with those previously reported (69), (67), (124).

The temperature dependence of thermoelectric properties of the HP-BST samples with various Sb contents is illustrated in Figure 4.3. As can be seen in Figures 4.3a and 4.3b, S and ρ vary linearly with temperature (in the range 250-390K) indicating a metal-like conduction behavior for all studied BST samples. S at 375K decreased from 240 to 165µv/K with increasing Sb content from x=0 to 0.3. This change in S is attributed to the carrier concentration variation with Sb content. Specifically, according to the next equation, S is directly proportional to the scattering factor (γ) and inversely proportional to the logarithmic carrier concentration (n):

$$S = \frac{k_B}{q}\left[\left(\frac{5}{2} + \gamma\right) - \ell n(n)\right]$$

where k_B is the Boltzmann's constant and q is the electron charge (111). Furthermore, similarly to S, $\rho = (1/n_H.e.\mu_H)$ decreases as n increases. ρ at 375K decreased from $2.1\text{x}10^{-5}$ Ohm.m to $6\text{x}10^{-6}$ Ohm.m with increasing Sb content from x=0 to 0.3. Figure 4.3c displays the temperature dependence of the calculated PF values for all BST samples. It is evident that PF increases with increasing Sb content, mainly because of a substantial improvement in ρ. The highest obtained PF value is 4600μW/mK^2 at 375K for HP-0.2 sample (S=165μV/K and $\rho=6\text{x}10^{-6}$ Ohm.m).

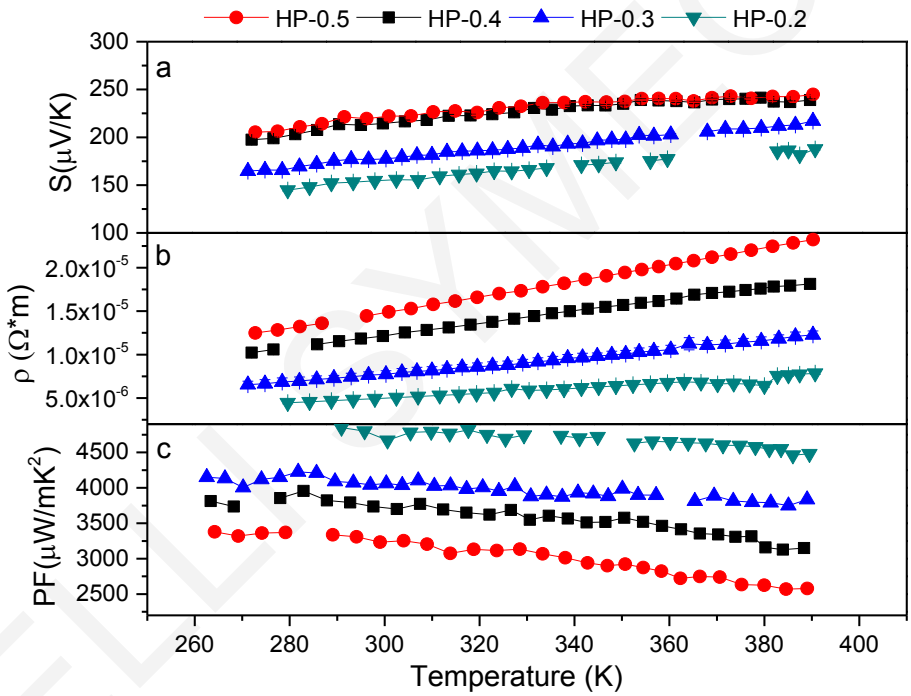

Figure 4.3. *Temperature dependence of* ***(a)*** *Seebeck coefficient S,* ***(b)*** *electrical resistivity ρ, and* ***(c)*** *power factor PF for the HP-BST samples.*

For the investigation of the in-plane thermal conductivity of BST samples, i.e., the measurement of κ along the same direction S and ρ were measured (perpendicular to the hot press direction), we used the method introduced by Xie et al. (3). The configuration of the samples is shown in Figure 4.4. Initially, the thermal diffusivity (D) of a test sample was measured in the cross-plane

direction (i.e., parallel to the hot press direction). The test sample was then cut into four bars which were glued together to preserve the cross-plane direction. The D of the glued sample was measured to determine whether the glue has any effect on it. We found that there was no difference between the D of the first and the second measurement, within the error of the measurement. Then, all BST samples were cut into four bars, rotated 90° counterclockwise and glued together. This re-configuration of BST samples allowed the measurement of D along the in-plane direction.

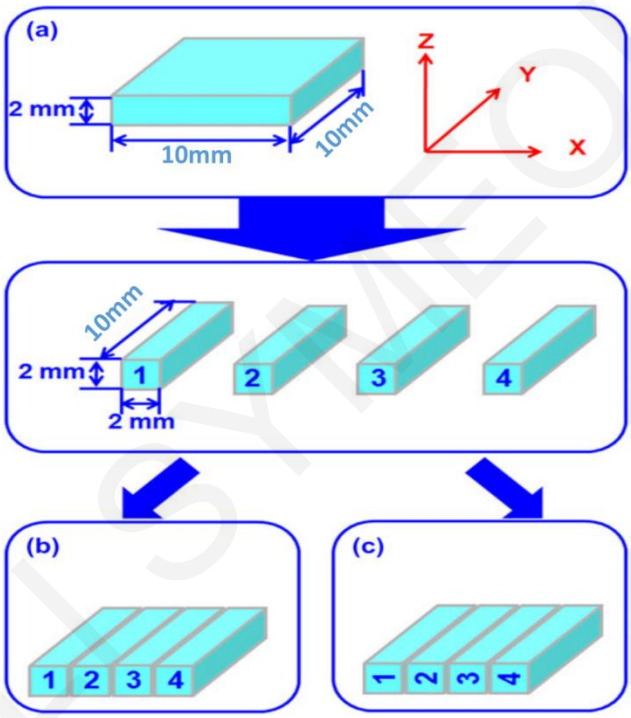

Figure 4.4. Three step measurement procedures for the reorientation of the BST samples. Z is pararel to the HP direction and X, Y are perpendicular to the HP direction. Re-produced from W. Xie et al. (3).

Finally, κ was calculated for all BST samples using the relation $\kappa=D.\rho_s.C_p$ (Figure 4.5a). The increment of κ with increasing Sb content is mainly attributed to an increase in the electronic contribution κ_{el}, which was estimated using the Wiedemann-Franz relationship, $\kappa_{el}=L_0\sigma T$, where $L_0=2.44x10^{-8}V^2/K^2$ is the Lorentz constant. The κ_{el}, at 375K, increased from ~ 0.35W/m.K for sample HP-0.2 to 1.10 W/m.K for sample HP-0.5 (Figure 4.5b). The lattice and ambipolar thermal conductivity κ-κ_{el} were calculated by subtracting κ_{el} from the total in-plane κ. The κ-κ_{el}

still increases with increasing temperature, while the lattice thermal conductivity decreases as 1/T. These trends are known to be due to the additional contribution caused by the bipolar effect, arising from the diffusion of electron-hole pairs with the onset of intrinsic contribution (67). Samples HP-0.5 and HP-0.4 exhibit higher κ-κ_{el} values compared with samples HP-0.3 and HP-0.2, because of their enhanced (00ℓ) texture (Figure 4.5c). Another possible reason is that the increasing Sb content could further enhance phonon scattering due to random mass and lattice strain fluctuations as the average atomic mass of Sb_2Te_3 compound (125.3) is larger than that of Bi_2Te_3 (116.02). (125).

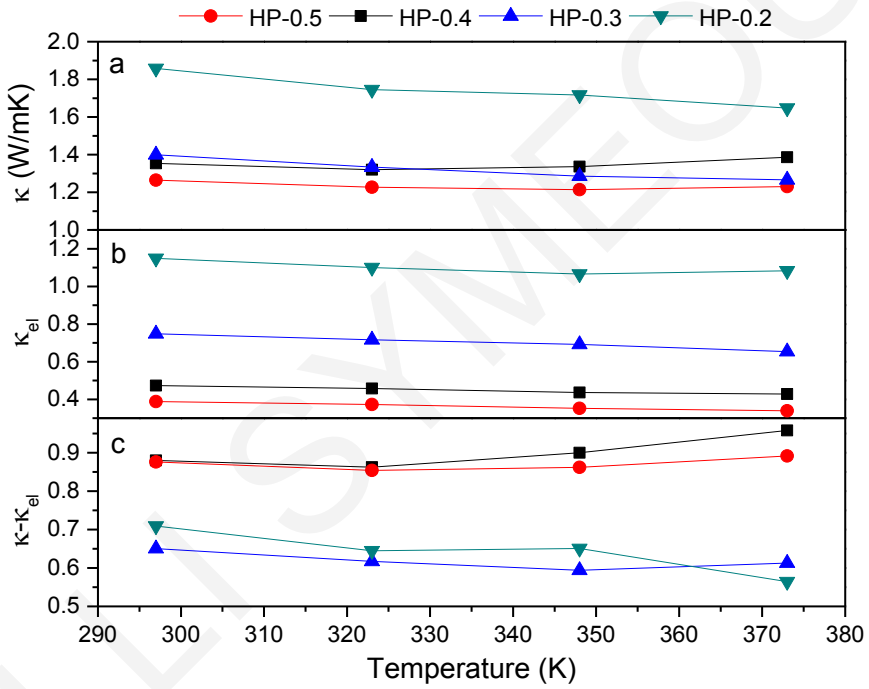

Figure 4.5. *Temperature dependence of* ***(a)*** *total thermal conductivity κ,* ***(b)*** *electronic thermal conductivity κ_{el}, and* ***(c)*** *lattice and ambipolar thermal conductivity κ-κ_{el} for the HP-BST samples along the in-plane direction.*

As shown in Figure 4.6, the dimensionless figure of merit, along the *in-plane* direction, reaches its highest value of ZT~1.12 at 375K for sample HP-0.3 ($Bi_{0.3}Sb_{1.7}Te_3$). This sample exhibits one of the highest PF and lowest κ values among the investigated samples. On the other hand, samples HP-0.5 and HP-0.4 exhibit their highest ZT values of 0.82 and 0.92, respectively, around 350K. In conclusion, increasing Sb content in HP-BST samples results in both an increase of the maximum value of ZT and a concurrent increase in the temperature at which this

maximum ZT value is obtained. Also, as shown in Table 4.2, a false maximum ZT of 1.66 could be obtained (more than 45% overestimation), if we had been misled by the apparent weak texture of the samples and used, in the calculation of ZT, values of S, ρ and κ that had been measured along different directions. A similar observation has also been reported by Shen *et al*. (126).

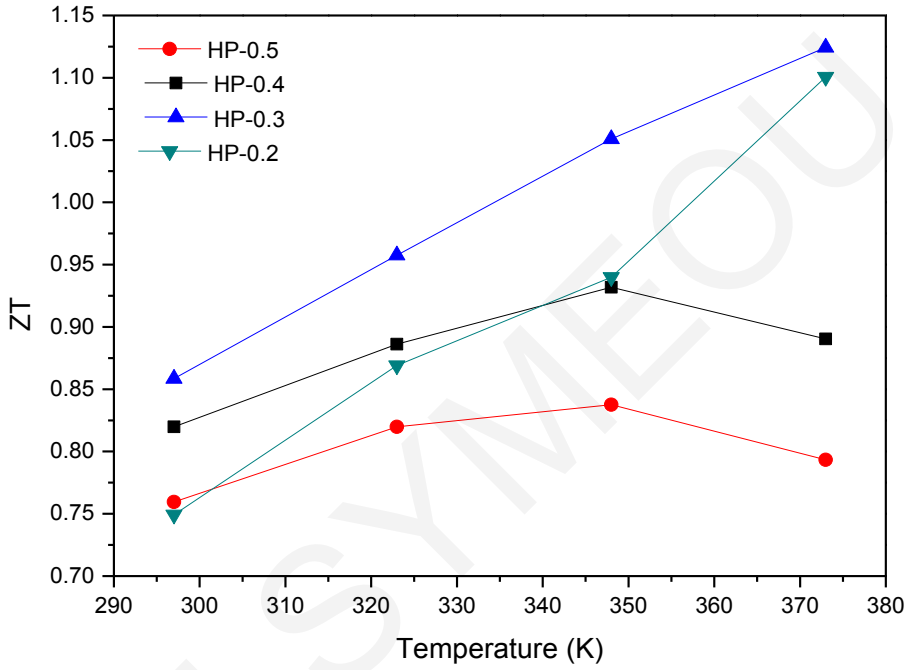

Figure 4.6. *Temperature dependence of the thermoelectric figure of merit ZT for the HP-BST samples.*

F factor=0.15	**S (μv/K) in-plane**	**ρ (Ohm.m) in-plane**	**K (W/mK) in-plane**	**ZT in-plane**	**K (W/mK) cross-plane (false direction)**	**ZT In/cross-plane**
HP-0.3	208.783	1.14E-05	1.647	1.1	0.868	1.66

Table 4.2. *In-plane Seebeck coefficient S, in-plane resistivity ρ, in-plane thermal conductivity K, in plane ZT, cross-plane conductivity K, and ZT calculated using in-plane S and ρ and cross-plane K for sample HP-0.3 BST sample at 375K.*

4.1.3 Hot deformation method

Even though the PF of the HP-BST samples is very high, the ZT values are still not high enough for use in large-scale thermoelectric applications, because of their high thermal conductivity. Reduction in lattice thermal conductivity could be achieved by phonon scattering through interfaces and boundaries related to nanostructuring (127). Shen et al. (71) have reported that hot deformation (HD) could reduce the lattice thermal conductivity of BST samples through the formation of partial recrystallization-induced in situ nanostructures and of high density lattice defects. This novel approach has been applied on just a few occasions with encouraging results (69), (70), (128). Inspired by these works, we investigated the effect of HD on the thermoelectric properties of our BST samples, i.e., consolidated powders produced by hand grinding of ingots which were prepared by melting stoichiometric metal mixtures with excess Te (4wt%).

First, we prepared a series of $Bi_{0.5}Sb_{1.5}Te_3$ samples to investigate how the temperature used in the first-HP step affects the thermoelectric properties of the samples obtained following the second-HD step. To this end, we compared the results for four samples prepared by: HP at 340°C; HP at 420°C; HP at 340°C followed by HD at 500°C; and HP at 420°C followed by HD at 500°C. The axial pressure and time duration used in the HP and HD steps are mentioned in the experimental section.

The temperature dependence of S, ρ and PF for the above BST samples is shown in Figure 4.7. Both the Seebeck coefficient (Figure 4.7a) and the resistivity (Figure 4.7b) of the HD samples are higher than those of their HP counterparts, likely as a result of reduced hole concentration and enhanced carrier scattering by the crystal defects induced by HD processing. As a result of the enhanced Seebeck coefficient, the HD samples exhibit the highest PF (Figure 4.7c), which is about 33% larger than that of their HP counterparts. Surprisingly, S, ρ and PF of the HD samples seem not to be affected by the temperature used for the first-HP step even though the samples prepared only by HP at different temperatures exhibit different S, ρ and PF values. Based on these observations, we decided, for the rest of the study, to use the lowest of the investigated temperatures for the first-HP step, i.e., HP at 340°C, because one of the aims of our work is to identify the least energy-consuming processing steps.

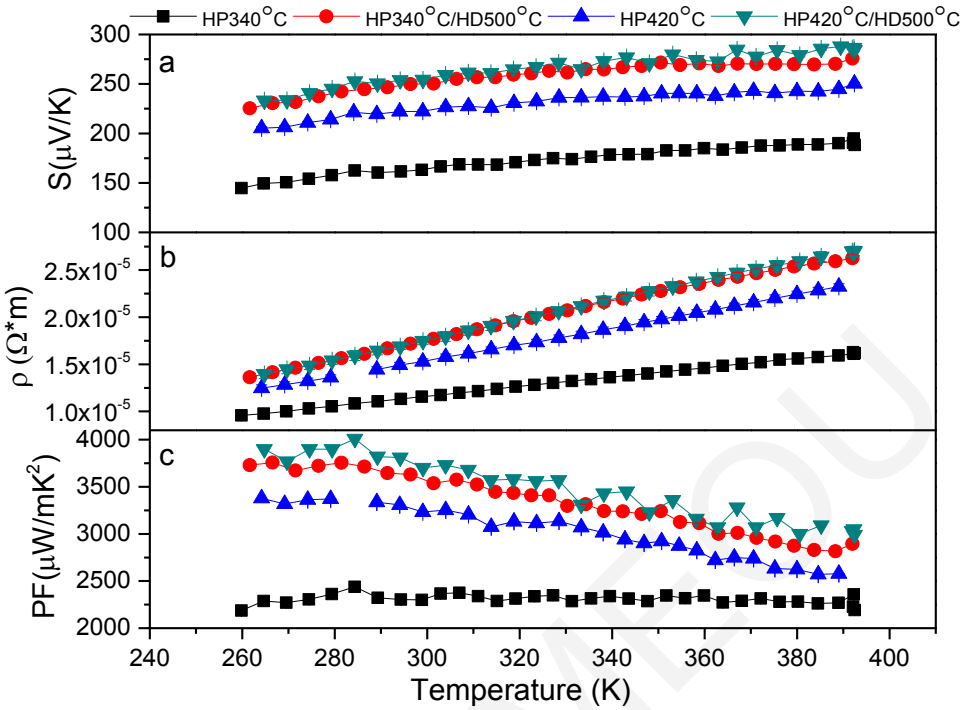

Figure 4.7. *Temperature dependence of* ***(a)*** *Seebeck coefficient S,* ***(b)*** *electrical resistivity ρ, and* ***(c)*** *power factor PF for BST samples prepared at different HP and HD temperatures.*

Next, we prepared a series of BST samples with different Sb content: $Bi_{0.5}Sb_{1.5}Te_3$, $Bi_{0.4}Sb_{1.6}Te_3$, $Bi_{0.3}Sb_{1.7}Te_3$, and $Bi_{0.2}Sb_{1.8}Te_3$, which were labeled HD-0.5, HD-0.4, HD-0.3 and HD-0.2, respectively. The composition of these samples was investigated by EDX (Table 4.3). The stoichiometry of the HD samples deviates from the nominal one, probably because of the evaporation of the volatile Te. By comparing the stoichiometry of the HP samples (Table 4.1) with the one of the HD samples, we conclude that the change in stoichiometry occurs during the HD process and not during the melting or HP process.

Figure 4.8a shows typical in-plane and cross-plane XRD patterns for the HP-BST samples investigated. All the observed diffraction peaks were indexed to the rhombohedral BST phase and no other impurity phase was found. The (00l) diffraction intensities in the in-plane XRD pattern are much higher than those in the cross-plane XRD pattern, revealing the existence of preferred (00l) orientation in the in-plane configuration (perpendicular to the hot press direction). As shown in Figure 4.8b, the in-plane F value exhibits a non-monotonic behavior,

i.e., F is about 0.29 for HD-0.5, then decreases to 0.16 for HD-0.4 and again increases to 0.21 and 0.23 for HD-0.3 and HD-0.2, respectively. On the other hand, the *cross-plane* F value was slightly negative for HD-0.5, HD-0.4 and HD-0.3 and positive for HD-0.2. As shown in Figures 4.1b and 4.1b, the in-plane F values increase from 0.11-0.19 in the HP samples to 0.16-0.29 in the HD samples. The HD step seems to induce enhanced texture in the BST samples likely as a result of the creation of plastic deformation which leads to sliding and alignment of the grains in the in-plane direction. Figure 4.8c shows the relative intensity of (0015) peak as a function of Sb content, for both the in-plane and cross-plane configurations. The dash line corresponds to the relative intensity (0015) of a randomly oriented sample. In the cross-plane configuration the relative intensity of the (0015) peak is much lower than the one of a randomly oriented sample. On the other hand, for the in-plane configuration, the relative intensity of the (0015) peaks is much higher than that of a randomly oriented sample and follows the same trend as the F factor. Figure 4.9 depicts a typical SEM image of the surface parallel to the hot deformation direction. In good agreement with the XRD results, the (00l) orientation of the HD samples seems to be enhanced in comparison with their HP counterparts.

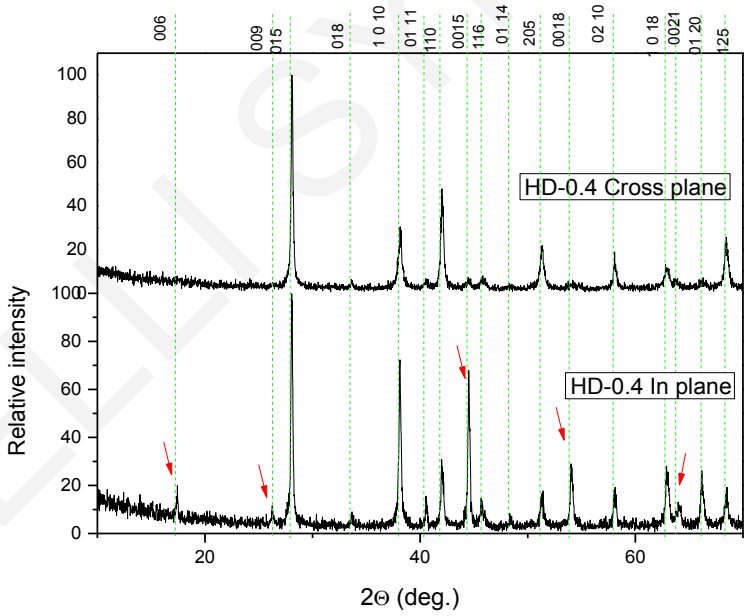

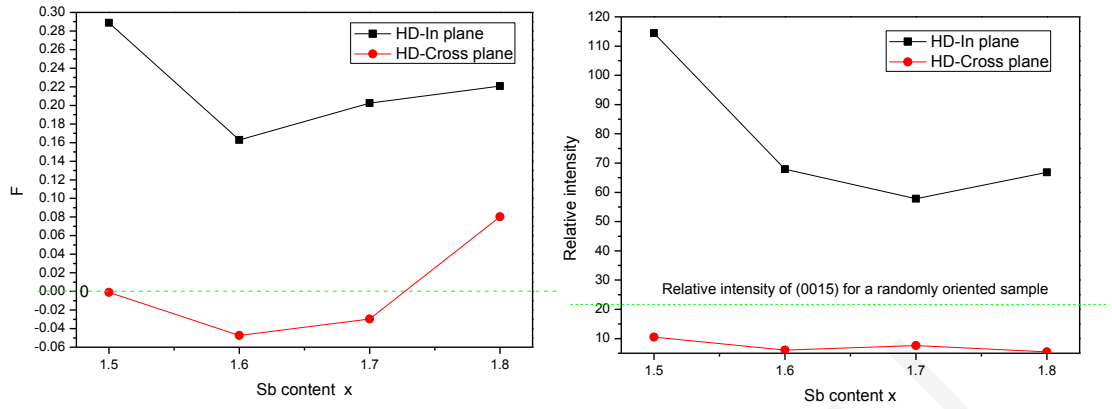

Figure 4.8. *XRD analysis of the HD-BST samples for both in-plane and cross-plane directions.* ***(a)*** *Typical XRD diffraction patterns of all samples - the Miller indices of all major peaks are indicated,* ***(b)*** *Lotgering factor F as a function of Sb content,* ***(c)*** *relative intensity of (0015) peak as a function of Sb content.*

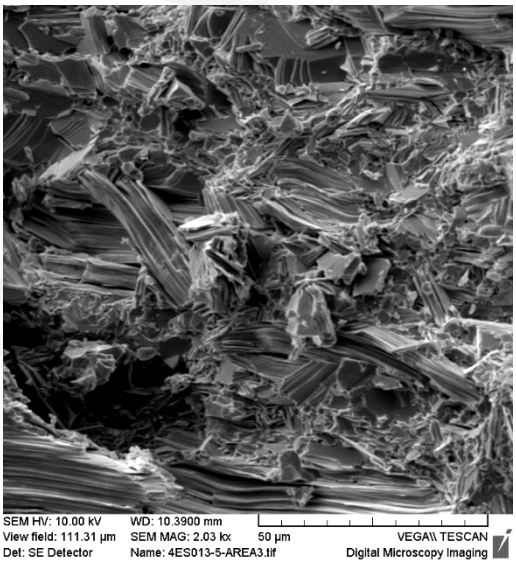

Figure 4.9. *Typical SEM image of the surface parallel to the pressing direction for HD-BST samples.*

Table 4.3 presents the n_H and μ_H values obtained at 300K for the HD samples. Both n_H and μ_H increase with increasing Sb content similarly to the case of HP samples discussed earlier.

However, the HD samples have a slightly smaller mobility than their HP counterparts even though they exhibit more enhanced (00l) texture (129). This could be explained by taking into account that the HD process is expected to generate a high density of lattice defects and as a consequence, carrier scattering is enhanced and hence, μ_H is reduced (128).

Sample name (nominal stoichiometry)	**Chemical composition (at%)**			**Carrier concentration and mobility at 300K**	
	Bi	Sb	Te	p (x10^{19}/cm^3)	μ (cm^2/V*s)
HD-0.5 (10/30/60)	8.94	32.26	58.82	1.49	236
HD-0.4 (8/32/60)	7.3	34.7	57.93	1.665	291
HD-0.3 (6/34/60)	5.59	36.13	58.28	2.765	297
HD-0.2 (4/36/60)	3.81	38.58	57.62	3.385	372

Table 4.3. *Chemical composition, carrier concentration n_H and hole mobility μ_H at 300K for the HD-BST samples.*

Figure 4.10 presents the thermoelectric properties (S, ρ, and PF) of HD-BST samples with various Sb content as a function of temperature. As can be seen in Figures 4.10a and 4.10b, S and ρ vary linearly with temperature (in the range 250-390K) indicating a metal-like conduction behavior for all studied HD samples. S(375K) decreases from 270 to 170μv/K and ρ(375K) decreases from $2.5x10^{-5}$ Ohm.m to $7x10^{-6}$ Ohm.m, with increasing Sb content from x=0 to 0.3. This change in S and ρ is attributed to the carrier concentration variation with Sb content (130). The ρ of the HD-samples increases slightly compared with the ρ of the HP-samples due to the introduction of crystal defects, such as point defects and dislocations, during the HD process. Figure 4.10c displays the temperature dependence of the calculated PF values for all HD-BST samples. PF increases with increasing Sb content and the highest PF value is 4700μW/mK^2 at 375K for samples HD-0.2 and HD-03. Comparing now the PF values obtained for HP and HD samples, it becomes evident that the HD samples exhibit slightly higher PF values, most likely because of the enhancement in the Seebeck coefficient.

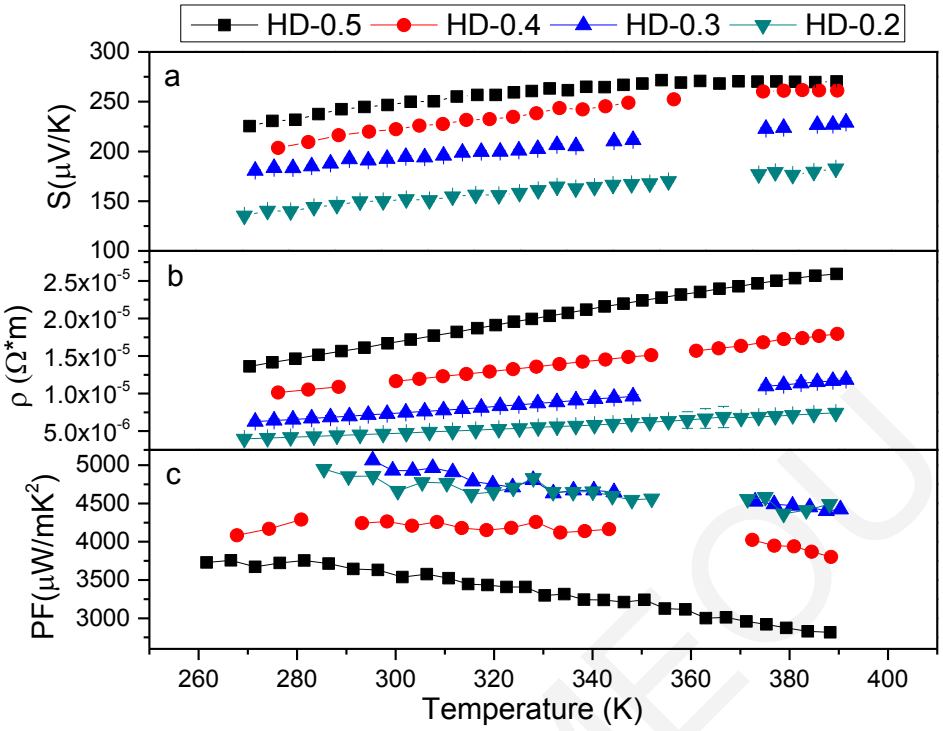

Figure 4.10. *Temperature dependence of* ***(a)*** *Seebeck coefficient S,* ***(b)*** *electrical resistivity ρ, and* ***(c)*** *power factor PF for the HD-BST samples.*

The temperature dependence of the total *in-plane* thermal conductivity κ for the HD-BST samples is plotted in Fig. 4.11a. The monotonic increase of κ with increasing Sb content is mainly attributed to an increase in the electronic contribution κ_{el}, as shown in Figure 4.11b, which stems from the decrease in ρ due to the increase in $n_{H.}$ (70) κ_{el} at 375K increases monotonically with increasing Sb content from ~0.3W/m.K for sample HD-0.5 to 1.10 W/mK for sample HD-0.2. On the other hand, the lattice and ambipolar thermal conductivity κ-κ_{el} (Figure 4.11c) exhibits a non-monotonic behavior as a function of Sb content, i.e., samples HD-0.3 and HD-0.5 exhibit higher κ-κ_{el} values compared with samples HD-0.4 and HD-0.2. In general, the κ-κ_{el} values of the HD samples seem to be similar to those of the HP samples (Figure 4.5c) indicating that the HD process was not as effective in reducing the total thermal conductivity of our samples as in other studies. This result may be related to the fact that the decrease of κ due to plastic deformation that takes place in the HD samples is compensated by the increase of κ due to the enhancement of the (00l) texture in the HD samples. Another possible explanation is that in our case the HD process has not resulted in strongly phonon scattering

nanostructures and lattice defects. This issue requires further investigation. It is noted, that we hot deformed BST samples using a bigger die (D=15mm) but the thermal conductivity did not change.

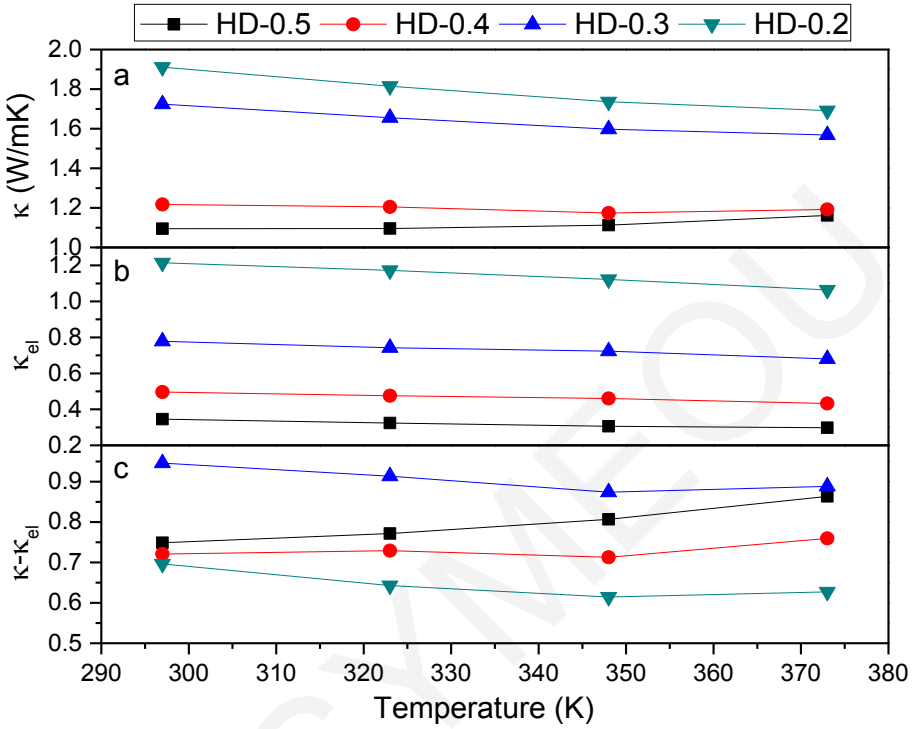

Figure 4.11. *Temperature dependence of* ***(a)*** *total thermal conductivity κ,* ***(b)*** *electronic thermal conductivity* κ_{el}*, and* ***(c)*** *lattice and ambipolar thermal conductivity* κ-κ_{el} *for the HD-BST samples along the in-plane direction.*

Finally, the calculated ZT values for the HD-BST samples are shown in Figure 4.12. Sample HD-0.4 ($Bi_{0.4}Sb_{1.6}Te_3$) exhibits the highest *in-plane* ZT value of 1.24 in the temperature range 350K to 373K. This ZT value is among the highest ever reported for p-type BST materials. As shown in Table 4.4, again, a false maximum ZT of 2.01 could be obtained, if we had been misled by the apparent weak texture of the samples and used, in the calculation of ZT, values of S, ρ and κ that had been measured along different directions.

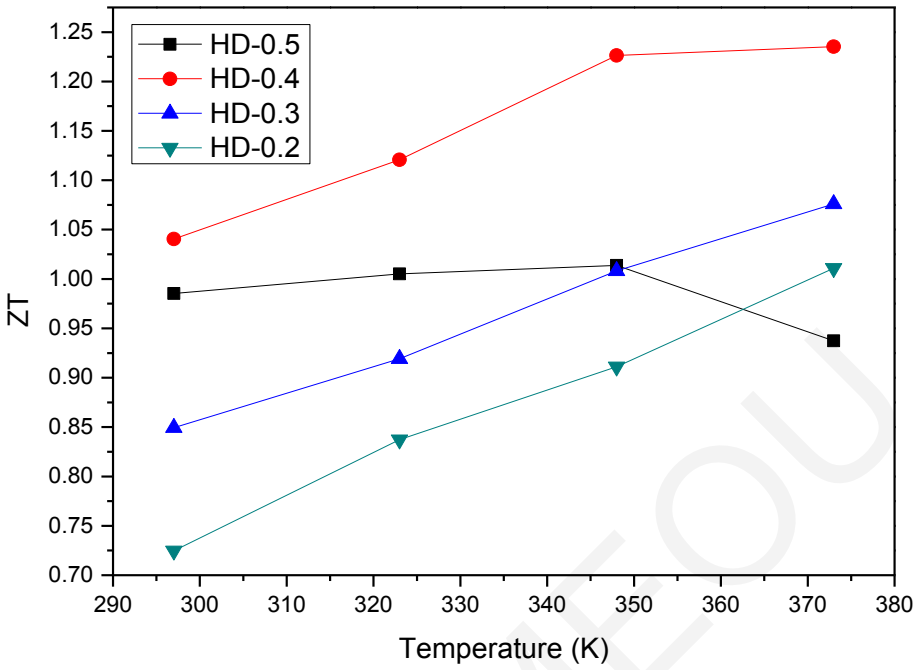

Figure 4.12. *Temperature dependence of the thermoelectric figure of merit ZT for the HD-BST samples.*

F factor=0.16	**S (µv/K) in-plane**	**ρ (Ohm.m) in-plane**	**K (W/mK) in-plane**	**ZT in-plane**	**K (W/mK) cross-plane (false direction)**	**ZT In/cross-plane**
HD-0.4	261	1.73E-05	1.19	1.24	0.73	2.01

Table 4.4. *In-plane Seebeck coefficient S, in-plane resistivity ρ, in-plane thermal conductivity K, in plane ZT, cross-plane conductivity K, and ZT calculated using in-plane S and ρ and cross-plane K for sample HD-0.4 BST sample at 375K.*

4.1.4 Conclusions

We have studied the influence of Sb content on the thermoelectric properties of HP and HD BST samples prepared with an extra amount of Te (4%wt). We have achieved a high in-plane ZT value of ~1.12 at 375K for $Bi_{0.3}Sb_{1.7}Te_3$ and average ZT of 1, which was prepared using the HP method. We have shown that a false maximum ZT of 1.66 could be obtained, if S, ρ and κ were measured along different directions assuming that the sample is isotropic because of its low F value. Also, we have studied the influence of the HD method on the thermoelectric properties of BST samples. The in-plane ZT reaches a maximum value of ~1.24 in the temperature range 350K to 373K for $Bi_{0.4}Sb_{1.6}Te_3$ and an average ZT of 1.15 in the range of 295-375K.

Chapter 5

5. Conclusions

The escalating energy crisis and the threatening global warming are critical issues that require our immediate attention. One potential solution may be the use of thermoelectric generators to "recycle" the huge amount of waste heat emitted (including solar thermal energy) into electricity and of thermoelectric cooling devices to achieve efficient thermal management in an environmentally friendly way. The main disadvantages of these thermoelectric devices are low efficiency and high cost. The future expansion of thermoelectric technology, beyond niche applications, is thus tied primarily to the enhancement of materials performance across the temperature range of interest. The efficiency of thermoelectric materials depends on the temperature dependent transport coefficients through the dimensionless thermoelectric figure of merit: $ZT= (S^2 /\rho. \kappa)$ where S, ρ, κ and T are the Seebeck coefficient, electrical resistivity, total thermal conductivity and absolute temperature, respectively. Another crucial criterion to characterize thermoelectric materials is the power factor, defined as $PF= S^2/\rho$. A good thermoelectric material must combine a large Seebeck coefficient (S) with low electrical resistivity (ρ) and low thermal conductivity (κ).

5.1 $Bi_{0.5}Sb_{1.5}Te_3$ thin films

As there are not many works on the growth of BST films by PLD, during the first part of this thesis we have carried out a **systematic investigation of the condition parameters which are far from being independent and affect the growth and quality of the resulting BST film**. The stoichiometric removal of material from a target is undoubtedly the single most important factor in the success of PLD. First, we have studied how the **laser fluence** affects the stoichiometry of the BST films. We observed that using fluences below 1.5 J/cm^2 the films have slight deficiency in Bi and above F=2 J/cm^2 the films have deficiency in Te. The optimum

stoichiometry is achieved using fluence 2 J/cm^2. Next we have grown BST films with varying the number of pulses and consequently the **thickness** of the films. Films thicker than 280nm have microcracks and the coalescence of these cracks leads to exfoliation. On the other hand, BST films thinner than 180nm are dense with smooth surfaces. The best PF is obtained for 180 nm-thick films, because of their lower resistivity than the other samples. The surface scattering of charge carriers is reduced resulting in the increase of the carrier mean free path. Finally, we have grown BST films at different **substrates temperatures**. It was evident that the films grown at substrate temperatures lower than 150°C are amorphous and as the substrate temperature increases above 150°C the crystallinity of the films improves. The film deposited at 350°C is fully oriented and the observed (00l) reflections indicate preferential growth along the c-axis of the BST film. The film deposited at 350°C exhibits the best PF over the entire temperature range investigated; e.g., PF= 2600 $\mu W/K^2m$ at 390 K. This PF value was still far from the PF value of the bulk BST samples.

In order to enhance the PF of the grown BST films, we investigated the effect of the three major **annealing parameters:** atmosphere, temperature and time duration, on the thermoelectric properties. We proceeded to grow BST films at RT which then underwent an ex-situ post-deposition annealing treatment at different temperatures (300°C, 350°C) and times (1h, 5h, 10h, 16h) in vacuum. SEM imaging reveals that annealing in Ar atmosphere results in the formation of particles and their areal density increases with increasing annealing duration. On the other hand, films annealed in vacuum have significantly less and smaller in size particles on their surface than the ones annealed in Ar atmosphere. It is evident that the surface morphology of the films remarkably changed following the post-annealing treatment at different temperatures in vacuum. However, following annealing at 300°C for 16h, crystallites are generated and following annealing at 350°C for 16h the size of the crystallites increases even further. All investigated BST films seem to exhibit a slight deficiency in Te concentration. This is likely attributed to the evaporation of volatile Te during annealing. Moreover, for the annealed BST films, the XRD patterns indicate that the film grains exhibit moderate texture with the preferred orientation direction varying depending on the temperature and time of the annealing process. The hole mobility increases with increasing annealing temperature and duration. This observation is attributed to the enhancement of grain growth, improvement of crystallinity and increased preferred grain orientation with increasing annealing temperature and duration. As a

consequence, the PF increases as the temperature and time of annealing increase. Specifically, PF (350°C/16h) > PF (350°C/10h) > PF (300°C/16h) > PF (300°C/10h) > PF (350°C/5h) > PF (350°C/1h) > PF (300°C/5h) > PF (300°C/1h). The BST film annealed at 350°C for 16h has a Seebeck coefficient of 210μV/K, an electrical resistivity of $1.15x10^{-5}$ Ohm.m and exhibits the highest PF value of 3750μW/mK^2 at 380K. This value is the highest one, ever reported in the case of BST films on fused silica substrates.

The second part of this work concerns the attempt to obtain BST films with bulk-like thermoelectric properties onto a **flexible substrate** such as Kapton, exploiting the experience we accumulated from the BST films grown on fused silica substrates (as discussed above). The influence of both substrate temperature and annealing process parameters on the thermoelectric properties of the BST films were investigated. It is evident that the films grown at substrate temperatures lower than 200°C are amorphous whereas films grown at temperatures higher than 200°C exhibit enhanced crystallinity and (1 0 10) preferred orientation. Also, for the film grown at 250°C the intensity of the diffraction peak assigned to (006) plane is enhanced. All films are characterized by a small deficiency in Te and an increasing Bi concentration as the substrate temperature increases. The BST film deposited at 250°C exhibits the best PF, which is 2600μW/mK^2 at 390K. This result is attributed to the enhanced (006) diffraction peak intensity. Next, we have grown BST films on Kapton substrates at RT and then post annealed at 250°C for 1h and 5 h. The reason we restricted our investigation to the particular annealing parameters is that BST films annealed at temperatures over 250°C exhibit microcracks and poor adhesion to Kapton. The XRD patterns reveal that the amorphous as-grown films undergo crystallization when they are subjected to annealing treatment. The BST film grown at RT and annealed at 250°C for 5h exhibits the highest PF value of 2600μW/mK^2 at 390K, which is the same as the one found for the case of BST films grown on Kapton substrates heated at 250°C. Although this PF value is lower than the bulk value, it is nevertheless the highest ever reported for BST films on flexible substrates.

Finally, BST thin films with different **Bi/Te and Bi/Sb ratio** were fabricated. The microstructure and thermoelectric properties of the films were sensitive to variations in the chemical composition. In the first case, we have prepared targets by cold press according to the formula $Bi_{10-x}Sb_{30}Te_{60+x}$ (x=2-6). As we observed, from the SEM images, a second face of Te

appeared in the targets. The films after annealing treatment, had considerable change in the elements concentration, which did not correspond to those of targets. As a consequence of the bad stoichiometry, the thermoelectric properties of these films were not as expected. Second, we have prepared targets by cold pressing according to the formula $Bi_{10-x}Sb_{30+x}Te_{60+1\%wt}$ (x=0-6), in order to investigate the influence of the Sb content on the thermoelectric properties of BST films, grown at RT and annealed at 300°C for 16h in vacuum.. The XRD patterns indicate that the films have polycrystalline rhombohedral structure with a preferred (1 0 10) orientation. A very small peak shift is observed with changing the Bi/Sb ratio due to a change in lattice parameters. When the Sb content in BST films was increased from x=2-4, the grain sizes show an obvious increase and voids appear on the surface. The carrier concentration was increased as the Sb content increased. The larger PF at 390K (3820 $\mu W/mK^2$) was obtained for the $Bi_8Sb_{32}Te_{60+1\%wt}$ film with an electrical resistivity and Seebeck coefficient of $1.5x10^{-5}$ Ohm.m and 240μV/K, respectively. This value is the highest one, ever reported in the case of BST films on fused silica substrates according to the formula $Bi_{10-x}Sb_{30+x}Te_{60+1\%wt.}$

Concluding, we can state that these results highlight the importance of annealing treatment in achieving good thermoelectric properties for room-temperature grown BST films and ultimately, in the development of highly efficient thin-film thermometric devices.

5.2 $Bi_{0.5}Sb_{1.5}Te_3$ bulk

Even though bulk BST material has been investigated extensively for several decades, recent findings indicate that there may be room for further improvement in its efficiency and it could be a good system to revisit. In the last part of this Thesis, polycrystalline solid solutions of p-type $Bi_{0.5-x}Sb_{1.5+x}Te_3$ were fabricated by both a **hot press (HP) and a hot deformation (HD) method**. Focus has been given on the two main issues concerning BST alloys: **anisotropy and intrinsic conduction.**

A high ZT value of ~1.12 at 375K and an average ZT_{av} of 1.15 was achieved, for $Bi_{0.3}Sb_{1.7}Te_3$, which was prepared using the HP method, and measuring all the properties in the same in-plane direction. Also, we have shown that a false maximum ZT of 1.66 could be obtained, if S, ρ and

κ were measured along different directions assuming that the sample is isotropic because of its low F value of 0.15.

Even though the PF of the HP-BST samples is very high, the ZT values are still not high enough for use in large-scale thermoelectric applications, because of their high thermal conductivity. The HD process seems to enhance texture in the BST samples most likely because of the creation of plastic deformation which leads to sliding and alignment of the grains in the in-plane direction. For this reason, we expected that the HD samples would have a lower thermal conductivity but this did not happen. Finally, the ZT, along the in-plane direction, reaches a maximum value of ~1.24 at 375K for HD $Bi_{0.4}Sb_{1.6}Te_3$ with an average ZT_{av} of 1.15, which are among the highest ever reported for p-type BST materials.

6. References

1. L. Zhao, V. P. Dravid and M. G. Kanatzidis. The panoscopic approach to high performance. Energy Environ. Sci, 2014, Vol. 7, 251-268.

2. Q. Jiang, H. Yan, J. Khaliq, H. Ning, S. Grasso, K. Simpson and M. J. Reece. Large ZT enhancement in hot forged nanostructured p-type Bi0.5Sb1.5Te3 bulk alloys. J. Mater. Chem. A, 2014, Vol. 2, 5785-5790.

3. Xie, W. Investigation of the sintering pressure and thermal conductivity. J. Mater. Res, 2011, Vol. 26, 1791-1799.

4. www.bp.com.

5. http://gmzenergy.com.

6. H. Alam, S. Ramakrishna. A review on the enhancement of figure of merit from bulk to nano-thermoelectric materials. Nano Energy, 2013, Vol. 2, 190-212.

7. D.M Rowe, Thermoelectrics Handbook: Macro to Nano. CRC Press, 2006.

8. T. M. Tritt. Encyclopedia of Materials: Science and Technology. 2002, Vol. 10, 1-11.

9. Subramanian and Terry M.Tritt. Thermoelectric Materials,Phenomena, and Applications: A Bird's Eye View. MRS Bulletin, 2006, Vol. 31, 188-229.

10. M. F. Silva, J. F. Ribeiro, J. P. Carmo, L. M. Gonçalves, J. H. Correia. Thin Films for Thermoelectric Applications. J. Nanosci. Nanotechnol , 2012, 485-528.

11. D.M. Rowe. Handbook on Thermoelectrics. CRC Press, 1995.

12. Z. G. Chen, G. Han, Lei Yang, L. Chenga, J. Zou. Nanostructured thermoelectric materials: Current research and future challenge. Materials International, 2012, Vol. 22, 535-549.

13. F.J. DiSalvo. Thermoelectric cooling and power generation. Sci, 1999, Vol. 285, 703.

14. M. He. Lin and F. Z. Qiu. Towards High-Performance Polymer-based Thermoelectric Materials. Energy Environ. Sci, 2013, Vol. 6, 1352-1361.

15. J. C. Vineis, A. Shakouri , A. Majumdar, M.G. Kanatzidis. Nanostructured Thermoelectrics: Big Efficiency Gains. Adv. Mater., 2010, Vol. 22, 3970-3980.

16. Short course on thermoelectrics. International Thermoelectric society, 2013, ebook: http://www.its.org/sct93.

17. A. J. Minnich, M. S. Dresselhaus, Z. F. Ren, and G. Chen. Bulk nanostructured. Bulk nanostructured thermoelectric materials: current research and future prospects. Energy Environ. Sci, 2009, Vol. 2, 5.

18. J. R. Sootsman, D. Y. Chung and M. G. Kanatzidis. New and Old Concepts in Thermoelectric Materials. Angew. Chem. Int. Ed, 2009, Vol. 48, 8616 – 8639.

19. B.V. Zeghbroeck, Principles of Semiconductor Devices. Principles of Semiconductor Devices. ebook: http://www.eletrica.ufpr.br/, 2011.

20. G. J. Snyder, and E. S.Toberer. Complex thermoelectric materials. Nat. Mater, 2008, Vol. 7, 105-114.

21. Y. Zhenwei. Fabrication and physical properties of thermoelectric thin films. Master of Engineering-Research Thesis, Institute for Superconducting and Electronic Materials, University of Wollongong , 2011.

22. J. Zheng. Recent advances on thermoelectric materials. Front. Phys, 2008, Vol. 3, 269-279.

23. C. Wood. Materials for thermoelectric energy conversion. Rep. Prog. Phys, 1988, Vol. 51, 459.

24. H. J. Goldsmid, and G. S. Nolas. A review of the new thermoelectric materials. 20th International Conference on Themoelectrics, 2001.

25. R. Venkatasubramanian, E. Siivola, T. Colpitts, and B. O'Quinn. Thin-film thermoelectric devices with high room-temperature figures of merit. Nature, 2001, Vol. 413, 597-602.

26. S. K. Bux, J. P. Fleurial and R.B. Kaner. Nanostructured materials for thermoelectric applications. Chem. Commun, 2010, Vol. 46, 8311-8324.

27. M.S. Dresselhaus, G.Chen, M.Y.Tang, R.G.Yang ,H.Lee and D.Z. Wang. New directions for low-dimensional thermoelectric materials. Adv. Mater, 2007, Vol. 19, 1043-1053.

28. G. S. Nolas, D. T. Morelli, and T. M. Tritt. SKUTTERUDITES: A Phonon-Glass-Electron Crystal Approach to Advanced Thermoelectric Energy Conversion Applications. Annu. Rev. Mater. Sci, 1999, Vol. 29, 89-116.

29. G. A. Slack, and V. Tsoukala. Some properties of semiconducting IrSb3. J. Appl. Phys, 1994, Vol. 76, 1665.

30. B. C. Sales, D. Mandrus, R. K. Williams. Filled Skutterudite Antimonides: A New Class of Thermoelectric Materials. Sci, 1996, Vol. 272, 1325-1328.

31. G. S. Nolas, J. L. Cohn, G. Slack, SB Schujman. Semiconducting Ge clathrates: Promising candidates for thermoelectric applications. Appl. Phys. Lett, 1998, Vol. 73, 178.

32. J. L. Cohn, G. S. Nolas, V. Fessatidis, T. H. Metcalf, and G. A. Slack. Glasslike Heat Conduction in High-Mobility Crystalline Semiconductors. Phys. Rev. Lett, 1999, Vol. 82, 779.

33. J. F. Meng, N. V. Chandra Shekar, J. V. Badding, and G. S. Nolas. Threefold enhancement of the thermoelectric figure of merit for pressure tuned Sr8Ga16Ge30. J. Appl. Phys, 2001, Vol. 18, 1730.

34. A. M. Guloy, R. Ramlau, Z. Tang, W. Schnelle, M. Baitinger, Y. Grin. A guest-free germanium clathrate. Nature, 2006, Vol. 443, 320.

35. C. Uher, J. Yang, S. Hu, D. T. Morelli, G. P. Meisner. Transport properties of pure and doped MNiSn (M=Zr, Hf). Phys. Rev. B, 1999, Vol. 59, 8615.

36. K. F. Hsu, S. Loo, F. Guo, W. Chen, J. S. Dyck, C. Uher, T. Hogan, E. K. Polychroniadis, M. G. Kanatzidis. Cubic AgPb(m)SbTe(2+m): bulk thermoelectric materials with high figure of merit. Sci, 2004, Vol. 303, 816.

37. Q. Jie, J. Zhou, L. Wu, J.-C. Zheng, Y. Zhu, Q. Li and J. Yang. Impact of Nanoscale Substructures on the Thermoelectric Properties of AgPbmSbTe2+m. MRS Fall Meeting, Boston, 2007.

38. J. Hejtmánek, M. Veverka, K. Knížek, H. Fujishiro, S. Hebert, Y. Klein, A. Maignan, C. Bellouard and B. Lenoir. Cobaltites as perspective thermoelectrics . Mater. Res. Soc. Symp, 2006, Vol. 886.

39. Y. F. Hu, W. D. Si, E. Sutter, Q. Li. In situ growth of cc-axis-oriented Ca3Co4O9Ca3Co4O9 thin films on Si (100). Appl. Phys. Lett, 2005, Vol. 082103, 171.

40. Y. Y. Wang, N. S. Rogado, R. J. Cava, and N. P. Ong, Nature, 2003, 423: 425. Spin entropy as the likely source of enhanced thermopower in NaxCo2O4. Nature, 2003, Vol. 423, 425-428.

41. L.D. Dresselhaus and M.S. Hicks and M. S. Effect of quantum-well structures on the thermoelectric figure of merit. Phys. Rev. B , 1993, Vol. 47, 12727.

42. H. Ohta, S. Kim, Y. Mune, T. Mizoguchi, K. Nomura, S. Ohta, T. Nomura, Y. Nkanishi, Y. Ikuhara, M. Hirano, H. Hosono, and K. Koumoto. Giant thermoelectric Seebeck coefficient of a two-dimensional electron gas in SrTiO3. Nature Materials, 2007, Vol. 6, 129-134.

43. A. I. Hochbaum, R. Chen, R. D. Delgado, W. Liang, E. C. Garnett, M. Najarian, A. Majumdar and P. Yang. Enhanced thermoelectric performance of rough silicon nanowires. Nature, 2008, Vol. 451, 163.

44. A.I. Boukai. Silicon nanowires as efficient thermoelectric materials. Nature, 2008, Vol. 451, 168-171.

45. P. Reddy. Thermoelectricity in Molecular Junctions. Sci, 2007, Vol. 315, 1568.

46. T. Harman, P.J. Taylor, D. L. Spears, M. P. Walsh. Thermoelectric quantum dot superlattices with high ZT. J. Electron. Mater, 2000, Vol. 29, 1-4.

47. X. Shi, J. Yang, J. R. Salvador, M. Chi, J. Y. Cho, H. Wang, S. Bai, J. Yang, W. Zhang and L. Chen. Multiple-Filled Skutterudites: High Thermoelectric Figure of Merit through Separately Optimizing Electrical and Thermal Transports. J. Am. Chem. Soc, 2011, Vol. 133, 7837–7846.

48. H.Bottner, G.Chen and R.Venkatasubramanian. Aspects of thin film, superlattice, thermoelectric materials, devices and applications. MRS Bulletin, 2006, Vol. 31, 211-217.

49. M.G. Kanatzidis. Nanostructured Thermoelectrics: The New Paradigm? Chem. Mater, 2010, Vol. 22, 648–659.

50. L. D. Zhao, S. Hao, S. H. Lo, C. I. Wu, X. Zhou, Y. Lee and H. Li. High Thermoelectric Performance via Hierarchical Compositionally Alloyed Nanostructures. J. Am. Chem. Soc, 2013, Vol. 135, 7364–7370.

51. H. J. Goldsmid, R. W. Douglas. The use of semiconductors in thermoelectric refrigeration. J. Appl. Phys, 1954, Vol. 5, 386-390.

52. G. A. Thomas, D. H. Rapke, R. B. Van Dover, L. F. Mattheis, W.A. Surden, L. F. Schneemaper and J. V. Waszczak. Large electronic-density increase on cooling a layered metal: Doped Bi2Te3. Phys. Rev. B, 1992, Vol. 46, 1553.

53. G. Kavei, M. A. Karami. Formation of anti-site defects and bismuth overstoichiometry in p-type Sb2−xBixTe3 thermoelectric crystals. J. Appl. Phys, 2008, Vol. 42, 67-73.

54. H. Scherrer and S. Scherrer. Handbook of Thermoelectrics. Chapter 19. Bismuth Telluride, Antimony Telluride, and Their Solid Solutions. CRC Press, 1995.

55. K. H.Park, M. Mohamed, Z. Aksamija and U. Ravaioli. Phonon scattering due to van der Waals forces in the lattice thermal conductivity of Bi2Te3 thin films. J. Appl. Phys, 2015, Vol. 117, 015103 .

56. P. Lostak, S. Karamazov, J. Horak. Antisite defects in BiSbTe3 crystals doped with indium atoms. Phys. Stat. Sol. A, 1994, Vol. 143, 271-276.

57. J. Horak, K. Cermak, L. Koudelka. Energy formation of antisite defects in doped Sb2Te3 and Bi2Te3 crystals. J. Phys. Chem. Solids, 1986, Vol. 47, 805-809.

58. J. Horak, P. Lostak, and L. Benes. Suppression of antistructural defects in crystals by an increased polarization of bonds. Philos. Mag. B Phys. Condens. Matter Stat. Mech. Electron. Opt. Magn. Prop, 1984, Vol. 50, 665-671.

59. H. Iwasaki, A. Ohishi, T. Kajihara, S. Sano. Control of the Figure of Merit by the Anti-site Defect in Thermoelectric Materials (Bi,Sb)2Te3. J. Appl. Phys, 2003, Vol. 42, 5477-5479.

60. J. Navratil, Z. Stary, T. Plechacek. Thermoelectric properties of p-type antimony bismuth telluride alloys prepared by cold pressing. Mater. Res. Bull, 1996, Vol. 31, 1559-1566.

61. C. Niu, Y. Dai, Y. Zhu, Y. Ma, L. Yu, S. Han and B. Huang. Realization of tunable Dirac cone and insulating bulk states in topological insulators (Bi1−xSbx)2Te3. Sci. Rep, 2012, Vol. 2, 976.

62. Y. Ma, Q. Hao, B. Poudel, Y. Lan, B. Yu, D. Wang, G. Chen and Z. Ren. Enhanced Thermoelectric Figure-of-Merit in p-Type Nanostructured Bismuth Antimony Tellurium Alloys Made from Elemental Chunks. nano letters, 2008, Vol. 8, 2580-2584.

63. W. Xie, X. Tang, Y. Yan, Q. Zhang and T. Tritt. Unique nanostructures and enhanced thermoelectric performance of melt-spun BiSbTe alloys. Appl. Phys. Lett , 2009, Vol. 94, 102111.

64. X. Zhao, X. Ji, Y. Zhang, T. Zhu, J. Tu, and X. Zhang. Bismuth telluride nanotubes and the effects on the thermoelectric properties of nanotube-containing nanocomposites. Appl. Phys. Lett, 2005, Vol. 86, 062111.

65. I. A. Drabkin, V. V. Karataev, V. B. Osvenski, A. I. Sorokin, G. I. Pivovarov, N. Yu. Tabachkova. Structure and Thermoelectric Properties of Nanostructured (Bi, Sb)2Te3 (Review). Advances in Materials Physics and Chemistry, 2013, Vol. 2, 119-132 .

66. S. Fan, J. Zhao, J. Guo, Q. Yan, J. Ma and H. H. Hng. p-type Bi0.4Sb1.6Te3Bi0.4Sb1.6Te3 nanocomposites with enhanced figure of merit. Appl. Phys. Lett, 2010, Vol. 96, 182104.

67. J. Jiang, L. Chen, S. Bai, Q. Yao and Q. Wang. Thermoelectric properties of p-type (Bi2Te3)x(Sb2Te3)1-x crystals prepared via zone melting. J. Cryst. Growth, 2005, Vol. 277, 258-263.

68. B. Poudel, Q. Hao, Y. Ma, C. Y. Lan, A. Minnich, B. Yu, X. Yan, D. Z. A. Muto, D. Veshaee, X. Y. Chen, J. M. Liu, M. S. Dresselhaus, G. Chen, Z. F. Ren. High-Thermoelectric Performance of Nanostructured Bismuth Antimony Telluride Bulk Alloys. Sci, 2008, Vol. 320, 634.

69. L. P. Hu, T. J. Zhu, Y. G. Wang, H. H. Xie, Z. J. Xu, X. B. Zhao. Shifting up the optimum figure of merit of p-type bismuth telluride-based thermoelectric materials for power generation by suppressing intrinsic conduction. NPG Asia Mater, 2014, Vol. 6, 88.

70. L. D. Zhao, B.P. Zhang, J.F. Li, H. L. Zhang and W. S. Liu. Enchanced thermoelectric and mechanical properies in textured n-type Bi2Te3 prepared by spark plasma sintering. Solid state Sci, 2008, Vol. 10, 651-658.

71. J.J. Shen, Z.Z. Yin,S.H. Yang, C. Yu, T.J. Zhu and X.B. Zhao. Improved Thermoelectric Performance of p-Type Bismuth Antimony Telluride Bulk Alloys Prepared by Hot Forging. J. Electron. Mater, 2011, Vol. 40, 1095-1099.

72. P. G. Ganesan, and V. Damodara Das. Thickness and temperature effects on electrical resistivity of (Bi0.5Sb0.5)2Te3 thin films. Matter. Lett, 2006, Vol. 60, 2059-2065.

73. X.Duan, J.Yang, W.Zhu, X.A.Fan and S.Q.Bao. Thickness and temperature dependence of electrical resistivity of p-type Bi0.5Sb1.5Te3 thin films prepared by flash evaporation method. J. Phys. D: Appl. Phys, 2006, Vol. 39, 5064-5068.

74. S. Jeon, H. Jeon, S. Nac, S. D. Kang, H. K. Lyeo, S. Hyun, H. J. Lee. Microstructure evolution of sputtered BiSb–Te thermoelectric films during post-annealing and its effects on the thermoelectric properties. J. Alloys Compd, 2013, Vol. 553, 343–349.

75. H. Lin, K. Kang, J. Hwang, H. Ghu, H. Huang, M. Wang. Effect of Annealing Temperature on the Thermoelectric Properties of the Bi0.5Sb1.5Te3 Thin Films Prepared by Radio-Frequency Sputtering. Metal Mater Tran A, 2013, Vol. 44, 2339-2345 .

76. L. Cao, Y. Wang, Y. Deng, H. Gao, B. Luo, W. Zhu. Facile synthesis of preferential Bi0.5Sb1.5Te3.0 nanolayered thin films with high power factor by the controllable layer thickness. J. Nanopart. Res, 2013, Vol. 15, 2088.

77. R. S. Makala, K. Jagannadham, B. C. Sales. Pulsed laser deposition of Bi2Te3-based thermoelectric thin films. J. Appl. Phys., 2003, Vol. 94, 3907-3918.

78. A. A. Aziz, M. Elsayed, H. A.Bakr, J. El-Rifai, T. Van der donck, J. Celis, V. Leonov, P. Fiorini, S. Sedky. Pulsed Laser Deposition of Bismuth Telluride Thin Films for Microelectromechanical Systems Thermoelectric Energy Harvesters. J. Electron. Mater, 2010, Vol. 39, 1920.

79. A. Boulouz, S. Chakraborty, A. Giani, F. P. Delannoy, A. Boyer, J. Schumann. Transport properties of V-VI semiconducting thermoelectric BiSbTe alloy thin films and their application to micromodule Peltier devices. J.Appl. Phys, 2001, Vol. 89, 5009-5014.

80. D.H. Kim, G.H Lee and O. J. Kim. The influence of post-deposition annealing on thermoelectric properties of Bi–Sb–Te films prepared by sputtering. Semicond. Sci. Technol, 2007, Vol. 22, 132-136.

81. D. Bourgault, B. Schaechner, C. Garampon, L. Carbone. Transport properties of thermoelectric Bi0.5Sb1.5Te3 and Bi2Te2.7Se0.3 thin films. J. Alloys Compd, 2014, Vol. 598, 79–84.

82. Z. Zheng, F. Ping, J. Luo, F. Ye. Thermoelectric properties of bismuth antimony tellurium thin films through bilayer annealing prepared by ion beam sputtering deposition. Thin Solid Films, 2014, Vol. 562, 181-184.

83. M. Takashiri, T. Shirakawa, K. Miyazaki, H. Tsukamoto. Fabrication and characterization of Bi0.4Te3.0Sb1.6 thin films by flash evaporation method. J. Alloys Compd, 2007, Vol. 441, 246–250.

84. M. Takashiri, S. Tanaka and K. Miyazaki. Improved thermoelectric performance of highly-oriented nanocrystalline bismuth antimony telluride thin films. Thin Solid Films , 2010, Vol. 519, 619-624.

85. M. Takashiri, S. Tanaka, H. Hagino and K. Miyazaki. strain and grain size effect on thermal transport in highly oriented nanocrystalline bismuth antimony telluride thin films . INT. J. HEAT MASS TRAN, 2014, Vol. 76, 376-384.

86. S. Kim, K. H. Lee, H. A Mun, H. Si. Kim, S.W. Hwang, J. W. Roh, D. J. Yang, W. H. Shin, X. S. Li, Y. H. Lee, G. J. Snyder and S. W. Kim. Dense dislocation arrays embedded in grain boundaries for high-performance bulk thermoelectrics. Sci, 2015, Vol. 348, 109-114.

87. J. Schou. Physical aspects of the pulsed laser deposition technique: The stoichiometric transfer of material from target to film. Appl. Surf. Sci, 2009, Vol. 255, 5191-5198 .

88. R. Eason. Pulsed Laser Deposition of Thin Films:Applications-Led Growth of Functional Materials. Wiley, 2007.

89. H. U. Krebs, M. Weisheit, J. Faupel, E. Süske, Th. Scharf, Ch. Fuhse, M. Störmer, K. Sturm, M. Seibt, H. Kijewski, D. Nelke, E.Panchenko, M. Buback. Pulsed Laser Deposition (PLD) - A Versatile Thin Film Technique. Advances in Solid State Physics, 2003, Vol. 43, 505-518.

90. http://nano-physics.pbworks.com/.

91. https://www.coherent.com/.

92. Silfvast, W. T. Laser Fundamentals, 2004, Vol. Cambridge University Press.

93. R.E. Billinge and S.J. Dinnebier. Powder Diffraction. Royal Society of Chemistry, 1-19.

94. B.E. Warren. X-ray diffraction. Dover Publications, 1990.

95. http://serc.carleton.edu/.

96. C.W. Oatley, W.C. Nixon and R.F.W. Pease. Scanning Electron Microscopy. ADV ELECTRON EL PHYS, 1966, Vol. 21, 181–247.

97. http://www.qdusa.com/.

98. https://www.nist.gov.

99. Tritt and M. Terry. Thermal conductivity: theory, properties, and applications. Kluwer Academic/Plenum Publishers, New York, Physics of solids and liquids, 2004.

100. M. J. Smith, R. J. Knight and C. W. Spencer. Properties of Bi2Te3-Sb2Te3 Alloys. J.Appl. Phy, 1962, Vol. 33, 2186-2190.

101. Y. Shtern, A.S. Malkova, A.S. Pashinkin and V.A. Fedorov. Heat capacity of the n-Bi2Te2.88Se0.12 and p-Bi0.52Sb1.48Te3 solid solutions. Inorg. Mater, 2008, Vol. 44, 10571059.

102. K. Kusagaya, M. Takashiri. Investigation of the effects of compressive and tensile strain on n-type bismuth telluride and p-type antimony telluride nanocrystalline thin films for use in flexible thermoelectric generators. Journal of Alloys and Compounds, 2015, Vol. 653, 480-485.

103. A. Dauscher, A. Thomy, H. Scherrer. Pulsed laser deposition of Bi2Te3 thin films. Thin Solid Films, 1996, Vol. 280, 61.

104. H.M. Eres and G. Christen. Recent advances in pulsed-laser deposition of complex-oxides. J. Phys. Condens. Matter, 2008, Vol. 20.

105. R. Zeipl, M. Pavelka, M. Jelínek, J. Chval, P. Lošťák, K. Ždánský, J. Vaniš, S. Karamazov, S. Vacková, J. WalachováR. Zeipl, M. Pavelka, M. Jelínek, J. Chval, P. Lošťák, K. Ždánský, J. Vaniš, S. Karamazov, S. Vacková, J. Walachová. Some properties of very thin Bi2Te3 layers prepared by laser ablation . Phys. Status Solidi C , 2003, Vol. 3, 867-871.

106. N.P. Bansal. Handbook of glass properties. New York: Academic Press, 1986.

107. N. Peranio, M. Wnkler, M. Durrschnabel, J. Konig, and O. Eibl. Assessing Antisite Defect and Impurity Concentrations in Bi2Te3 Based Thin Films by High-Accuracy Chemical Analysis. Adv. Funct. Mater, 2013, Vol. 23, 4969-4976.

108. D.Bourgault, C.Giroud Garampon, N. Caillault, L.Cardone,J.A. Aymami. Thermoelectric properties of n-type Bi2Te2.7Se0.3 and p-type Bi0.5Sb1.5Te3 thin films deposited by direct current magnetron sputtering. Thin Solid Films , 2008, Vol. 516, 8579-8583.

109. C. N. Liao, T.H.She. Preparation of bismuth telluride thin films through interfacial reaction. Thin Solid Films , 2007, Vol. 515, 8059-8060.

110. H. Noro, K. Sato, H. Kagechika. The thermoelectric properties and crystallography of Bi-Sb-Te-Se thin films grown. J. Appl. Phys, 1993, Vol. 73, 1252-1260.

111. Suga, Y. Thermoelectric semiconductor. Maki Syoten, Tokyo, 1966, 100-103.

112. L.M.Goncalves, C.Couto, J.H.Correia, P.Alpuim, Gao Min, D.M.Rowe. Optimization of thermoelectric thin-films deposited by co-evaporation on plastic substrates. ECT, 2006.

113. www.dupont.com.

114. O, Madelung. Semiconductors: Data Handbook, 3rd ed. Springer. Berlin, 2004.

115. A. Li Bassi, A. Bailini , CS. Casari, F. Donati , A. Mantegazza, M. Passoni. Thermoelectric properties of Bi–Te films with controlled structure and morphology. J Appl Phys, 2009, Vol. 105, 124307.

116. H. Obara, S. Higomo, M. Ohta, A. Yamamoto, K. Ueno, and T. Iida. Thermoelectric properties of Bi2Te3-based thin films with fine grains fabricated by pulsed laser deposition. J. Appl. Phys, 2009, Vol. 48, 085506.

117. J. E. Cornett, O. Rabin. Pulsed laser deposition and annealing of Bi2xSbxTe3 thin films. Solid-State Electroni, 2014, Vol. 101, 106-115.

118. Y. Li, J. Jiang, G. Xu, W. Li, L. Zhou, Y. Li, P. Cui. Synthesis of micro/nanostructured p-type Bi0.4Sb1.6Te3 and its thermoelectrical properties. J. Alloys Compd, 2009, Vol. 480, 954-957.

119. C. Liu, G. Liu, Y. Liu and L. Chen. Enchanced thermoelectric performance of compacted Bi0.5Sb1.5Te3 nanoplatelets with low thermal conductivity. J. Mater. Res,, 2011, Vol. 26, 1755-1761.

120. D. Li, R. Sun, X. Qin. Improving thermoelectric properties of p-type Bi2Te3 based alloys by spark plasma sintering. Material international, 2011, Vol. 21, 336-340.

121. J.J. Shen, S.N. Zhang, S.H. Yang, Z.Z. Yin, T.J. Zhu, X.B. Zhao. Thermoelectric and thermomechanical properties of the hot pressed polycrytalline Bi0.5Sb1.5Te3 alloys. J. Alloys Compd, 2011, Vol. 509, 161-164.

122. F.K. Lotgering. Topotactical reactions with ferromagnetic oxides having hexagonal crystal structures. J. Inorg. Nucl. Chem, 1959, Vol. 9, 113-123.

123. R.J. Payne and D.A. Ong. Processing effects for integrated PZT: Residual stress, thickness and dielectric properties. J. Am. Ceram. Soc, 2005, Vol. 88, 2839-2847.

124. W.M. Rosi and F.D.Yim. Compound Tellurides and their alloys for Peltier cooling-A review. Solid State Electron., 1972, Vol. 15, I12 I- 1140.

125. W. H. Yim, E. V. Fitzke and F. D. Rosi. Thermoelectric properties of Bi2Te3-Sb2Te3-Sb2Se3 pseudo-ternary alloys in the temperature range 77 to 300K. J. Mater. Sci, 1966, Vol. 1, 52-65.

126. J. J. Shen, L. P. Hu, T. J. Zhu, and X. B. Zhao. The texture related anisotropy of thermoelectric properties in bismuth telluride based polycrystalline alloys. Apl. Phys. Lett, 2011, Vol. 99.

127. W. Kim, J. Zide, A. Gossard, D. Klenov, S. Stemmer, A. Shakouri and A. Majumdar. Thermal Conductivity Reduction and Thermoelectric Figure of Merit Increase by Embedding Nanoparticles in Crystalline Semiconductors. Phys. Rev. Lett, 2006, Vol. 96, 045901.

128. L. Hu, H. Gao, X. Liu, H. Xie, J. Shen, T. Zhu and X. Zhao. Enhancement in thermoelectric performance of bismuth telluride based alloys by multi-scale microstructural effects. J. Mater. Chem, 2012, Vol. 22, 16484-16490.

129. W. E. Bies, R. J. Radtke, H. Ehrenreich, E. Runge. Thermoelectric properties of anisotropic semiconductors. Phys. Rev. B, 2002, Vol. 65, 085208.

130. K. Sharma, M. Lal, V.K. Gumber, A. Kumar, N. Chaudary and N. Goyal. Effect of Composition on Optical and Thermoelectric Properties of Microstructured p-type (Bi2Te3)x(Sb2Te3)1 – x Alloys. J. Nano- Electron. Phys, 2014, Vol. 6, 01007-1.